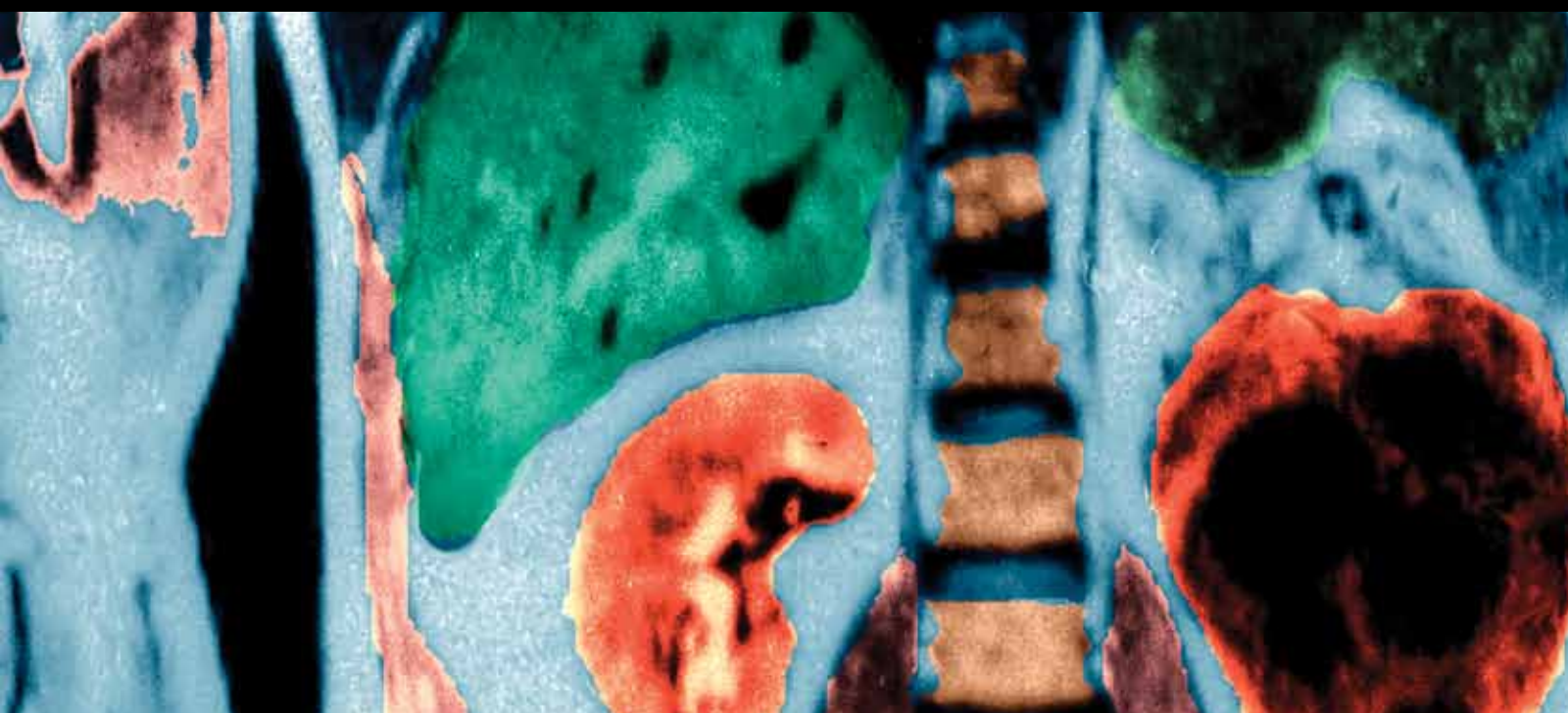# Three-Dimensional Imaging and Modeling of Anatomic Structures, Sectional and Radiological Anatomy, and Staining Techniques

Guest Editors: Tuncay Peker, Nadir Gülekon, Ilkan Tatar, Levent Sarıkcıoğlu, and David Kachlik

Three-Dimensional Imaging and Modeling of Anatomic Structures, Sectional and Radiological Anatomy, and Staining Techniques

Three-Dimensional Imaging and Modeling of Anatomic Structures, Sectional and Radiological Anatomy, and Staining Techniques

Guest Editors: Tuncay Peker, Nadir Gülekon, Ilkan Tatar, Levent Sarıkcıoğlu, and David Kachlik

Editorial Board

Contents

Editorial

Three-Dimensional Imaging and Modeling of Anatomic Structures, Sectional and Radiological Anatomy, and Staining Techniques

Tuncay Peker,[1] Nadir Gülekon,[1] Ilkan Tatar,[2] Levent Sarıkcıoğlu,[3] and David Kachlik[4]

[1] *Department of Anatomy, Gazi University, Faculty of Medicine, 06500 Ankara, Turkey*
[2] *Department of Anatomy, Hacettepe University, Faculty of Medicine, 06100 Ankara, Turkey*
[3] *Department of Anatomy, Akdeniz University, Faculty of Medicine, 07058 Antalya, Turkey*
[4] *Department of Anatomy, Third Faculty of Medicine, Charles University, 100 00 Prague 10, Czech Republic*

Correspondence should be addressed to Tuncay Peker, tpeker@gazi.edu.tr

The first three-dimensional (3D) reconstruction was performed by Born (1883) and His (1885) using serial sections. Since then, a variety of reconstruction techniques have been developed, and the construction of physical models has become important in anatomy. The first computer-aided 3D reconstruction was achieved by Glaser and Van der Loos in 1965. With the improvements in both computer hardware and software tools, computerized modelling of anatomical structures has become very useful for visualizing complex 3D forms. Three-dimensional visualization of various microanatomic structures using special preparation and staining methods is important. Devices used for this purpose such as MicroCT, microMRI, SEM, and Confocal microscopy and so forth. are development parallel to the technological advances and give excellent 3D images, and it allows a better understanding of gross and microanatomic structures. On the other hand, first studies on cross-sectional anatomy date back to the 16th century. The widespread use of cross-sectional imaging techniques such as CT and MRI has gained an increasing importance in sectional anatomy. The most known cadaveric cross-sectional study, the visible human project, is an outgrowth of the National Library Medicine.

In this special issue, we reviewed and edited seven articles on three-dimensional imaging and modeling of anatomic structures, sectional and radiological anatomy, and staining techniques.

K. K. Schmid (University of Nebraska, USA) Marx and Samal (University of Nebraska-Lincoln, USA) discussed three-dimensional regression, a technique that can be used for mapping images and shapes that are represented by sets of three-dimensional landmark coordinates, for comparing and mapping 3D anatomical structures in their research paper.

Y. Hoshino and coworkers (University of Pittsburgh, USA) reviewed previous research about image analysis of the anterior cruciate ligament (ACL) anatomy and its application to ACL reconstruction surgery. They concluded that three-dimensional image analysis of the ACL anatomy and its application to the navigation system is becoming more prevalent and reliable for advancing the anatomic studies related to the native ACL and the ACL reconstruction procedure.

A. Arencibia et al. (Veterinary Faculty, University of Las Palmas de Gran Canaria) investigated imaging features of the temporomandibular joint (TMJ) using computed tomography and magnetic resonance imaging in two normal camels. They stated in conclusion that CT is an excellent method for the detailed assessment of the bony structures, and MRI is a valid imaging modality for the evaluation of the soft tissues. Processing of CT and MR images allowes to appreciate different bone structures and soft tissues of the TMJ, assisting in the interpretation of the images.

J. A. N. Buytaert and colleagues (University of Antwerp and Ghent University, Belgium) discussed the first implementation of (laser) light-sheet-based fluorescence microscopy (LSFM) to image biomedical tissue in three-dimensional orthogonal plane fluorescence optical sectioning microscopy (OPFOS). They have shown with several applications that the OPFOS (and derived) methods are a valuable

addition for sectional imaging and three-dimensional modeling of anatomic structures.

The review paper entitled "*Ultrahigh voltage electron microscopy (UHVEM) links neuroanatomy and neuroscience/neuroendocrinology*" by H. Sakamoto (Okayama University, Japan) and M. Kawata (Kyoto Prefectural University of Medicine, Japan) stressed that UHVEM and light microscopy are useful and powerful tools for studying molecular and/or chemical neuroanatomy at the ultrastructural level.

D. R. Marker et al. (The Johns Hopkins Hospital and University School of Medicine, Weill Cornell Medical College, USA) discussed strategic improvements for gross anatomy web-based teaching in their research paper. To better meet the expectations of gross anatomy students, electronic radiology teaching files for first-year coursework were organized into a web site. The web site was custom designed to provide material that directly correlated to the gross anatomy dissection and lectures. Quick links provided sets of images grouped by anatomic location. Their findings suggest that a well-organized web portal can provide a user-friendly, valuable educational resource for medical students who are studying gross anatomy.

Finally, Herber and coworkers (University of California, USA) in their study entitled "*Imaging an adapted dentoalveolar complex*" used micro-X-ray computed tomography combined with 3D modeling using image processing, scanning electron microscopy, fluorochrome labeling, conventional histology (H&E, TRAP), and immunohistochemistry (RANKL, OPN) to elucidate the dynamic nature of bone, the periodontal ligamentspace, and cementum in the rat periodontium. They concluded that studies focusing on a functional rat dentoalveolar complex should acknowledge the baseline phenomena of bone-PDL-cementum adaptation, especially in regards to the physiological distal drift, before additional experimental variables are imposed.

We hope that this special issue will contribute as a stimulus for further research into three-dimensional imaging and modeling of anatomic structures, sectional and radiological anatomy, and staining techniques. We are very grateful to the contributing authors for their scientific contributions to this special issue. We also thank the reviewers who spend their valuable time and thoughts on each paper. We appreciate the Hindawi Publishing Corporation for their help in the guidance of the procedure.

Tuncay Peker
Nadir Gülekon
Ilkan Tatar
Levent Sarıkcıoğlu
David Kachlik

Research Article

Imaging an Adapted Dentoalveolar Complex

Ralf-Peter Herber,[1] Justine Fong,[2] Seth A. Lucas,[1] and Sunita P. Ho[2]

[1] *Division of Orthodontics, Department of Orofacial Sciences, University of California San Francisco, San Francisco, CA 94143, USA*
[2] *Division of Biomaterials and Bioengineering, Department of Preventive and Restorative Dental Sciences,*
  University of California San Francisco, San Francisco, CA 94143, USA

Correspondence should be addressed to Sunita P. Ho, sunita.ho@ucsf.edu

Adaptation of a rat dentoalveolar complex was illustrated using various imaging modalities. Micro-X-ray computed tomography for 3D modeling, combined with complementary techniques, including image processing, scanning electron microscopy, fluorochrome labeling, conventional histology (H&E, TRAP), and immunohistochemistry (RANKL, OPN) elucidated the dynamic nature of bone, the periodontal ligament-space, and cementum in the rat periodontium. Tomography and electron microscopy illustrated structural adaptation of calcified tissues at a higher resolution. Ongoing biomineralization was analyzed using fluorochrome labeling, and by evaluating attenuation profiles using virtual sections from 3D tomographies. Osteoclastic distribution as a function of anatomical location was illustrated by combining histology, immunohistochemistry, and tomography. While tomography and SEM provided past resorption-related events, future adaptive changes were deduced by identifying matrix biomolecules using immunohistochemistry. Thus, a dynamic picture of the dentoalveolar complex in rats was illustrated.

1. Introduction

The load-bearing bone is a dynamic tissue and continuously adapts to changes in loads [1]. In the periodontium, the cementum of a tooth is attached to the alveolar bone by the periodontal ligament (PDL), and the root is contained within the alveolar bone socket. Cementum and bone are calcified tissues of similar chemical composition, but cementum is far less dynamic [2]. The vascularized and innervated PDL consists of basic constituents that resist and dampen mechanical loads. Different types of collagen and noncollagenous proteins including polyanionic water attracting molecules, the proteoglycans (PGs), all of which accommodate cyclic occlusal loads of varying magnitudes and directions. Unlike other ligaments within the musculoskeletal system, the blood vessels in the PDL are continuous with blood vessels in the endosteal spaces of bone [3]. Although PDL and bone are two dissimilar tissues in physical and chemical properties, the continuity formed by blood vessels enables a flow of nutrients and maintains cellular activity responsible for PDL turnover and bone remodeling and modeling. Development and growth superimposed with functional loads [4] may cause posterior lengthening of the rat jaw [5], and can contribute to PDL turnover, bone remodeling, and load-related modeling during the lifespan of a rat. As a result, rat molars are thought to exhibit an inherent distal drift [6], but this theory continues to be controversial [7, 8]. Regardless, the drift of the molars causes bone resorption located on the distal side of the root and bone formation on the mesial side. In this study, the distal side of the root and the adjacent alveolar bone will be referred to as the distal root bone complex (bone resorption side), and the mesial side of the root and adjacent bone as the mesial root bone complex (bone apposition side). Specific to this study are the various imaging modalities implemented to investigate the physical, chemical, and biochemical changes reflective of distal drift in a rat bone-PDL-cementum complex.

Numerous studies in dental research have used the rat periodontium as a model to investigate adaptation of bone, PDL, and root due to perturbations, such as disease [9] and extraneous loads [10]. The perturbations could affect the bone-PDL and cementum-PDL attachment sites. Hence, it is important to know the baseline parameters in the rat model before additional variables are imposed. In this study, we

present an overview of commonly used imaging methods to investigate calcified tissues and the PDL, while addressing the plausible artifacts during specimen preparation, imaging, and postprocessing of experimental data.

Micro X-ray imaging is a popular method, as it provides a three-dimensional (3D) representation of organs and tissues. Micro X-ray imaging is used to study the internal architecture of bone [11], tooth [12], and the bone-PDL-cementum complex [3], along with resorption-related changes of the root [13]. Additionally, X-ray attenuation maps can be related to mineral density variations within calcified tissues [11].

Scanning electron microscopy (SEM) is used to study tissue architecture at a relatively higher resolution. In this study, SEM was used to identify resorbed bone [14] and root [15] morphology. Although not used in this study, the higher resolving power of a transmission electron microscope (TEM) provides information about the inorganic crystal type and morphology within a tissue matrix [16]. While most conventional SEM and TEM operate under high vacuum mode, an atomic force microscope (AFM) can image site-specific regions within tissues at ambient conditions, facilitating nanoscale and microscale observations of tissue architecture under hydrated conditions [17] with minimum specimen preparation [18]. AFM coupled with a nanoindentation transducer can be used for mapping site-specific mechanical properties of tissues and their interfaces [3].

Various spectroscopy techniques, including Fourier transform infrared spectroscopy (FTIR) [19] and Raman microspectroscopy [20] provide chemical composition of calcified tissues. Complementing spectroscopy techniques are numerous conventional histological, and immunohistochemical stains to identify cells relative to the spatial localization of biomolecules of interest. Histological analyses specific to this study include, hematoxylin and eosin (H&E) [21, 22], tartrate-resistant acid phosphatase (TRAP) [23, 24], and immunohistochemical staining using fluorescent probes for receptor activator of nuclear factor κB ligand (RANKL) [25, 26] and osteopontin (OPN) [27, 28]. Fluorochrome labeling is another widely used technique to study the temporal growth of bone and cementum [29, 30].

In this study, micro X-ray computed tomography (Micro-XCT) was used to image and measure the anatomical, physical, and chemical properties of calcified tissues in 3D and locate resorption and remodeling related events. Micro-XCT data was complemented with (immuno)histochemical studies to investigate biomolecular events within the bone-PDL-cementum complex. Furthermore, a combination of these techniques performed consecutively on the same specimen allowed correlating 2D histological sections with 3D tomography, performed before preparing the specimen for histology. Thus, synergetic effects of imaging modalities were exploited to develop a dynamic picture of the resorption and remodeling-related events in the load-bearing bone-PDL-cementum complex. The combination of techniques within describes complex events in the periodontium and illustrates potential mechanisms elucidating cause-and-effect relationships.

2. Materials and Methods

Maxillae from 7-week to 4-month-old male Sprague Dawley rats were used. Rats were obtained using animal tissue transfer according to guidelines of Institutional Animal Care and Use Committee (IACUC), University of California San Francisco (UCSF).

2.1. Micro X-Ray Computed Tomography. Entire heads or hemimaxillae were imaged using Micro-XCT (Micro XCT-200, Xradia, Pleasanton, CA). The occlusion was imaged using whole heads, while the tooth-bone complex was imaged using hemimaxillae. After harvesting, all specimens ($N = 8$) were placed in polymeric containers with 70% ethanol, mounted on a specimen stage, and imaged at different magnifications and power as needed using a Micro-XCT. Polymeric wire was used to bring the upper and lower jaws together to approximate the occlusal plane and was imaged using a 2x objective, at 90 KVp and a power of 6 W. The maxillae per se were imaged at 2x and 4x and 75 KVp and a power of 6 W. Each tomography was reconstructed from 3500 radiographic projections obtained from a full circle of 360° and exposure times were adjusted to yield 6000 to 8000 counts per pixel of each recorded radiograph approximating 25% of the original X-ray intensity passing through the specimen and arriving at the detector. Associated tomographies were reconstructed using reconstruction software (XMReconstructor, Version 7.0.2817, Xradia Inc., Pleasanton, CA). 3D images were postprocessed using the Xradia 3D viewer and Amira software (Visage Imaging Inc., Version 5.2.2, San Diego, CA).

2.2. Scanning Electron Microscopy. Maxillary molars ($N = 3$) were isolated using forceps, and the remaining bony sockets were cut to separate bone from the mesial and distal complex. The exposed alveolar socket and molars were mounted on SEM stubs and sputtered with gold. The specimens were examined using an SEM (S4300, Hitachi, Tokyo, Japan) with an electron energy of 5 keV.

2.3. Histology. Intact hemimaxillae ($N = 5$) were decalcified in 0.5 M EDTA solution for 3 weeks. The specimens were dehydrated with 80%, 95%, and 100% Flex alcohol (Richard-Allan Scientific, Kalamazoo, MI) before embedding in paraffin (Tissue Prep-II, Fisher Scientific, Fair Lawn, NJ). They were sagittally sectioned on a rotary microtome (Reichert-Jung Biocut, Vienna, Austria) using a disposable steel blade (TBF Inc., Shur/Sharp, Fisher Scientific, Fair Lawn, NJ). The paraffin serial sections were mounted on Superfrost Plus microscope slides (Fisher Scientific, Fair Lawn, NJ) and deparaffinized with xylene.

2.3.1. Hematoxylin and Eosin Stain. The sections were stained with hematoxylin (Fisher Scientific, Kalamazoo, MI) and eosin (Fisher Scientific, Kalamazoo, MI) [31]. The stained tissues were characterized using a light microscope (BX 51, Olympus America Inc., San Diego, CA) and analyzed

using Image Pro Plus v6.0 software (Media Cybernetics Inc., Silver Spring, MD).

2.3.2. Tartrate-Resistant Acid Phosphatase Histochemistry.
Deparaffinized serial sections were used for TRAP staining. In brief, the method [32] included treating the rehydrated specimens with 0.2 M acetate buffer, a solution of 0.2 M sodium acetate and 50 mM L(+) tartaric acid (Sigma-Aldrich, St. Louis, MO). After 20-minute incubation at room temperature, naphthol AS-MX phosphate and fast red TR salt were added followed by incubation at 37°C for 1 hour. The stained sections were washed in deionized water, counterstained with hematoxylin, and mounted with Immu-Mount (Thermo Scientific, Fremont, CA) for subsequent examination under a light microscope as stated above. Multiple images were stitched together to produce the resulting figure using Microsoft Research Image Composite Editor (Microsoft Corporation, Redmond, WA).

2.3.3. Immunostaining.
In the method used [26], deparaffinized sections were rehydrated, digested with trypsin (Sigma-Aldrich, St. Louis, MO) for ten minutes at 37°C, and subsequently rinsed and washed in deionized water. Specimens were incubated in blocking buffer (3% goat serum, 0.1% BSA in 1x PBS) and then in primary antibodies polyclonal rabbit anti-RANKL (Santa Cruz Biotechnology Inc., sc-9073, Santa Cruz, CA) or monoclonal mouse anti-OPN (Santa Cruz Biotechnology, Inc. Akm2A1, Santa Cruz, CA). Primary antibodies were diluted to 1:50 in blocking buffer. Slides were stored at 4°C in a humid case overnight, followed by washing three times for five minutes with 0.1% Tween-20 in PBS (PBST) and then incubated with secondary antibodies. Alexa Fluor 594 goat anti-rabbit (Invitrogen, A-11029, Carlsbad, CA) was used to label polyclonal rabbit anti-RANKL and Alexa Fluor 488 goat anti-mouse (Invitrogen, A-11037, Carlsbad, CA) to label monoclonal mouse anti-OPN, at 1:300 (diluted in blocking buffer). Slides were incubated in a opaque humid case for one hour at room temperature. Sections were washed three times for five minutes with PBST and then stained with 1:10000 trihydrochloride trihydrate (Invitrogen, Carlsbad, CA) for ten minutes in the absence of light. Slides were rinsed twice with PBS and mounted using Fluoro Gel (Electron Microscopy Sciences, Hartfield, PA). Stained tissues were visualized using Eclipse E800 fluorescent microscope (Nikon Inc., Melville, NY). TRITC filter (540–565 nm) was used to excite Alexa Fluor 594 (abs. 590 nm, emit. 617 nm), FITC filter (465–495 nm) to excite Alexa Fluor488 (abs. 495 nm, emit. 519 nm), and DAPI filter (340–380 nm) to excite trihydrochloride trihydrate (abs. 358 nm, emit. 461 nm). Multiple images were stitched together as described above.

2.4. Fluorochrome Study.
Under regulation of the animal protocol No. AN083692 and AN080608-02 approved by the IACUC, UCSF, 6-week- ($N = 3$) and 4-month- ($N = 3$) old male Sprague-Dawley rats were given intraperitoneal injections with alternating tetracycline hydrochloride and alizarin red (both Sigma-Aldrich, St. Louis, MO) on days 0, 3, and 7. According to the method used [29], 25 mg fluorochrome per 1 kg rat body mass was diluted in 2% $NaHCO_3$ to a concentration of 0.01 mg/μL before intraperitoneal injection. On day 8, rats were sacrificed using CO_2 gas and bilateral thoracotomy. Maxillae were dissected, fixed in 4% paraformaldehyde overnight, sectioned sagittally using a low-speed diamond saw (Isomet, Buehler, Lake Bluff, IL), and ground into 50 μm thick specimens for viewing under the fluorescent microscope (Eclipse E800, Nikon Inc., Melville, NY). FITC filter (465–495 nm) was used to excite tetracycline HCl (abs. 390–425 nm, emit. 525–560 nm) and TRITC filter (540–565 nm) to excite Alizarin Red (abs. 530–560 nm, emit. 580 nm). Multiple images were stitched together as described above.

3. Results and Discussion

In the 19th century, Wolff discussed adaptation of bone due to mechanical forces [1]. The occlusal force, primarily used in grinding the hard diet fed to rats, is the most prominent force in the periodontium [33]. Within this adaptation lies growth and function-related changes in bone and cementum, which will be illustrated through various imaging modalities.

Micro-XCT is a noninvasive technique that requires minimum specimen preparation. Specimens can be imaged under wet conditions, preserving different tissue structures and at microscopic resolution below 5 microns. Tomographies and virtual scans can be processed to evaluate mineral density, resorption volumes, displacement fields, and 3D spatial association of the root with the bony socket. The 3D tooth-bone association can provide insights to form-function relationships. Additionally, 2D images recorded with other techniques including light microscopy can be related to the 3D tomographies and 2D virtual sections, and potential artifacts due to specimen preparation can be identified. In this study, we used Micro-XCT for *in situ* imaging, to approximate interdigitation of disarticulated maxilla and mandible of a rat by imaging at 2x magnification (Figure 1, left). Root morphology, and resorbed pits in bone and roots were measured. Structural analysis through the volume of a specimen was correlated with virtual serial sections with least interpolation. Additionally, X-ray attenuation indicative of mineral density variations at the bone-PDL interface was investigated.

The Micro-XCT images presented in Figures 1–3 illustrate an accurate anatomy of the dentoalveolar complex. Accuracy is necessary to spatially correlate 2D measurements from other complementary studies by identifying landmarks, and anatomical planes within the dentoalveolar complex. Furthermore, 2D and 3D data will help identify deviations due to external perturbations such as, disease or load-mediated influences from baseline measurements.

A rat hemimaxilla contains one incisor and three molars. We focused our investigation on the molars responsible for masticatory function. The crown of the 1st molar is the biggest, with the largest occlusal surface, the 2nd molar measures approximately 2/3 s, and the 3rd molar 3/5 s of the
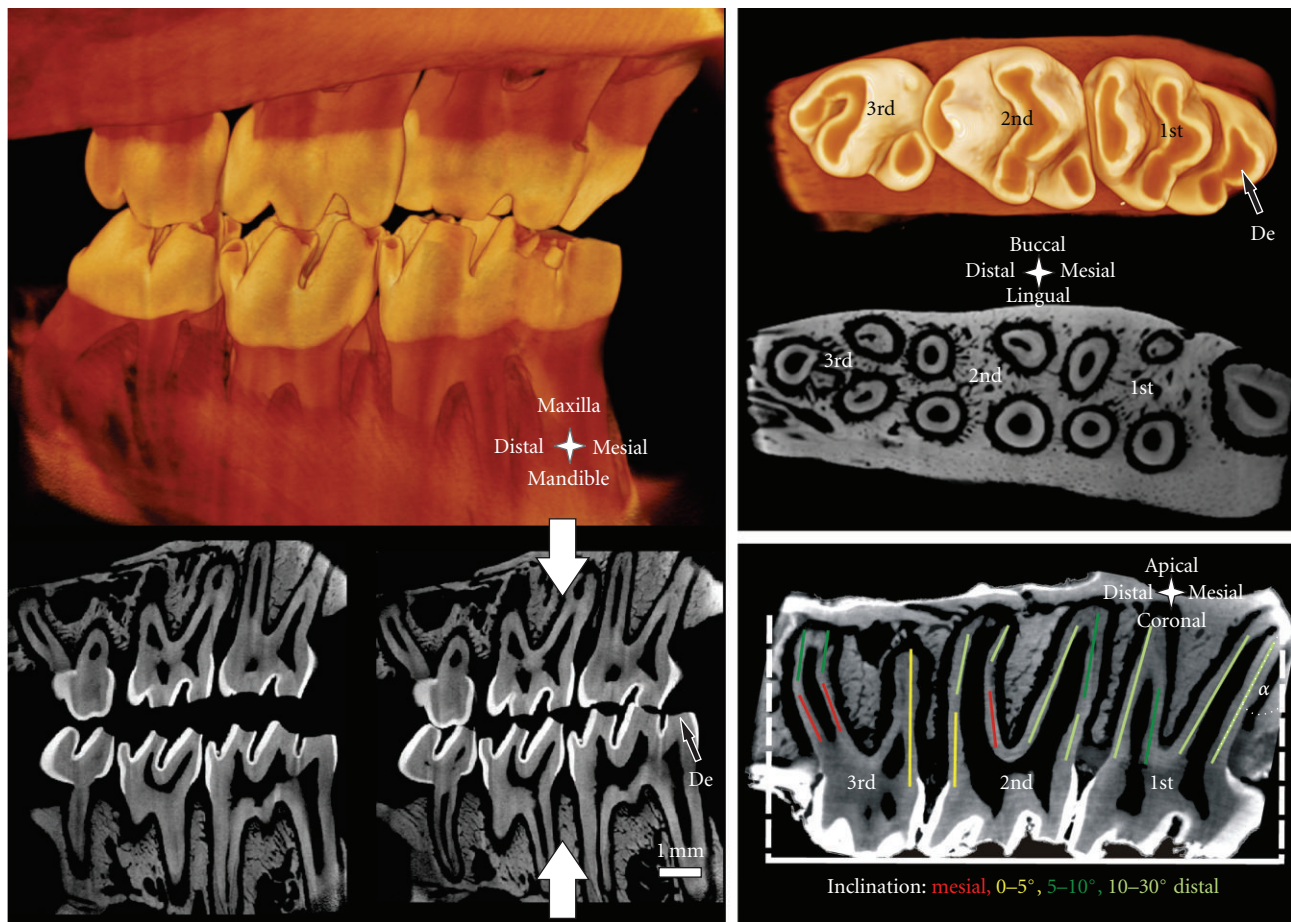
FIGURE 1: Left top: Simulated occlusion of a left rat maxilla with the corresponding mandible imaged with Micro-XCT. Left bottom: sagittal sections simulate open (left) and closed (right) bite. Top right: occlusal surface and transversal section of a right maxilla. Bottom right: sagittal section; note the predominant distal inclination of the roots. Inclination α is measured for the most mesial root as demonstrated. The colored segments on the roots represent the inclination angle of the roots. De = exposed dentin.

length of the 1st molar. In all specimens, a significant amount of occlusal wear was commonly observed. Figure 1 demonstrates enamel wear and exposed dentin on the occlusal surface. This could lead to varying contact between opposing teeth and is a potential cause for altered biomechanics and modeling-related adaptation in the bone-PDL-cementum complex throughout the lifespan of an organism.

The 1st molar is located mesially and the 3rd molar distally. Often times the challenge lies in identifying the anatomical directions of the specimen when only a part of it is imaged. Hence, certain predefined anatomical features are used to assign anatomical directions, and planes. Lingual and buccal sides of the hemimaxilla denote the tongue and cheeksides, respectively. The bone around the molars is slightly curved with the center of the curve toward the lingual side. The occlusal surface of all molars contains 2 or 3 enclosed depressions, with the most mesially located in the lingual half. The roots on the lingual side are more uniform in appearance and more closely aligned. The 1st, 2nd, and 3rd molar have 5, 4, and 3 roots, respectively. The 3rd molar exhibits an additional, but smaller, 4th root. The majority of the roots are within 2 parallel planes, the lingual and buccal

planes from the midsagittal section. The roots exhibit a slight distal inclination α of $10°-15°$. The angle of inclination is measured at the root apex, as the angle between root surface, and the normal to the occlusal surface, as shown in Figure 1 bottom right. According to the theory of Wolpoff [34], inclinations promote distal drift of the molars. At the age of 4 months, the roots are not straight but exhibit mesial curvature along with increasing distal inclination towards the root apex (Figures 1–3). The mesial root of the 1st and the distal root of the 3rd molar are exceptional cases, as they are centrally located with significant distal and mesial inclinations, respectively. Given such an anatomy, the rate of distal drift can also change due to a change in occlusal forces. Occlusal forces can generate distal force vectors because of the distal inclination of the roots [34]. Interestingly, root inclination in humans and primates is mesial [8, 35] and a physiological mesial drift is reported that enables closing of gaps due to development and function [34].

Based on the morphology of the tooth-bone complex in rats, it is conceivable that occlusal loads will compress the PDL in the distal root-tooth complex and simultaneously result in PDL tension within the mesial complex. Similar
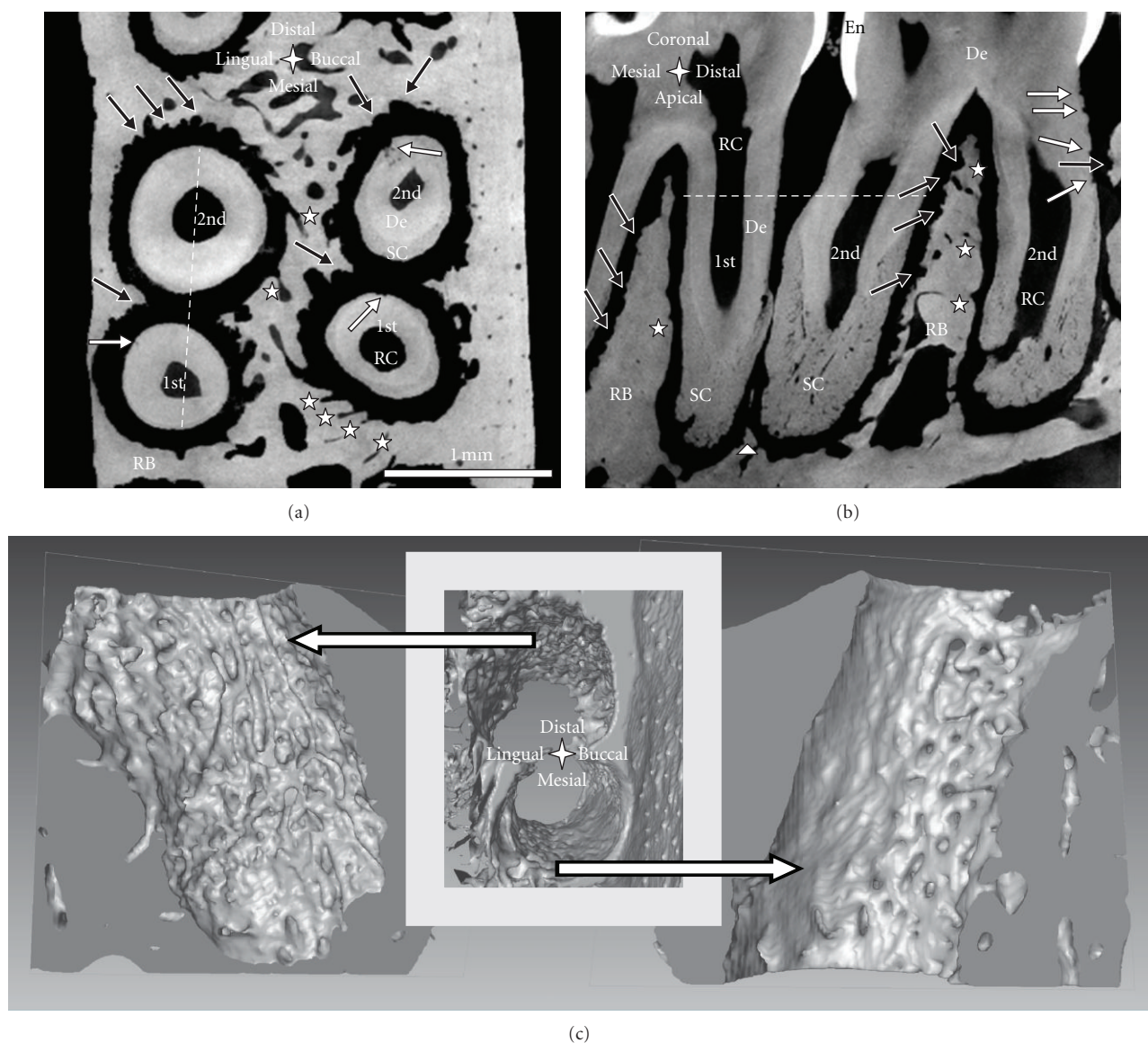
(a)

(b)

(c)

FIGURE 2: Transverse (a) and sagittal section (b) of the distal root of a 1st and the mesial root of a 2nd molar of a right maxilla exhibiting minimal interdental bone imaged with Micro-XCT; the white dotted lines indicate the position of the other section, respectively; note: bone resorption (black arrows), root resorption (white arrows), blood vessels (white stars), and residual interdental bone (white triangle). (c) 3D images of alveolar bone of the buccal roots in (a); bone surface of the distal root-bone complex shows resorption tracks (left image); holes on bone surface of the mesial complex indicate entering of blood vessels (right image). De = dentin, RB = interradicular bone, SC = secondary cementum, RC = root canal, and En = enamel.

effects exist in orthodontics, where compression sites in the PDL promote resorption and tension sites promote formation, resulting in tooth migration along the dominant force vector [36]. Cyclic compression and tension of the PDL during mastication could promote bone resorption and formation, respectively. Furthermore, it has been shown that different mechanical demands on the tooth-bone complex [4], and compression and tension sites related to distal inclination of the roots (Figure 2), affect microscale structure of alveolar bone and macroscale form of the bony socket. Consequently, bone morphologies in the distal and mesial root-tooth complex of the same root are inherently different as demonstrated in Figure 2.

Bone of the distal complex contains concave-rounded pits separated by narrow sharp ridges, resulting in a rough and pitted surface. This appearance is characteristic for distal bone and originates from the osteoclastic resorption activity also demonstrated in SEM micrographs (Figure 5) and histological images (i.e., Figures 6 and 7) of individual pits approximately 50 to $100\,\mu$m in diameter [37]. A reconstruction of the bony socket from the same Micro-XCT scan is illustrated in Figure 2(c). The extent of the osteoclastic activity can be observed as several resorption channels cut through the volume of the bone (Figure 2(c) left). Contrastingly, the bone from the mesial root-bone complex exhibits a smooth surface with convex-rounded
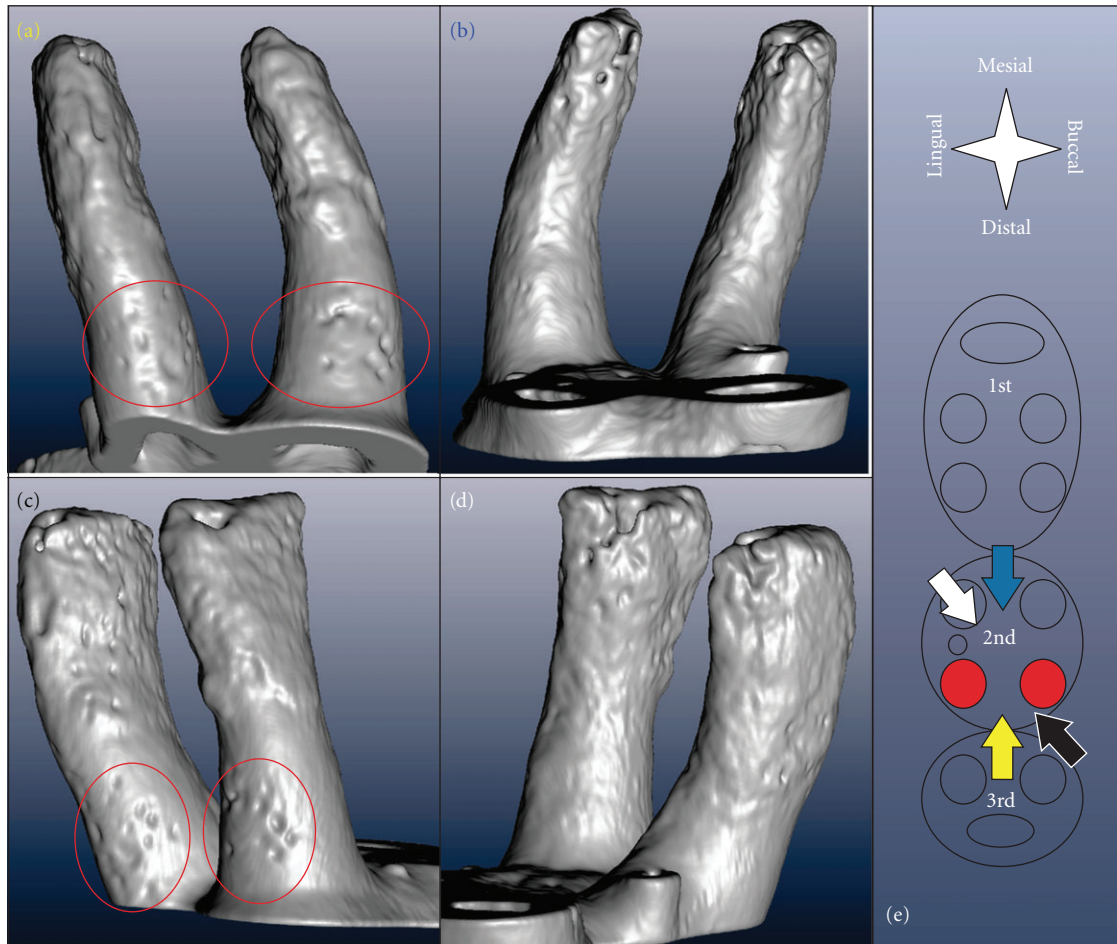
FIGURE 3: 3D reconstruction of the distal roots of 2nd molar viewed from different directions indicated by corresponding colors in (e). Accordingly, (a) shows the distal (yellow arrow), (b) the mesial (blue), (c) the buccal-distal (black), and (d) the lingual-mesial (white) surface of the roots; the apical parts of the roots are rough while the coronal parts are regularly rounded except for the resorption pits located on the coronal distal side of the root indicated by the red ovals.

bony protrusions into the PDL-space. The bony protrusions are separated by recesses or channels (Figure 2). The channels can be related to blood vessel spaces with red blood cells as shown in the H&E stained sections (Figure 6). The convex protrusions can be attributed to bone formation as demonstrated in the fluorochrome study (Figure 4 right). Regardless, the 3D images of bone demonstrates continuity of blood vessels in the PDL to those in bone (Figure 2(c)). Several histology sections in this study also support this observation in particular, Figure 6, top right.

The roots exhibit a significant structural anisotropy. The root surface, separated by a $100\,\mu$m thick PDL from the resorbed bone in the distal root-bone complex also exhibits resorption pits (Figure 2). The 3D images of the distal roots of a second molar in Figure 3, viewed from different angles illustrates the distribution of resorption pits on the root. Resorption pits on the root are less frequent than on bone. Pits on the root are small, and can be identified predominantly in the coronal region in primary cementum. While the mesial surfaces of the coronal thirds/halves of the roots typically show a regular morphology, several pits were identified in the coronal-distal portion of the roots. The apically located secondary cementum shows an overall high roughness and minor pits on all sides. The rough appearance of the secondary cementum in the apical part of the root has already been reported for rats [38], and was attributed to increased resorption and formation-related activities stimulated by occlusal loading.

Another remarkable anatomical feature is thinning of interdental bone, as shown in Figure 2. The distal root of the 1st molar and the mesial root of the 2nd molar share the same PDL-space and are in physical contact. Interdental bone commonly reaches the cervix of the tooth, and is comparable to the interradicular bone between the distal and mesial roots of the 2nd molar. Previous studies reported partial thinning of interdental bone, and resulting root proximity [39]. Figures 1 and 2 illustrate the apical parts of 2nd and the 3rd molars not separated by bone (Figure 1 bottom right, Figure 2(b)). In general, adequate interdental bone and PDL-space are maintained through combined resorption
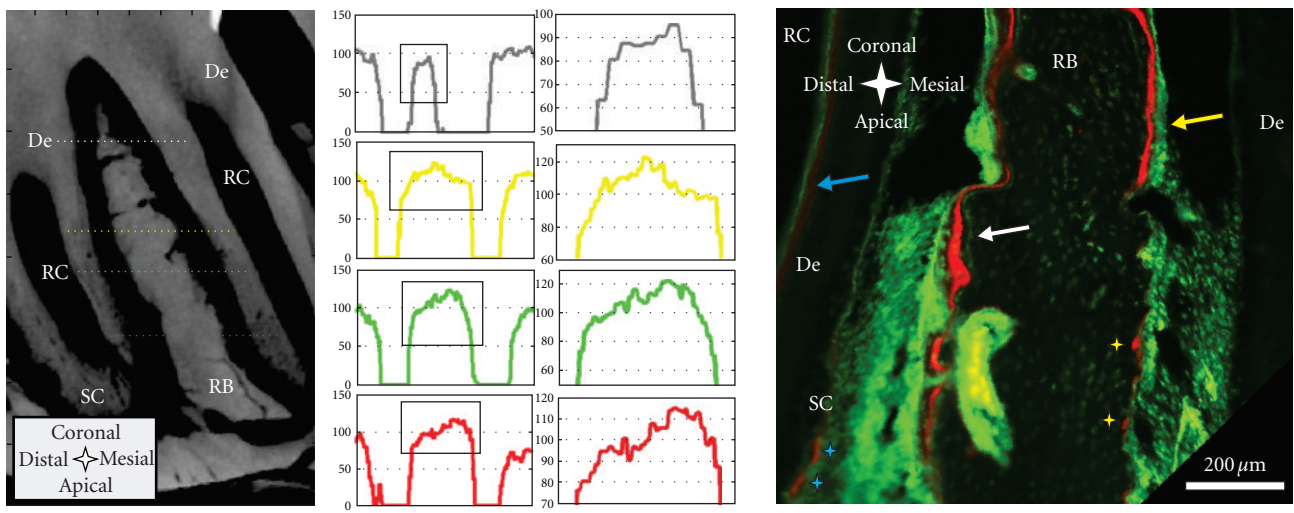
FIGURE 4: Left panel: Attenuation profiles (arbitrary units) from left to right through interradicular bone; bone formation in the mesial root-bone complex (left side) to bone resorption in the distal complex (right side) of the same molar. Attenuation of the "old" bone on the resorption side (right side) is generally higher and transition from PDL is steeper compared to the newly formed bone on the other side (left side). Right panel: sagittal section of a 7-week-old specimen with fluorochrome labeling; bone deposition predominantly in the mesial root-bone complex (white arrow), but also probably growth-related deposition in the distal complex (yellow arrow); note: predentin formation in the pulp (blue arrow), red stain on resorption pits (yellow stars); formation/repair of secondary cementum (blue stars). De = dentin, RB = interradicular bone, RC = root canal, and SC = secondary cementum.
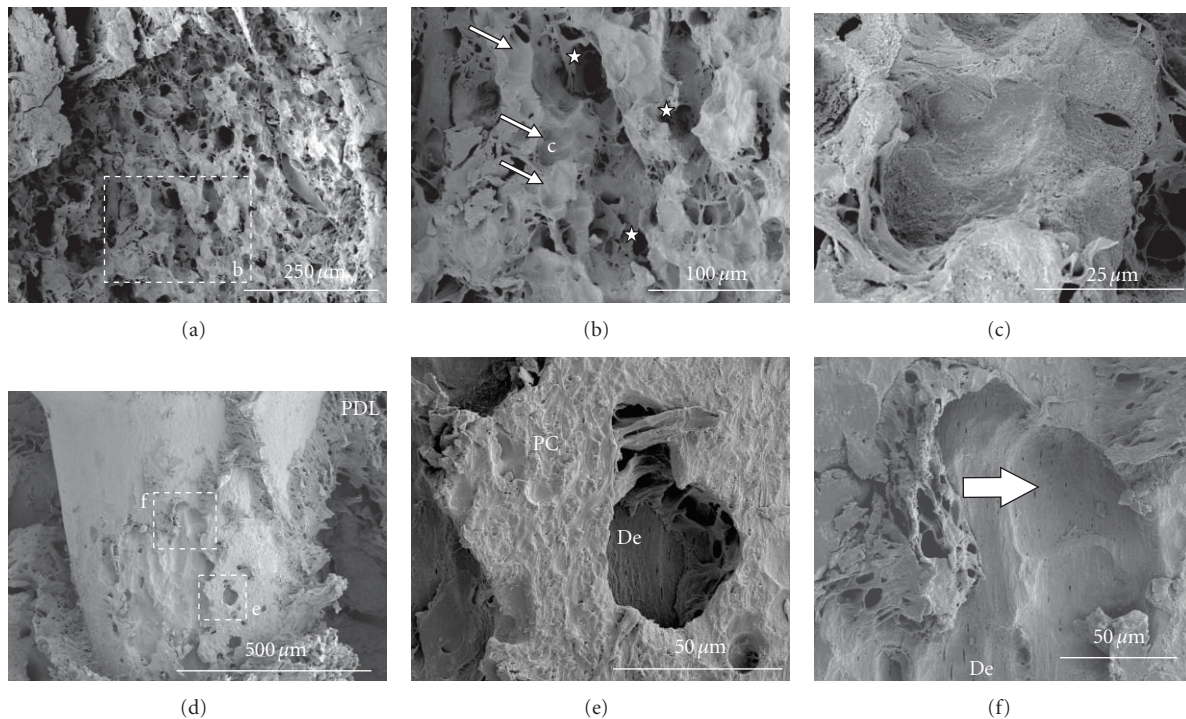
FIGURE 5: (a–c) SEM image of bone from the distal root-bone complex; (b) note: resorption pits (white arrows), blood vessel space (white stars); (c) high magnification of resorption pit. (d–f) SEM image of a root exhibiting heavy root resorption; (e) isolated pit in primary cementum; (f) larger resorption pit subdivided into smaller ones; note tubular structure of dentin in pits of (e) and (f). De = dentin, PC = primary cementum, and PDL = periodontal ligament.

FIGURE 6: Histological sections stained with H&E: (a) shows the entire root and indicates the position of the mesial (b) and distal (c) root-bone complex at higher magnifications; rough pitted bone surface on the surface of the distal complex and the regular surface in the mesial complex; note: resorption pits in bone (black arrows), cement lines in bone (grey arrows), root resorption (white arrows), and blood vessel spaces (white stars). De = dentin, RB = interradicular bone, DB = interdental bone, SC = secondary cementum, and PC = primary cementum.

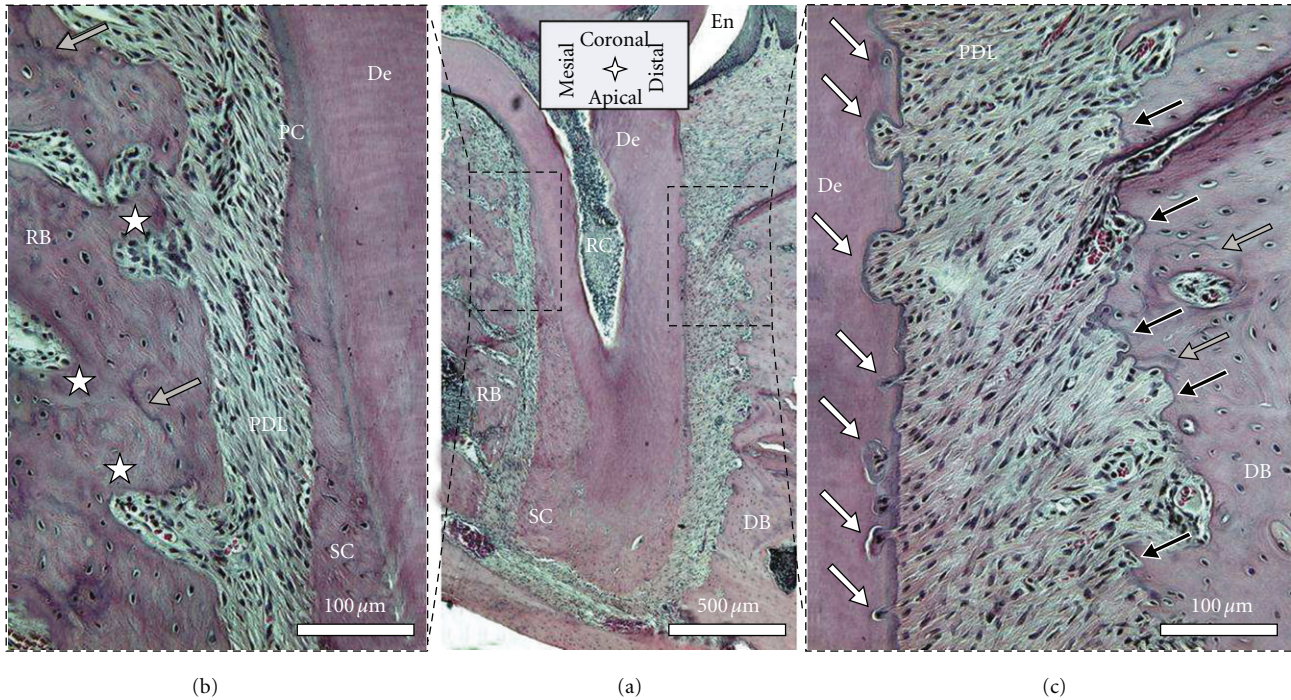(distal) and apposition (mesial) related events, accomodating movement of the molars [8]. Based on our observations and previous reports by others, we suggest different migration rates of the individual molars [40].

Apposition and resorption-related events manifest into lower and higher X-ray attenuation profiles in the mesial and distal root-bone complex. Micro-XCT techniques measure X-ray attenuation differences that can be directly related to bone mineral density when calibrated with phantoms of known mineral density [11]. Furthermore, mineral density differences can be exploited from virtual scans at a spatial resolution equivalent to the magnification at which the specimen was scanned. In this study highly attenuating regions in the specimen appear brighter and are related to higher mineral content. In the sagittal and transversal sections of the Micro-XCT images, we consistently observed darker areas representing lower X-ray attenuation close to the PDL interface in bone of the mesial root-bone complex (Figure 4 left). The graphs demonstrate that attenuation of bone in the distal complex is generally higher and that the increase of attenuation from PDL to bone is steeper than in the mesial root-bone complex. Lower attenuation in bone is caused by lower degree of mineralization and/or crystallinity and can be related to the earlier stages of modeled bone associated with distal drift. This continuous apposition of bone in the mesial root-bone complex accompanied by resorption of bone in the distal complex, coupled with adaptations in primary and secondary cementum, is necessary to maintain

a uniform functional PDL-space and accommodate the hard pellet diet in rats.

Complementing X-ray attenuation profiles, are results from fluorochrome labeling. Despite the cumbersome nature of the fluorochrome labeling technique, which includes injecting the animal periodically with different fluorescent dyes, followed by harvesting, specimen preparation, and imaging, the technique illustrates the dynamic nature of bone indicating potentially loaded areas in both tension and compression [41]. Fluorochrome labeling is an effective method to study biomineralization-related events [42]. Fluorochrome dyes form chelate complexes with exposed apatite within a mineralizing tissue. As a result, the fluorescent label demarcates active mineralizing fronts exhibiting mineralized tissue formation at the time of administration. By using alternating dyes and injecting at different timepoints, the stratified growth of bone can be temporally mapped [30]. Figure 4 shows a section of interradicular bone of a 2nd molar from a 7-week-old specimen. The sequence of green-red-green lines in the mesial root-bone complex demonstrates bone formation. The space between two lines shows that the mineralization front moved approximately $10–30\,\mu$m in the 3-4 days between two injections, which corresponds to a distal drift of approximately $20–30\,\mu$m over the same period [43, 44]. Coronal bone in the distal complex also shows fluorochrome labeling. Furthermore, the surface appears to be regular and convex. This could indicate that bone apposition/repair occasionally also occurs in the

distal root-bone complex. However, in the older 4-month-old specimen, significant bone formation was observed in the mesial complex.

Changes from resorption to apposition activity are the origin of cement lines [41], shown as basophilic lines in H&E stained sections (Figure 6). However, remaining distal bone illustrated a pitted surface, and no fluorochrome labeling, indicating resorption activity. Some of the pits exhibited a red lining on the surface, probably indicating local repair. Furthermore, the distal root in Figure 4, shows regular deposition of predentin in the pulp chamber and minor repair/formation activity on secondary cementum.

Specimen preparation for SEM is more cumbersome than for Micro-XCT. In particular, dehydration, fracturing, and sputtering of the specimen along with imaging under high vacuum can induce several artifacts and affect structural integrity. High-energy electrons can result in disintegration of soft tissue, and the vacuum chamber limits *in situ* experiments. However, its spatial resolution and magnification range are superior to the other techniques presented in this study. Hence, SEM measurements were conducted to study bone and root morphology, and in particular, resorption morphology at higher resolution. Figure 5(a) shows an SEM image of bone from a distal root-bone complex. At higher magnification, resorption pits and blood vessel openings can be identified (Figures 5(b)-5(c)). In Figure 5(c), a single pit of less than 50 μm was observed. Figures 5(d)–5(f) illustrate a case of excessive root resorption on the distal side of a 2nd molar, with a pattern of large and small pits and regular cementum surface. At a higher magnification, larger pits were subdivided into smaller pits with diameters of approximately 50 μm, (Figure 5(f)). Inside the larger pits within primary cementum (Figure 5(e)), typical tubular structure of dentin was observed.

While Micro-XCT, SEM, and fluorochrome staining coupled with fluorescence microscopy identified adaptation of the calcified tissue, the distribution of the cells, proteins, and organic matrix could not be imaged sufficiently due to low-contrast for X-rays and high-energy electrons, respectively. Though highly attenuating stains like phosphotungstic acid, osmium tetraoxide, and gallocyanin-chromalum improve imaging of the PDL fibers and most likely cells [45], the information that can be gathered from imaging following staining is still very limited compared to conventional histology and immunohistochemistry. Furthermore, the resolving power of the Micro-XCT is another limit. The latter would not pose a problem for SEM, but this method will introduce artifacts in the organic tissue due to specimen preparation, high vacuum, and higher-energy electrons as stated earlier. Hence chemically fixed histological sections were stained conventionally or using immunolabeling techniques. The preparation of the histological specimens is very time consuming, as it requires fixation, chemical processing, embedding, and sectioning. Moreover, it can introduce artifacts like delaminated interfaces and loss of structural integrity. The identification of stained organic matter is limited by the resolution of the analytical instruments: the optical or fluorescent microscopes. Furthermore, it should be noted that the sections prepared are 2D and can lead to

misinterpretation of 3D structures, despite the interpolation between serial sections.

Though H&E is a conventional stain, it is of value to the study, as it allows to distinguish basophilic structures that stain blue (nuclei), and eosinophilic structures that stain pink (intra and extracellular proteins), or red (red blood cells). This stain gives good structural contrast, and therefore the H&E stained sagittal section in Figure 6 can be compared to sagittal sections imaged with Micro-XCT (Figures 1 and 2). The bone surface in the mesial root-bone complex is regular and convexly rounded. The channels appearing prominently on the Micro-XCT images are also present and feature red blood cells. Thus, blood vessels in the PDL are continuous with those in bone. The mesial root surface is covered with a regular layer of cementum that broadens towards the apex. On the distal side, the layer of cementum is thin. Furthermore, the root exhibits a number of pits in dentin with a narrow pinch through cementum. Bone in the distal root-bone complex exhibits a strongly pitted surface, with basophilic lines (blue lines) around those pits. Other basophilic-rich regions include cementum resorption sites and cement lines in bone. The cement line is a remnant of the reversal from bone resorption to bone formation during a remodeling process. Hence, cement lines allow us to extrapolate beyond remodeling events. Cement lines can be found everywhere in bone. This shows that although resorption is the dominant process, remodeling is partly executed in the distal complex, as shown in the fluorochrome image (Figure 4 right). The cement line close to the bone surface in the distal root-bone complex, shown in Figure 6((c) lower grey arrow) could be an example for such local remodeling.

Compared to H&E, TRAP staining is specific to mature osteoclasts and more suitable for investigating adaptation of mineralized tissues [24, 46]. It has been shown that the secretion of TRAP by osteoclasts correlates with their resorptive behavior [23, 47], and therefore serves as a selective marker for osteoclastic activity. In our study of the rat periodontium, TRAP-positive cells were almost exclusively observed in the PDL-space of the distal root-bone complex (Figure 7), predominantly close to or in contact with the bone surface. TRAP-positive cells were also found on the surface of the roots, but consistently in lower numbers. These cells were multinucleated like osteoclasts (insert in Figure 7). TRAP-positive multinucleated cells resorbing cementum and dentin were also identified as odontoclasts [48].

Specificity, as exhibited by the TRAP stain is also fundamental to immunohistochemistry. It utilizes antibodies to bind to specific antigens of interest. For our study, RANKL and OPN, proteins related to bone remodeling, were chosen. The primary antibody is targeted by a secondary antibody that is bound to a fluorophore. Fluorescence-based immunohistochemistry allowed us to identify the distribution of the desired protein in the tissue. RANKL expression is necessary for differentiation and survival of osteoclasts. An increased number of active osteoclasts is a prerequisite for ongoing resorption due to distal drift. Osteoclastogenesis begins with hematopoietic cells generating mononuclear cells that are stepwise differentiated into mature osteoclasts
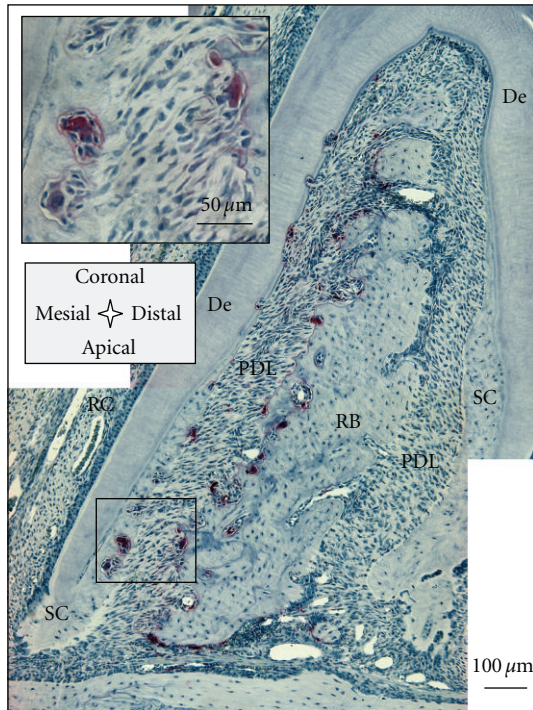
FIGURE 7: TRAP-positive cells located exclusively in the distal root-bone complex; *insert* shows multinucleated cells resorbing bone and secondary cementum, osteoclasts, and odontoclasts, respectively. De = dentin, RB = interradicular bone, PDL = periodontal ligament, SC = secondary cementum, and RC = root canal.

FIGURE 8: Histological sections immunostained with RANKL; the red RANKL stain is dominant in the PDL close to the bone surface of the distal root-bone complex (right image) compared to the mesial complex (left image); *insert*: note odontoclast on root and osteoclasts on bone (white stars). De = dentin, DB = interdental bone, PDL = periodontal ligament, and SC = secondary cementum.

[41]. Since the step in which mononuclear cells fuse into polykaryons, coincides with TRAP expression, RANKL [49] is recognized to play a significant role. An orthodontic study in rats found that compressed PDL promotes expression of RANKL [25]. In our study, Figure 8 shows that RANKL is upregulated in the compressed PDL of the distal root-bone complex, especially close to the bone-PDL attachment site, as compared to the attachment sites in the mesial complex. The large multinucleated cells in the resorption pits of bone and the root (osteoclasts and odontoclasts) also stained intensely for RANKL (Figure 8 insert).

OPN supports bone remodeling and is produced by osteoblasts, osteoclasts, and a number of other cells. It belongs to the family of small integrin-binding ligand N-linked glycoproteins (SIBLING). The proposed function of OPN in biomineralization [50] is threefold. It promotes cell adhesion of osteoclasts and osteoblasts. It regulates osteoclastic resorption and migration, and was shown to inhibit hydroxyapatite crystal growth by binding to its surface. In our study, most intense staining of OPN was found on the interface of bone and PDL in the distal complex (Figure 9). Its presence is indicated by green lines on the bone surface and green-stained multinucleated cells attached or close to those lines (Figure 9 right insert). The progression from bright to faint staining in the pits on the root surface on dentin, and on cementum, highlights resorption related events. The bulk cementum illustrated an undefined faint stain. Occasionally, brighter staining was found in cementum, specifically at the

primary to secondary cementum transition in Figure 9. This could be a sign of recent cementum repair as indicated by Jäger et al. [27]. The progression from bright green to red lines in bone are seemingly related to cement lines, which regularly stain for OPN [28]. The bone surface of the mesial complex neither exhibits bright green lines on the surface, nor osteoclasts complementing lack of TRAP staining in Figure 7. However, close to the bone surface, faint lines were consistently observed (Figure 9 left insert), and could indicate intermittent biomineralization.

4. Conclusions

The functional dentoalveolar complex in rat molars is a highly dynamic system with interactions between functional forces, 3D form, tissues, cells, and biomolecules. The periodontium is an interesting model to study the mechanisms of biomineralization. The inherent distal drift requires ongoing bone formation on the mesial side and resorption on the
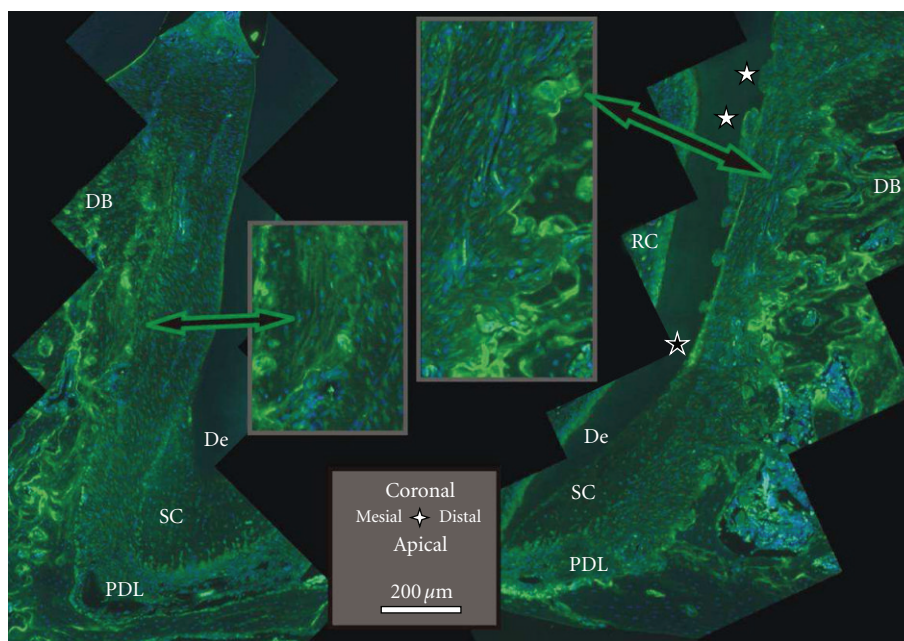
FIGURE 9: Histological sections immunostained with OPN; the green stain of OPN dominates the distal root-bone complex (right image); note staining on resorption pits and multinucleated cells on bone (right insert), resorption pits on the root (white stars), remodeling in secondary cementum (black star); on the mesial surface of the root (left image) less staining on the bone PDL interface, faint parallel lines in the bulk close to the bone surface in the mesial root-bone complex (left insert), and a single cell (left insert); cement lines stain as bright lines everywhere in the bulk bone. De = dentin, DB = interdental bone, PDL = periodontal ligament, SC = secondary cementum, and RC = root canal.

distal side of the root, to facilitate tooth migration and maintain functional PDL-space. For a better understanding of function-related adaptation, it is necessary to discuss observations at a macroscopic and a microscopic level and correlate them using complementary techniques. With Micro-XCT and post processing of 3D images, we were able to describe the anatomy of the dentoalveolar complex including, approximation of macroscopic occlusion, root geometry, and anisotropy in bone morphology due to the distribution of the microscopic resorption pits on bone and root. With SEM, we increased the resolution and identified structures created by the resorption activity. Attenuation profiles derived from Micro-XCT virtual sections, together with the fluorochrome study, highlighted advancement of the mineralization fronts in the mesial root-bone complex. Fluorochrome labeling pointed out that biomineralization, in relation to repair, can also exist in the distal complex. H&E staining verified structural features from Micro-XCT and SEM studies, and provided a basic understanding of the organic matrix. TRAP allowed for identification of multinucleated cells in the resorption pits of bone and root, found almost exclusively in the distal root-bone complex. Increased RANKL expression as a parallel event to TRAP could be found predominantly close to the distal complex of bone, and to a minor degree at the root surface. We could identify the omnipresence of OPN in the tissue, and related it to its multiple functions in the resorption and remodeling of mineralized tissues. Utilizing a variety of techniques had a synergetic effect to describe and understand the complex dynamic system of the rat periodontium. These results eluci-date that load-mediated perturbations and subsequent adaptation of the rat dentoalveolar complex, should acknowledge baseline function based adaptation of bone-PDL-cementum. Local remodeling and modeling related events associated with the physiological distal drift should also be identified before additional experimental variables are imposed.

Acknowledgments

References

[1] J. Wolff, "The classic: on the inner architecture of bones and its importance for bone growth," *Clinical Orthopaedics and Related Research*, vol. 468, no. 4, pp. 1056–1065, 2010.

[2] B. L. Foster, T. E. Popowics, H. K. Fong, and M. J. Somerman, "Advances in defining regulators of cementum development

and periodontal regeneration," *Current Topics in Developmental Biology*, vol. 78, pp. 47–126, 2007.

[3] S. P. Ho, M. P. Kurylo, T. K. Fong et al., "The biomechanical characteristics of the bone-periodontal ligament-cementum complex," *Biomaterials*, vol. 31, no. 25, pp. 6635–6646, 2010.

[4] A. Mavropoulos, S. Kiliaridis, A. Bresin, and P. Ammann, "Effect of different masticatory functional and mechanical demands on the structural adaptation of the mandibular alveolar bone in young growing rats," *Bone*, vol. 35, no. 1, pp. 191–197, 2004.

[5] H. Sicher and J. P. Weinmann, "Bone growth and physiologic tooth movement," *American Journal of Orthodontics and Oral Surgery*, vol. 30, no. 3, pp. C109–C132, 1944.

[6] A. G. Kraw and D. H. Enlow, "Continuous attachment of periodontal membrane," *American Journal of Anatomy*, vol. 120, no. 1, pp. 133–148, 1967.

[7] D. Roux, C. Chambas, B. Normand, and A. Woda, "Analysis of tooth movement into an extraction space in the rat," *Archives of Oral Biology*, vol. 35, no. 1, pp. 17–22, 1990.

[8] J. L. Saffar, J. J. Lasfargues, and M. Cherruau, "Alveolar bone and the alveolar process: the socket that is never stable," *Periodontology 2000*, vol. 13, no. 1, pp. 76–90, 1997.

[9] A. L. Dumitrescu, S. A. El-Aleem, B. Morales-Aza, and L. F. Donaldson, "A model of periodontitis in the rat: effect of lipopolysaccharide on bone resorption, osteoclast activity, and local peptidergic innervation," *Journal of Clinical Periodontology*, vol. 31, no. 8, pp. 596–603, 2004.

[10] Y. Ren, J. C. Maltha, and A. M. Kuijpers-Jagtman, "The rat as a model for orthodontic tooth movement—a critical review and a proposed solution," *European Journal of Orthodontics*, vol. 26, no. 5, pp. 483–490, 2004.

[11] A. J. Burghardt, T. M. Link, and S. Majumdar, "High-resolution computed tomography for clinical imaging of bone microarchitecture," *Clinical Orthopaedics and Related Research*, vol. 469, no. 8, pp. 2179–2193, 2011.

[12] G. Plotino, N. M. Grande, R. Pecci, R. Bedini, C. H. Pameijer, and F. Somma, "Three-dimensional imaging using microcomputed tomography for studying tooth macromorphology," *Journal of the American Dental Association*, vol. 137, no. 11, pp. 1555–1561, 2006.

[13] D. A. Harris, A. S. Jones, and M. A. Darendeliler, "Physical properties of root cementum: part 8. Volumetric analysis of root resorption craters after application of controlled intrusive light and heavy orthodontic forces: a microcomputed tomography scan study (vol 130, p. 639, 2006)," *American Journal of Orthodontics and Dentofacial Orthopedics*, vol. 132, no. 3, p. 277, 2007.

[14] S. Ren, H. Takano, and K. Abe, "Two types of bone resorption lacunae in the mouse parietal bones as revealed by scanning electron microscopy and histochemistry," *Archives of Histology and Cytology*, vol. 68, no. 2, pp. 103–113, 2005.

[15] C. Gonzales, H. Hotokezaka, M. A. Darendeliler, and N. Yoshida, "Repair of root resorption 2 to 16 weeks after the application of continuous forces on maxillary first molars in rats: a 2- and 3-dimensional quantitative evaluation," *American Journal of Orthodontics and Dentofacial Orthopedics*, vol. 137, no. 4, pp. 477–485, 2010.

[16] M. A. Rubin, I. Jasiuk, J. Taylor, J. Rubin, T. Ganey, and R. P. Apkarian, "TEM analysis of the nanostructure of normal and osteoporotic human trabecular bone," *Bone*, vol. 33, no. 3, pp. 270–282, 2003.

[17] S. P. Ho, B. Yu, W. Yun, G. W. Marshall, M. I. Ryder, and S. J. Marshall, "Structure, chemical composition and mechanical properties of human and rat cementum and its interface with root dentin," *Acta Biomaterialia*, vol. 5, no. 2, pp. 707–718, 2009.

[18] T. Hassenkam, H. L. Jørgensen, and J. B. Lauritzen, "Mapping the imprint of bone remodeling by atomic force microscopy," *Anatomical Record A*, vol. 288, no. 10, pp. 1087–1094, 2006.

[19] E. P. Paschalis, F. Betts, E. DiCarlo, R. Mendelsohn, and A. L. Boskey, "FTIR microspectroscopic analysis of normal human cortical and trabecular bone," *Calcified Tissue International*, vol. 61, no. 6, pp. 480–486, 1997.

[20] G. Penel, G. Leroy, C. Rey, and E. Bres, "MicroRaman spectral study of the PO4 and CO3 vibrational modes in synthetic and biological apatites," *Calcified Tissue International*, vol. 63, no. 6, pp. 475–481, 1998.

[21] G. Anneroth, K. H. Danielsson, H. Evers, K. G. Hedström, and A. Nordenram, "Periodontal ligament injection. An experimental study in the monkey," *International Journal of Oral Surgery*, vol. 14, no. 6, pp. 538–543, 1985.

[22] Y. Sasano, Y. Maruya, H. Sato et al., "Distinctive expression of extracellular matrix molecules at mRNA and protein levels during formation of cellular and acellular cementum in the rat," *Histochemical Journal*, vol. 33, no. 2, pp. 91–99, 2001.

[23] N. Z. Angel, N. Walsh, M. R. Forwood, M. C. Ostrowski, A. I. Cassady, and D. A. Hume, "Transgenic mice overexpressing tartrate-resistant acid phosphatase exhibit an increased rate of bone turnover," *Journal of Bone and Mineral Research*, vol. 15, no. 1, pp. 103–110, 2000.

[24] A. R. Hayman, P. Macary, P. J. Lehner, and T. M. Cox, "Tartrate-resistant acid phosphatase (Acp 5): identification in diverse human tissues and dendritic cells," *Journal of Histochemistry and Cytochemistry*, vol. 49, no. 6, pp. 675–683, 2001.

[25] T. Kim, A. Handa, J. Iida, and S. Yoshida, "RANKL expression in rat periodontal ligament subjected to a continuous orthodontic force," *Archives of Oral Biology*, vol. 52, no. 3, pp. 244–250, 2007.

[26] Q. Yan, Y. Zhang, W. Li, and P. K. DenBesten, "Micromolar fluoride alters ameloblast lineage cells in vitro," *Journal of Dental Research*, vol. 86, no. 4, pp. 336–340, 2007.

[27] A. Jäger, D. Kunert, T. Friesen, D. Zhang, S. Lossdörfer, and W. Götz, "Cellular and extracellular factors in early root resorption repair in the rat," *European Journal of Orthodontics*, vol. 30, no. 4, pp. 336–345, 2008.

[28] A. Nanci, "Content and distribution of noncollagenous matrix proteins in bone and cementum: relationship to speed of formation and collagen packing density," *Journal of Structural Biology*, vol. 126, no. 3, pp. 256–269, 1999.

[29] X. Luan, Y. Ito, S. Holliday et al., "Extracellular matrix-mediated tissue remodeling following axial movement of teeth," *Journal of Histochemistry and Cytochemistry*, vol. 55, no. 2, pp. 127–140, 2007.

[30] S. M. van Gaalen, M. C. Kruyt, R. E. Geuze, J. D. de Bruijn, J. Alblas, and W. J. Dhert, "Use of fluorochrome labels in in vivo bone tissue engineering research," *Tissue Engineering B*, vol. 16, no. 2, pp. 209–217, 2010.

[31] F. L. Carson, *Histotechnology—A Selfinstructional Text*, American Society Clinical Pathology, 1990.

[32] A. Erlebacher and R. Derynck, "Increased expression of TGF-β2 in osteoblasts results in an osteoporosis-like phenotype," *Journal of Cell Biology*, vol. 132, no. 1-2, pp. 195–210, 1996.

[33] A. Mavropoulos, A. Bresin, and S. Kiliaridis, "Morphometric analysis of the mandible in growing rats with different masticatory functional demands: adaptation to an upper posterior bite block," *European Journal of Oral Sciences*, vol. 112, no. 3, pp. 259–266, 2004.

[34] M. H. Wolpoff, "Interstitial wear," *American Journal of Physical Anthropology*, vol. 34, no. 2, pp. 205–227, 1971.

[35] J. P. Weinmann, "Bone changes related to eruption of the teeth," *Angle Orthodontist*, vol. 11, no. 2, pp. 83–99, 1941.

[36] W. R. Proffit, H. W. Fields, and D. M. Sarver, *Contemporary Orthodontics*, Mosby Elsevier, St. Louis, Mo, USA, 4th edition, 2007.

[37] Y. Hu, B. Ek-Rylander, E. Karlström, M. Wendel, and G. Andersson, "Osteoclast size heterogeneity in rat long bones is associated with differences in adhesive ligand specificity," *Experimental Cell Research*, vol. 314, no. 3, pp. 638–650, 2008.

[38] C. Gonzales, H. Hotokezaka, M. Yoshimatsu, J. H. Yozgatian, M. A. Darendeliler, and N. Yoshida, "Force magnitude and duration effects on amount of tooth movement and root resorption in the rat molar," *Angle Orthodontist*, vol. 78, no. 3, pp. 502–509, 2008.

[39] K. Vermylen, G. N. T. de Quincey, M. A. van 'T Hof, G. N. Wolffe, and H. H. Renggli, "Classification, reproducibility and prevalence of root proximity in periodontal patients," *Journal of Clinical Periodontology*, vol. 32, no. 3, pp. 254–259, 2005.

[40] A. B. Hardt, "Bisphosphonate effects on alveolar bone during rat molar drifting," *Journal of Dental Research*, vol. 67, no. 11, pp. 1430–1433, 1988.

[41] A. G. Robling, A. B. Castillo, and C. H. Turner, "Biomechanical and molecular regulation of bone remodeling," *Annual Review of Biomedical Engineering*, vol. 8, pp. 455–498, 2006.

[42] H. M. Frost, "Tetracycline-based histological analysis of bone remodeling," *Calcified Tissue Research*, vol. 3, no. 1, pp. 211–237, 1969.

[43] G. J. King, S. D. Keeling, E. A. McCoy, and T. H. Ward, "Measuring dental drift and orthodontic tooth movement in response to various initial forces in adult rats," *American Journal of Orthodontics and Dentofacial Orthopedics*, vol. 99, no. 5, pp. 456–465, 1991.

[44] J. J. Lasfargues and J. L. Saffar, "Effects of prostaglandin inhibition on the bone activities associated with the spontaneous drift of molar teeth in the rat," *Anatomical Record*, vol. 234, no. 3, pp. 310–316, 1992.

[45] B. D. Metscher, "MicroCT for developmental biology: a versatile tool for high-contrast 3D imaging at histological resolutions," *Developmental Dynamics*, vol. 238, no. 3, pp. 632–640, 2009.

[46] B. Ek-Rylander, P. Bill, M. Norgard, S. Nilsson, and G. Andersson, "Cloning, sequence, and developmental expression of a type 5, tartrate-resistant, acid phosphatase of rat bone," *Journal of Biological Chemistry*, vol. 266, no. 36, pp. 24684–24689, 1991.

[47] B. Kirstein, T. J. Chambers, and K. Fuller, "Secretion of tartrate-resistant acid phosphatase by osteoclasts correlates with resorptive behavior," *Journal of Cellular Biochemistry*, vol. 98, no. 5, pp. 1085–1094, 2006.

[48] T. Sasaki, "Differentiation and functions of osteoclasts and odontoclasts in mineralized tissue resorption," *Microscopy Research and Technique*, vol. 61, no. 6, pp. 483–495, 2003.

[49] G. Franzoso, L. Carlson, L. Xing et al., "Requirement for NF-κB in osteoclast and B-cell development," *Genes and Development*, vol. 11, no. 24, pp. 3482–3496, 1997.

[50] C. M. Giachelli and S. Steitz, "Osteopontin: a versatile regulator of inflammation and biomineralization," *Matrix Biology*, vol. 19, no. 7, pp. 615–622, 2000.

Research Article

Strategic Improvements for Gross Anatomy Web-Based Teaching

David R. Marker,[1] Krishna Juluru,[2] Chris Long,[1] and Donna Magid[1, 3]

[1] *Department of Radiology, The Johns Hopkins Hospital, 601 North Caroline Street, Baltimore, MD 21287, USA*
[2] *Department of Radiology, Weill Cornell Medical College, 525 E. 68th Street, F-056, New York, NY 10065, USA*
[3] *The Russell H. Morgan Department of Radiology and Radiological Science, The Johns Hopkins University School of Medicine,*
  601 N. Caroline Street, JHOC 5165, Baltimore, MD 21287, USA

Correspondence should be addressed to Donna Magid, dmagid@jhmi.edu

Current generations of graduate students have been immersed in technology from their early school years and have high expectations regarding digital resources. To better meet the expectations of Gross Anatomy students at our institution, electronic radiology teaching files for first-year coursework were organized into a web site. The web site was custom designed to provide material that directly correlated to the Gross Anatomy dissection and lectures. Quick links provided sets of images grouped by anatomic location. Additionally, Lab and Study Companions provided specific material for the students to review prior to and after lectures and gross dissections. Student opinions of this education resource were compared to student opinions of the prior year's digital teaching files. The new content was ranked as more user friendly (3.1 points versus 2.3 points) and more useful for learning anatomy (3.3 points versus 2.6 points). Many students reported that using the web portal was critical in helping them to better understand relationships of anatomical structures. These findings suggest that a well-organized web portal can provide a user-friendly, valuable educational resource for medical students who are studying Gross Anatomy.

1. Introduction

Gross anatomy is a fundamental component of first-year medical school curriculum. During this course, students gain a distinct visual understanding of the organ systems and their relationships to one another. Traditionally this visual understanding has been obtained through a surgical perspective provided by gross dissection or prosection [1]. More recently, with the advent of modern medical imaging, anatomy education has increasingly been supplemented by a radiological perspective [2–4]. Gross Anatomy coursework that provides both perspectives is arguably the ideal training for medical students who will require facility using both views during surgery and radiology rotations or when consulting these services. In support of this educational approach, several recent studies have reported improved clinical training through the use of imaging educational resources [3, 5–7]. In a study that directly compared the approaches, Stanford et al. reported that the combination of gross dissection and computer-based educational tools was a more efficacious teaching approach than either teaching modality alone [8].

As imaging has been adopted in the modern medical education, it has benefited from the concurrent development of technologies that have allowed the material to be presented electronically. One of the technologies with the greatest impact has been the Internet [9]. The Internet has increasingly been utilized as an educational tool due to its ability to provide a large volume of educational material in a single, readily-accessible location as well as permitting flexibility in the material format. Images, text, interactive quizzes, and videos can be integrated seamlessly into a comprehensive educational resource. While these capabilities are largely beneficial, they can have a negative effect on the efficacy of the educational resource if the material is poorly organized. For example, if students are confronted with a vast amount of information on the Internet that is presented in a non-user-friendly format, they are likely to either not utilize the resource or not benefit from its use.

One proposed solution for managing Internet material in an organized, user-friendly format is the implementation of a web portal. A web portal is a site that serves as a single point

of access to information collected from different sources and presented in multiple formats. Some common features of portals include personalized navigation, for example, "quick links" to frequently accessed information pages, directory-based information structure, community-building tools such as chatrooms, bulletin boards, and emailing lists, user authentication (log in and password), and subject-specific search functionality. Web portals have recently gained in popularity as they have been successfully implemented in a number of clinical settings, such as nursing [10], mental health [11], government disaster preparation [12], patient diabetes information [13], and the MedEdPORTAL implemented by The Association of American Medical Colleges [14]. The general consensus from these studies has been that web portals require initial planning and subsequent maintenance in order to remain relevant and effective but when designed appropriately, this online educational format is robust, easily accessible, and associated with excellent outcomes. While there is limited information regarding the concept of utilizing a portal for medical education purposes, it is reasonable to consider that these benefits recognized in clinically focused web portals would translate effectively for a medical-education-related web portal.

A recent study assessing electronic radiology teaching files for first year Gross Anatomy at our institution suggested the potential need for an improved organization and customization [15]. In its first year, there were 9% of students who reported that they did not find the material user-friendly and over one third of students did not utilize the resource. Based on this assessment as well as a previously defined goal of creating a longitudinal teaching resource for medical student, a decision was made to develop a web portal with several key changes to the existing web content to better organize the educational material. The primary purpose of the present study was to present rational for an approach that was utilized to develop internet-based Gross Anatomy material. Implementation of this teaching resource was assessed by evaluating student opinion regarding its usefulness, determining whether there was any correlation with how the students performed on their anatomy tests and the usage of the web teaching files, measuring student usage patterns of the material, and noting whether there were any design or technical difficulties when developing and managing the web site.

2. Materials and Methods

One of the goals of first-year Anatomy curricular redesign efforts at the Johns Hopkins University School of Medicine was to further integrate Radiology into the coursework. The initial efforts for this integration were centered on developing a Medical-Imaging-Resource-Center (MIRC-) based website with relevant teaching files to supplement topics discussed in lecture and corresponding gross dissections [15]. The goal of the present study was to improve on these initial efforts through the creation of a web portal that would organize existing teaching files as well as newly created educational resources and more fully integrate this material into the existing Anatomy coursework.

A survey from the previous year with student feedback from initial efforts in developing Radiology teaching files in a web-based format for Anatomy was reviewed. The team of attending, residents, and medical students working on the second iteration of development used this feedback to identify several possible areas for improvement with the goal for improved user friendliness and increased utilization of the material. Some of the key changes included integration of the material into a web portal, development of Lab and Study Companion components, and a set of organized links to access the material rather than requiring the user to type in search criteria. The list of features that were created and the rational for their implementation are provided in Table 1.

Joomla 1.5 (Open Source Matters, Inc, New York, NY) was utilized as a content management system for creating the web content. Joomla is an open-source application that is freely available on the Internet. It provided the ability to organize and keep track of all content as well as constantly update cases and documents without republishing the web page.

In order to expand the content that would be offered via the web portal, a search for relevant images within the past year was conducted using the Johns Hopkins Hospital Emageon Ultravisual (AMICAS, Inc, Boston, MA) picture archiving and communication system (PACS). There was no copyright protection for these images developed in this iteration of the site development. Although the site was password protected, there was no functionality limiting copying of images from the site by students. This issue will be further addressed in future iterations of the web site development. The effort to obtain several relevant images for each anatomic site was largely in response to student feedback from the prior year that suggested additional imaging teaching files would be beneficial. In order to expand the MIRC content already available, the goal of case acquisition this year was directed towards finding CT and MRI cases where multiple slices could be viewed for each case. Similar to the existing teaching files, the new cases included normal anatomy as well as cases with simple pathology. The cases were initially identified by two of the authors and subsequently reviewed by the senior authors before incorporation into teaching cases. Once selected, the image sets were saved in standard tagged image file format and animated with Macromedia Flash using an open-source student PACS module created by students and residents at the University of Medicine and Dentistry of New Jersey. The new modules allowed users to scroll through images, zoom, and pan while also interacting with labeled structures within the image sets. The decision to utilize Flash was impart based on familiarity of the product by the student developers. In addition, while evaluation of MIRC demonstrated excellent static image teaching file development, it had less robust capabilities compared to the Joomla/Flash combination option for developing more dynamic teaching files with scrolling and highlighting.

The new student PACS modules were combined with last year's MIRC cases to create teaching files that could be accessed during lecture by the instructors and by the anatomy students for review during and following anatomy

Table 1: Rational and features of newly created Radiology web portal for Gross Anatomy.

Goal/Rational	Feature	Description
Provide multiple formats for viewing and learning Radiology.	Utilized MIRC, Flash, and Joomla for Creating Teaching Files	MIRC provides excellent functionality for developing static single image teaching files. Macromedia Flash using an open-source student PACS module and Joomla content management system readily allowed for creation of teaching files with multiple-level cross-sections, and animations.
Provide single site for Radiology teaching material that students will utilize starting day one Gross Anatomy and then throughout medical school.	Home Page	Structured Web Portal with an integrated anatomy component.
Begin to expose students to clinical application of anatomy.	Cases of the Week	Clinical cases with relevant findings on imaging updated on homepage to correspond to lectures.
Provide students with direct correlations between cadaver anatomy and imaging.	Laboratory Companion	Feature of Web Portal providing imaging relevant to the day's dissection.
Provide content that allows students to identify labeled anatomy on imaging.	Study Companion	Feature of Web Portal providing labeled images and cross sectional modules.
Ensure students recognize reasoning for integrating Radiology and Anatomy.	Module Goals	Clearly stated goals provided on home page.
Provide students with a roadmap to optimize use of Radiology to learn Anatomy.	Methods for Achieving Goals	Discussed in lecture on first day of class and clearly stated on home page.
Allow Radiology files to be reviewed by anatomic site.	Organization of Files	Students click links that instantly bring up files organized by anatomic site.
Facilitate web site navigation by giving quick views of available material.	Preview of Teaching Files	Students click thumb nail with an image preview as well as text description.
Develop site that will serve as a platform for Radiology learning throughout medical school.	Longitudinal Educational Components	Web Portal provides additional components for basic Medicine and Surgery clinical rotations.
Reflect importance of cross-sectional imaging in clinical medicine.	Cross Section Teaching Files	Static images plus new cross section files that allow scroll, pan, and zoom.
Provide lecture presentations for preview and review of material.	Lecture material	Lecture PowerPoints made available via link on the Web Portal.
Introduce students to other existing resources for learning Radiology and Gross Anatomy.	Additional Learning Tools	Information provided in syllabus and links to resources provided on the web portal.
Introduce students to advancements being made in Radiology which may have future clinical implementation.	Anatomy TV	3D video anatomy teaching files available

lectures. MIRC files which were created last year were incorporated into the web site as thumbnails with hyperlinks to the original content, while new thumbnails were created to hyperlink to the students PACS cases. The web portal was designed such that all teaching files were organized by anatomical region. These anatomical regions were defined based on the existing syllabus for the anatomy course. The files were further separated into tutorial files and quiz files. In total, over 100 teaching files were provided (Tables 2 and 3).

In order to create interactive teaching files, relevant anatomy was identified and highlighted on each slice of an image set. A set of questions or relevant teaching points were then linked to each structure so that if the structure was selected on any slice where it could be seen, the questions or teaching points would then appear on the right

Table 2: Characterization of teaching files by question type.

Anatomical region	Tutorials	Quizzes	Normals	Abnormals
Thorax	11	18	15	14
Abdomen	7	22	11	18
Pelvis	3	7	7	3
Limbs	9	18	10	17
Spine	1	2	1	2
Head and neck	2	4	5	1
Total	33	71	49	55

side of the screen. Figure 1 displays a sample tutorial case where the arch of the aorta was highlighted and relevant information was displayed for that structure. In Figure 2, a quiz case is displayed where the ascending aorta has
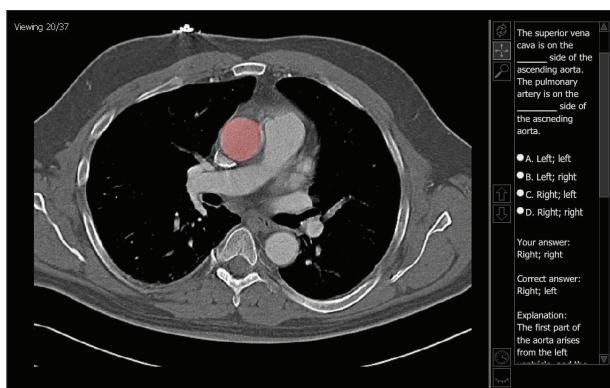
FIGURE 1: This is a screen-capture of one of the Thorax tutorial files. After clicking on a structure within the image, the structure will highlight and information will be provided about the structure on the right-hand side of the screen. In this example, the arch of the aorta has been selected and information regarding its origin, course, and branches has been provided.
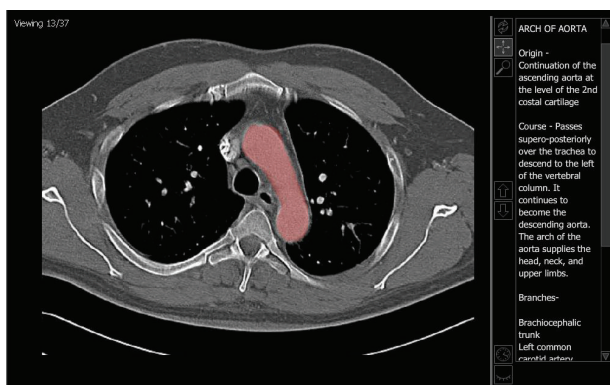

FIGURE 2: This image illustrates an example of one of the Thorax quiz files. After clicking on a structure within the image, the structure will be highlighted and a question regarding that structure will appear on the right-hand side of the screen. In this example, the ascending aorta has been selected and the correct answer has been chosen displaying an explanation.

TABLE 3: Characterization of teaching files by imaging modality.

Anatomical region	CT	MRI/MRA	US	Plain film	Angiography (Fluoroscopy)
Thorax	9	3	0	15	2
Abdomen	14	0	1	11	3
Pelvis	6	0	0	4	0
Limbs	1	0	0	25	1
Spine	0	0	0	3	0
Head and neck	1	4	0	1	0
Total	31	7	1	59	6

been highlighted prompting a multiple choice question related to this structure. For each of the tutorials, there was a page of instructional text, with one associated image set as demonstrated in Figures 1 and 2 and a corresponding set of relevant multiple choice questions.

The web portal was introduced to the medical students on the first day of their anatomy class. The rational for presenting the portal on the first day was to provide students a roadmap to optimize use of Radiology to learn Anatomy and to begin to get them comfortable with the basic layout of the web site. The web address was provided and basic navigation through the site was reviewed. The students were informed that the homepage would be updated a few days prior to each radiology lecture to include pertinent cases (Figure 3). They were required to look over those selected cases prior to lecture and advised to look over the additional cases found in the corresponding anatomical link for further review.

Each radiology lecture was divided into two one-hour segments. During the first hour, the lecturer presented a PowerPoint (Microsoft Corporation, Redmond, WA) lecture on material corresponding to the gross dissection scheduled for that day. The students were then given a five-minute break and asked to close all laptops before the second session began. Next, the lecturer broke the classroom up into small groups based on where the students were sitting and quizzed them on each of the cases found on the homepage of the web portal for that day. This process was repeated for each of the radiology-based lectures so that the students were aware of the expectation that they should be familiar with the corresponding cases found on the web portal homepage.

Following the completion of the Gross Anatomy course (Fall 2010), a fourteen question, web-based survey was distributed to the Anatomy students. The survey was similar to the one distributed to the first-year medical students the previous year (Fall 2009) [15]. Figure 6 provides a complete list of the questions on the survey. In order to evaluate the impact of the web portal compared to the previously available teaching files, the results of the survey from the current year were compared to the results from the previous year.

In order to quantify the utilization of the web site during the anatomy course, a StatistX module was installed into the Joomla content manager. This module allowed a hit counter to be incorporated into the web site which would keep track of all web traffic received by the site. The module provided daily activity, hourly reports, top ten pages hit, and the last twenty pages visited. This module provided information regarding when the students were utilizing the website the most and what content they were looking at. IP addresses were also provided in the statistics indicating whether the students preferred to access the material on or off campus. As previously noted, the teaching files were integrated to a greater extent into the coursework by including the material in discussion groups rather than the lecture-only format utilized during the previous year. The server data from the current year was compared to the server data from the previous year to identify any changes in the student utilization patterns after these changes in the structure of the coursework.

Head and neck introduction

Welcome to the head and neck anatomy section of the TeamRads anatomy module. The imaging cases in this section are divided into in two parts: tutors and quizzes

Tutors labeled cross sectional images made with student PACs and MIRCS
Quizzes designed to teach anatomy in the context of abnormal findings

Abbreviations: AP (antero-posterior), PA (postero-anterior), CT (computed tomography), CTA (computed tomography angiogram), MR (magnetic resonance), MRA(magnetic resonance angiogram)
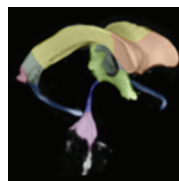
Head CT (axial)
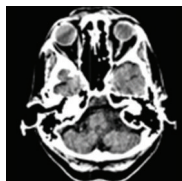
Click on the image
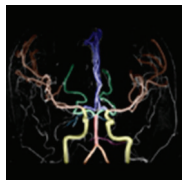Description: guide to cross-sectional anatomy as seen on a single head CT slice

Cerebral ventricular system

Click on the image
Description: guide to anatomy of the cerebral ventricles

Cerebral arterial system

Click on the image
Description: guide to major arteries of the anterior and posterior circulation

Head and neck radiograph (lateral)

Click on the image
Description: guide to anatomy of the head and neck as seen on a lateral radiograph

FIGURE 3: This screen-capture demonstrates the dynamic portion of the web portal home page which provided prelecture material. For this example, the teaching files were provided on the home page a few days prior to the head and neck imaging lecture. The students were expected to review the teaching files prior to lecture.

3. Statistical Analysis

After collecting the responses to the web-based survey, the data was exported from the survey site (http://surveymonkey.com) to spreadsheet format for aggregating and graphing the data. The spreadsheet data was imported into SPSS version 13.0 software (SPSS, Chicago, Illinois) for additional data analysis and statistical calculations. Comparisons of proportions for student responses for the current year to the prior year were made utilizing a chi-square analysis with a Yate's correction. A Mann-Whitney rank sum test was conducted to compare the mean values of the student responses. P values less than 0.05 were considered statistically significant.

4. Results

The demographic profile of the students who responded to the web-based survey this year was similar to the prior year. There were 87 of 120 medical students (73%) who completed the survey this year compared to 71% who completed the survey the previous year ($P = 0.886$). In both cohorts, the majority of the students was between 22 and 25 years old and had an undergraduate degree in biology. The only difference in demographics noted between the two groups was that the more recent cohort of students had a smaller percentage of Fine Arts majors (5% compared to 15%, $P = 0.036$).

Compared to the previous electronic teaching files, the new content received better evaluations for user friendliness and usefulness (Table 4). The mean score for usefulness of the web portal content was 3.3 points (helpful to very helpful) compared to 1.5 points (not helpful to somewhat helpful) for the previous material ($P < 0.001$). When excluding the 0 point scores of the students who did not use the online teaching files last year, the mean score improved from 1.5 to 2.6 points (somewhat helpful to helpful). However, the 2.6 points remained statistically less than the 3.3 point rating for the web portal ($P < 0.001$). Similarly, the new web material was rated as being more user friendly 3.1 points (good to excellent) versus 2.3 points (satisfactory to good) even after correcting again for the students who did not use the online content ($P < 0.001$).

The primary reason students utilized the resources was to review material that was going to be tested (Figure 4). There were 52 (60%) students who ranked this as the number one reason for accessing the teaching files, and 67 (77%) students ranked it as either the no. 1 or no. 2 reason they used the web material. The number of students who indicated that the teaching files were used because they helped to better understand anatomical relationships was only slightly less with 66 (76%) students ranking this option as either their no.1 or no. 2 choice. There were few students who indicated that their primary reason for using the teaching files was

TABLE 4: Comparison of student opinion of Radiology Teaching Files from Fall 2009 versus Fall 2010.

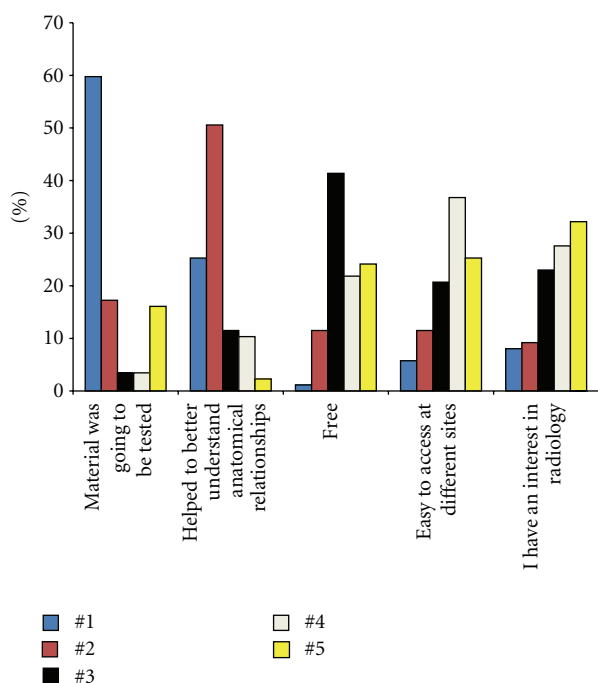| Data	Searchable Database (2009)	Web Portal (2010)	P value
Helpful in exam preparation?			<0.001*
Very helpful	8 (9%)	40 (46%)	
Helpful	16 (19%)	36 (41%)	
Somewhat helpful	22 (26%)	9 (10%)	
Not helpful	4 (5%)	2 (2%)	
Did not use	35 (41%)	0 (0%)	
user-friendly?			<0.001*
Excellent	3 (4%)	28 (32%)	
Good	16 (19%)	41 (47%)	
Satisfactory	23 (27%)	16 (18%)	
Poor	8 (9%)	2 (2%)	
Did not use	35 (41%)	0 (0%)	

* Statistically significant.

FIGURE 4: This bar graph illustrates the responses of the students regarding their ranking of why they utilized the Radiology teaching files.
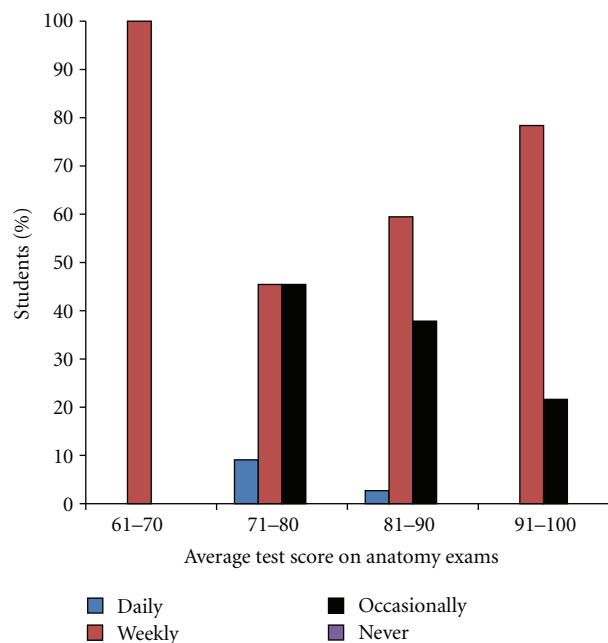

FIGURE 5: This bar graph groups the students by the performance on the Gross Anatomy exams and depicts how frequently they utilized the Radiology teaching files.

averages) to utilize the web portal more frequently than the 71-to-80 and 81-to-90 groups (Figure 5). However, there were insufficient numbers of students in the various test score groups to perform a chi-square analysis with any sufficient degree of certainty.

There were no students who completed the survey that did not use the radiology-based teaching materials available on the web site. This finding was consistent with required prelecture study files and subsequent review files that were provided as study aids for similar material that would be tested. The web server traffic pattern demonstrated a baseline of 30 to 40 hits per day. The number of hits increased to over 100 during the two to three days prior to an exam.

There were minimal technical or design difficulties in the creation and maintenance of the web portal. After being introduced to the web portal on the first lecture, no students reported any difficulty accessing the Radiology teaching files from home or at the school computer labs. Trials of accessing the site with various web browsers, including Internet Explorer 8, Safari 4, Flock 2, Chrome 3, Opera 10, Netscape Navigator 9, and Firefox 3.5, demonstrated no loss of functionality. There were no instances where the server went down throughout the course. At the end of the course, there were multiple students who suggested that the functionality of the online PACS modules needed to be improved. Students expressed frustration with the fact that the modules required the student to identify a structure correctly before moving to the next question. For example, one student noted that "It would be really helpful if the online modules allowed you to get a hint if you cannot find a structure. The way the quizzes are set up currently, if you cannot find something, you just have to skip it and move

because they were free. However, many students ranked this as their second or third reason for utilizing the site, and this was the third highest ranked choice overall.

The numbers of students in each of the test score categories were 2 students with average scores 61 to 70, 11 students with scores 71 to 80, 37 students with scores 81 to 90, and 37 students with scores 91 to 100. There appeared to be a trend for the highest scoring students (91 to 100

jhurads4anatomy.com online radiology teaching files survey

1. Gross anatomy radiology online teaching files (jhurads4anatomy.com) survey

1. How old are you?

○ <22 years ○ 22 to 25 years ○ >25 years

2. What was your undergraduate degree?

○ Biology ○ Chemistry or physics ○ Computer science ○ Engineering ○ Fine arts ○ Other

3. Do you have a higher degree?

☐ Masters ☐ MPH ☐ Other
☐ PhD or doctorate ☐ MBA

4. What was your average score on the anatomy radiology image quizes?

○ 0–50 ○ 51–60 ○ 61–70 ○ 71–80 ○ 81–90 ○ 91-100

5. How helpful do you find each of the following in your preparation for the anatomy exams?

	0 = did not use	1 = not helpful	2 = somewhat helpful	3 = helpful	4 = very helpful
The online radiology teaching files	○	○	○	○	○
Other online resources	○	○	○	○	○
Lectures	○	○	○	○	○
Textbooks	○	○	○	○	○
Anatomy Atlas	○	○	○	○	○
Gross dissection	○	○	○	○	○
Other	○	○	○	○	○

6. Please rank the reasons you utilized the online Radiology teaching files.

	#1	#2	#3	#4
The material was going to be tested.	○	○	○	○
The files were helpful as a supplement for learning anatomy	○	○	○	○
The files were free	○	○	○	○
The files were easy to access at different sites	○	○	○	○

7. On average, how frequently do you use the online radiology teaching files?

○ Daily ○ Weekly ○ Occasionally ○ Never

8. Where did you most often utilize the online radiology teaching files resource?

○ Never used ○ From home ○ Student computer lab ○ Other

9. How user-friendly did you find the online radiology teaching files?

○ Did not use ○ Poor ○ Satisfactory ○ Good ○ Excellent

10. How helpful did you find each of the components of the online radiology teaching files?

	0 = did not use	1 = not helpful	2 = somewhat helpful	3 = helpful	4 = very helpful
Normal labeled anatomy image	○	○	○	○	○
Abnormal cases with radiologic findings	○	○	○	○	○

11. What anatomy do you think you would have benefited from seeing more examples in the online radiology teaching files (check all that apply)?

☐ Abdomen ☐ Extremities ☐ Head/neck
☐ Thorax ☐ Pelvis

12. How helpful is the integration of radiology into first year gross anatomy?

○ Not helpful ○ Somewhat helpful ○ Helpful ○ Very helpful

13. How have the radiology lectures/online teaching files affected your interest in radiology?

○ Large decrease ○ Some decrease ○ No change ○ Some increase ○ Large increase

14. Any other comments or suggestions:

Figure 6

onto something else. The CTs would be much more helpful if it were possible to view an index of all of the labeled items." Similarly, another student is quoted as saying, "The website is a good start. I would want a system where the different parts of the radiographs are already labeled so that I do not have to randomly click around the image to find one tiny structure." Another area the students suggested for improvement was to add even more teaching files. 74 (85%) of the students indicated that they would benefit from more cases from one or more anatomic site. The most common sites indicated were head and neck ($n = 65$, 88%) and extremities ($n = 38$, 51%).

5. Conclusions

Recent student feedback at our institution suggested the need for a more organized approach for presenting the Radiology component of the first year medical school Gross Anatomy course. Based on feedback from earlier efforts and assessment of studies that have shown successful approaches for implementing web portals for clinical practice, efforts were made to better organize Radiology teaching files prepared for Gross Anatomy. In general, the results of the present study suggest that organizing web material to better correspond to Anatomy course work and providing it in a structured set of links in a web portal was associated with increased student satisfaction and utilization of the resource.

One of the factors that may have facilitated the development of a useful tool for Gross Anatomy students is that some of the authors are medical students or are only a few years removed from taking the course themselves and can relate to what material may be useful for Gross Anatomy study. This hypothesis is supported by a recent study by Rosenbaum et al. [16]. They evaluated medical student involvement in the development of a website to act as each individual medical student's homepage. They created a web portal that provided students with access to course material, evaluations, academic information, and community assets. Based on greater than 80% positive feedback regarding the web portal, they recommended that other medical schools that are creating and expanding digital resources should solicit the valuable input and perspective of medical students.

It was and will be difficult to analyze the effect of the web portal on student performance since it was felt to be inappropriate to withhold access from half the class for a controlled comparison. Our students are highly motivated and sophisticated learners, as well as "digital natives" accustomed to using web resources; it was felt their comments and satisfaction scores were legitimate metrics of utility or the resource. There also continue to be changes in the overall Gross Anatomy course structure and student testing reflecting as our medical school's new curriculum moves through its second year, further complicating comparison of test scores or grades from the initial year of web site usage to the second year with the improved/modified web material.

Although the primary objective for the present study was to create user-friendly teaching files for anatomy students, the ultimate goal of the Radiology research team working on this project was to create the foundation for a medical student and resident Radiology education web portal. The concept for the web portal was derived from previous studies at our institution that have highlighted the benefit of longitudinal directed teaching [7, 17]. For example, Feigin et al. reported that recall and retention toward the end of medical school was facilitated by providing preclinical instruction followed by review of the material later in school [7]. They reported that senior students benefited from previously received preclinical radiology training as they were able to improve their score on an anatomy quiz from an average of 4.42 (standard deviation 1.34) to a score of 8.65 (standard deviation 1.24) only three weeks later. The goal for the web portal in the present study is to provide a similar benefit but in an electronic format. The web portal design updates that have now been included in an effort to meet this goal are components for (1) imaging modules to be integrated into the basic clerkships (PRECEDE Modules for third year medical students), (2) lectures from The Johns Hopkins Basic Radiology Elective (for third- and fourth-year medical students), and (3) Johns Hopkins Radiology Resident Joint Procedure notes (for residents). For those students interested in pursuing a career in radiology or just looking for residency match advice, a residency application guide (*APPS of STEEL*) created by the senior author was also included. Finally, links to other recommended anatomy and radiology resources were incorporated into the site to allow students and residents to further their interest in the field.

While all of this functionality of the portal was customized for a single institution, the authors are assessing possible collaborations with other institutions. There is a potential to provide a more universal product. This product could potentially be provided to international colleagues who may not have the funds to develop a similar resource. To provide this outreach, it is conceivable that such a product could linked to be included under the umbrella of a larger entity with greater outreach such as the MedEdPORTAL.

The students indicated that the number one reason for accessing the files was to prepare for the material possibly being on the test. Although this may have been the primary incentive, it is important to note that regardless of the reason the students accessed the material initially, there were a large number of students who subsequently found the material to be user friendly and helpful in learning to identify anatomic structures. Furthermore, it is reasonable to expect students who are required to utilized material that will be tested to be more hypercritical of the material. As such, the improvements in reported user-friendliness of the electronic material are arguably more substantial. Of interest, students constantly came forward or emailed us during the semester to make constructive suggestions or to inquire about joining the project, also implying engagement. These findings suggest that Educators should recognize that by informing students that material will be on their tests, a majority if not all of the student body will review the resource. The goal of the Educator, however, should not only be to have students utilize the resource but to also provide material that is user friendly and provides optimal educational value. If Educators are considering a digital

format for distributing material, a structured web site can be a tool to provide easy access, in a user friendly format.

Similar to other questionnaire-based studies, one of the limitations of the present study is the number of students who do not participate. As previously noted, the response rate of 73% for the present study was similar to the rate for the survey from the previous year. This response rate is approximately one standard deviation above the normal response rates reported in the literature [18]. While it is uncertain how the remaining 27% of students would have answered the survey questions, we believe that based on the reported demographics and test scores that the study population was a fair representation of the class on a whole. Another limitation is that the survey was not formally validated prior to online implementation. However, students did not report problems when completing the survey, and standard survey functionality provided by the vendor was utilized to ensure students completed all required questions. One other limitation was the accuracy of the self-reported test scores. However, the range of scores reported appeared to reflect the class actual performance and with no identifiers for the responses the students had no incentive to not report their true performance.

In summary, this study suggests that students have a favorable impression of having a web site with organized Radiology resources for first-year Gross Anatomy. We are encouraged by the increased utilization of this resource compared to the resources provided last year. There remains room for improvement with students suggesting that they would benefit from more teaching files and from modules that allow for a summary view rather than requiring point by point walk through of the material. Based on the first two years' experience and survey feedbacks, and our observations and increasing experience, we will further expand and refine this teaching resource before the 2011 Gross Anatomy course and hope to be able to further explore and assess the initial trends and findings discussed here. Additional studies are being planned that will further assess other components of the web portal and the efficacy of the site as a longitudinal educational resource for students throughout medical school.

References

[1] A. Winkelmann, "Anatomical dissection as a teaching method in medical school: a review of the evidence," *Medical Education*, vol. 41, no. 1, pp. 15–22, 2007.

[2] A. R. A. Choi, R. Tamblyn, and M. D. Stringer, "Electronic resources for surgical anatomy," *ANZ Journal of Surgery*, vol. 78, no. 12, pp. 1082–1091, 2008.

[3] W. E. Erkonen, M. A. Albanese, W. L. Smith, and N. J. Pantazis, "Effectiveness of teaching radiologic image interpretation in gross anatomy: a long-term follow-up," *Investigative Radiology*, vol. 27, no. 3, pp. 264–266, 1992.

[4] L. M. McNiesh, J. E. Madewell, and R. M. Allman, "Cadaver radiography in the teaching of gross anatomy," *Radiology*, vol. 148, no. 1, pp. 73–74, 1983.

[5] N. F. Jafri, P. Wu, L. Stanfield, and P. J. Slanetz, "Use of radiologic imaging to enhance physical diagnosis instruction in the preclinical curriculum," *Academic Radiology*, vol. 15, no. 7, pp. 942–947, 2008.

[6] H. Petersson, D. Sinkvist, C. Wang, and O. Smedby, "Web-based interactive 3D visualization as a tool for improved anatomy learning," *Anatomical Sciences Education*, vol. 2, no. 2, pp. 61–68, 2009.

[7] D. S. Feigin, D. Magid, J. G. Smirniotopoulos, and S. J. Carbognin, "Learning and retaining normal radiographic chest anatomy. Does preclinical exposure improve student performance?" *Academic Radiology*, vol. 14, no. 9, pp. 1137–1142, 2007.

[8] W. Stanford, W. E. Erkonen, M. D. Cassell et al., "Evaluation of a computer-based program for teaching cardiac anatomy," *Investigative Radiology*, vol. 29, no. 2, pp. 248–252, 1994.

[9] M. L. Richardson, "A World-Wide Web radiology teaching file server on the Internet," *American Journal of Roentgenology*, vol. 164, no. 2, pp. 479–483, 1995.

[10] T. B. Campbell, "Role socialization: designing a web-based program to orient new school nurses," *Journal of School Nursing*, vol. 25, no. 2, pp. 117–125, 2009.

[11] H. Christensen, K. Murray, A. L. Calear, K. Bennett, A. Bennett, and K. M. Griffiths, "Beacon: a web portal to high-quality mental health websites for use by health professionals and the public," *The Medical Journal of Australia*, vol. 192, no. 11, pp. S40–44, 2010.

[12] J. L. Bader, J. Nemhauser, F. Chang et al., "Radiation event medical management (REMM): website guidance for health care providers," *Prehospital Emergency Care*, vol. 12, no. 1, pp. 1–11, 2008.

[13] C. Nordqvist, L. Hanberger, T. Timpka, and S. Nordfeldt, "Health professionals' attitudes towards using a web 2.0 portal for child and adolescent diabetes care: qualitative study," *Journal of Medical Internet Research*, vol. 11, no. 2, article e12, 2009.

[14] R. J. Reynolds, "MedEdPORTAL: educational scholarship for teaching," *Journal of Continuing Education in the Health Professions*, vol. 28, no. 2, pp. 91–94, 2008.

[15] D. R. Marker, A. K. Bansal, K. Juluru, and D. Magid, "Developing a radiology-based teaching approach for gross anatomy in the digital era," *Academic Radiology*, vol. 17, no. 8, pp. 1057–1065, 2010.

[16] B. P. Rosenbaum, T. L. Gorrindo, S. G. Patel, M. P. McTigue, S. M. Rodgers, and B. M. Miller, "Medical student involvement in website development," *Medical Teacher*, vol. 31, no. 7, pp. 627–633, 2009.

[17] D. Magid, D. W. Hudson, and D. S. Feigin, "Chest radiographic anatomy retention. The impact of preclinical groundwork on clinical recall in two schools," *Academic Radiology*, vol. 16, no. 11, pp. 1443–1447, 2009.

[18] Y. Baruch and B. C. Holtom, "Survey response rate levels and trends in organizational research," *Human Relations*, vol. 61, no. 8, pp. 1139–1160, 2008.

Review Article

Ultrahigh Voltage Electron Microscopy Links Neuroanatomy and Neuroscience/Neuroendocrinology

Hirotaka Sakamoto[1] and Mitsuhiro Kawata[2]

[1] *Laboratory of Neuroendocrinology, Ushimado Marine Institute, Graduate School of Natural Science and Technology,*
  Okayama University, Kashino, Ushimado, Setouchi, Okayama 701-4303, Japan
[2] *Department of Anatomy and Neurobiology, Kyoto Prefectural University of Medicine, Kawaramachi-Hirokoji, Kamigyo-ku,*
  Kyoto 602-8566, Japan

Correspondence should be addressed to Hirotaka Sakamoto, hsakamo@uml.okayama-u.ac.jp

The three-dimensional (3D) analysis of anatomical ultrastructures is extremely important in most fields of biological research. Although it is very difficult to perform 3D image analysis on exact serial sets of ultrathin sections, 3D reconstruction from serial ultrathin sections can generally be used to obtain 3D information. However, this technique can only be applied to small areas of a specimen because of technical and physical difficulties. We used ultrahigh voltage electron microscopy (UHVEM) to overcome these difficulties and to study the chemical neuroanatomy of 3D ultrastructures. This methodology, which links UHVEM and light microscopy, is a useful and powerful tool for studying molecular and/or chemical neuroanatomy at the ultrastructural level.

1. Introduction

The three-dimensional (3D) analysis of anatomical ultrastructures is extremely important in most fields of biological research. However, it is considerably difficult to perform a 3D image analysis of exact serial sets of ultrathin sections. Although 3D reconstruction from ultrathin sections ($\sim$100 nm thickness) has been generally used to obtain 3D information, this technique is applicable only for small specimen areas because of the technical and physical difficulties under the transmission electron microscopy, restricted to approximately 1 mm^2 area. On the other hand, due to tremendous development of various techniques in molecular biology (e.g., green fluorescent proteins and their color variants), as well as the development of live imaging techniques, the structure of biological molecules and their functional changes are calculated and visualized in 3D at subnanometer resolution [1, 2]. With the aid of confocal laser scanning microscopy, it is now possible to image and quantify the 3D organization of these cell processes; however, the detailed morphology of the complicated terminal processes of these cells remains obscure because of the insufficient spatial

resolution of light microscopy and visualization methods that depend on fluorescence [3–6]. In addition, unstained domains are very difficult to recognize [3]. In contrast, conventional transmission electron microscopy provides extremely detailed and fine structural information, but the images obtained are mostly 2D due to the physical properties of this imaging technique (use of ultrathin sections). Consequently, it is too difficult to relate electron micrographs to the 3D structures of cells.

The high penetration power of electrons at an ultrahigh accelerating voltage enables the examination of thick sections of biological specimens. This property of ultrahigh voltage electron microscopy (UHVEM) is particularly useful for the morphological study of the central nervous system [7]. Differences in behavioral neuroendocrinology (i.e., control of reproduction, sexual behavior, and food intake) are commonly correlated with differences in neuroanatomy. In the central nervous system, a population of synaptic inputs from a brain nucleus can influence axosomatic synapses whereas the structural analysis of multiple major synaptic inputs into the dendrites located outside the nucleus is difficult to perform methodologically. However, using UHVEM

we overcame these difficulties and described a powerful methodology to study the chemical neuroanatomy of 3D ultrastructures [8, 9]. Here, 3D analysis of neuroanatomy at the ultrastructural level using UHVEM is summarized.

2. Golgi Impregnation

The gross morphology of neurons and glial cells have been described in detail using light microscopy in combination with various metal impregnation techniques such as Golgi silver staining [10]. The Golgi method is very useful and has been utilized by many neuroanatomists over the past century. Subsequently, the rapid Golgi impregnation procedure, a newly developed method, is also applied in qualitative and quantitative characterization of neuronal morphology analyses both at light and electron microscopic levels [11–14]. We used rapid Golgi impregnation, in combination with UHVEM to visualize neuronal structures at the electron microscopic levels.

Rats were overdosed with sodium pentobarbital (100 mg/kg body weight), and perfusion fixed using 2.5% paraformaldehyde and 2.5% glutaraldehyde in a 0.1 M phosphate buffer (PB; pH 7.4). Brain sections (100–300 μm thickness) were prepared using a microslicer (Dosaka EM, Kyoto, Japan). After the sections were processed using the rapid Golgi technique as described elsewhere [11, 12], the tissues were dehydrated and flat embedded in epoxy resin and preliminarily examined using a light microscope [8]. Appropriately Golgi-impregnated neurons in the hippocampus were selected for the following procedures. Thick sections of selected neurons were remounted for further sectioning. Two to five-micrometer thick sections were cut using an ultramicrotome (Ultracut, Reihert-Jung, Wetzlar, Germany) and collected on copper grids. Each specimen was first photographed using a light microscope for reference purposes, then examined using UHVEM (Hitachi H-1250 M; National Institute for Physiological Sciences, Okazaki, Japan) at an accelerating voltage of 1,000 kV. Stereopaired photomicrographs were prepared using UHVEM by tilting the specimen stage $\pm 8°$.

In the hippocampus, excitatory synapses develop very rapidly and most of the components necessary to perform their complex functions can be found during the early postnatal period [15]. Over 90% of the excitatory synapses are formed on small postsynaptic protrusions that are known as "dendritic spines" [16]. Dendritic spines are the major excitatory input sites of the hippocampal pyramidal neurons and are related to learning, memory, functional recovery, and plasticity of the central nervous system [17]. Accordingly, the precise morphometry of these structures is indispensable for a better understanding of neuronal function and useful for modeling neuronal circuitry. A 3D morphometric study was performed using stereopaired UHVEM images. First, nontilted and $\pm 8°$-tilted UHVEM images of 4-μm thick specimens were examined. UHVEM stereoscopic analysis of the thick Golgi-impregnated materials revealed that the thorny processes appeared as a bunch of grapes, consisting of long protrusions that were studded with many bulbous
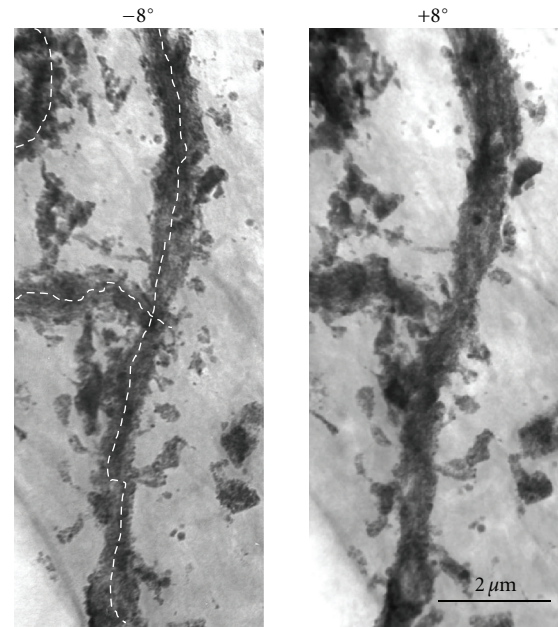

FIGURE 1: Stereopaired UHVEM images obtained by tilting the specimen stage $\pm 8°$ to reveal the 3D structure of the impregnated Golgi dendrites of CA1 pyramidal neurons of the hippocampus.

appendages (Figure 1). Because dendritic spines are the major excitatory input sites of the neurons in the central nervous system [16], 3D morphometric analysis, in combination with Golgi impregnation and UHVEM stereopaired images, is very useful for elucidating the neural functions of living matter (Figure 1).

3. Retrograde Tracing and Immunocytochemistry

Onuf's nucleus, located in the ventral horn of the sacral spinal cord of many mammals, including humans, is a sexually dimorphic nucleus that innervates the perineal muscles that are involved in sexual behavior. In humans, it is a distinct group of neurons located in the ventral part of the anterior horn of the sacral region of the spinal cord involved in the maintenance of micturition and defecatory continence, as well as muscular contraction during orgasm [18]. The number of neurons in Onuf's nucleus is greater in males than in females [18–21]. On the other hand, the spinal nucleus of the bulbocavernosus (SNB) of rats, located in the lower lumbar and upper sacral spinal segments, is homologous to Onuf's nucleus in that it innervates the striated perineal muscles that are attached to the base of the penis [21–23]. The distribution of serotonergic fibers and terminals in this nucleus in rats is also different between the sexes (male dominant) [24–26]. SNB also plays a significant role in male sexual functions in the rat [22, 23, 27, 28]. Male rats have a larger and a greater number of SNB motoneurons than females; this dimorphism results from differences in perinatal androgen signaling through a mechanism mediated by the androgen receptor [22]. On the

other hand, we recently reported that a collection of neurons within the upper lumbar spinal cord (L3-L4 level) project axons with gastrin-releasing peptide (GRP) to the lower lumbar spinal cord, controlling male reproductive functions in rats [9, 29, 30]. It has also been reported that the sexually dimorphic distribution of GRP-immunoreactive fibers in the lower lumbar spinal cord is profoundly regulated by circulating androgen levels [31], mirroring changes in SNB motoneuron arborizations and other synaptic populations [23]. However, due to methodological difficulties, no direct evidence has been reported regarding GRP synaptic inputs to the SNB motoneurons. The aim of the current study was to determine the axodendritic synaptic inputs of GRP neurons that project into perineal SNB motoneurons and bulbocavernosus muscles. Immunoelectron microscopy, in combination with a retrograde tracing technique using UHVEM, was employed to visualize the 3D ultrastructures of the central nervous system [8].

Rats were deeply anesthetized using intraperitoneal injections of 50 mg/kg body weight sodium pentobarbital and bilaterally injected with 1 μL of 0.2% cholera toxin β subunit-horseradish peroxidase conjugate (CTb-HRP; List Laboratories, Cupertino, CA, USA) into the bulbocavernosus muscles. Rats were overdosed with sodium pentobarbital (100 mg/kg body weight) 48–96 h after the CTb-HRP injection, and then perfusion fixed with 4% paraformaldehyde, 0.2% glutaraldehyde, and 1.25% picric acid in a 0.1 M PB solution (pH 7.4). Spinal cords were immediately removed and immersed in the same fresh fixative for 3 h. Spinal sections (L5-L6 level; 30 μm thickness) were prepared using a microslicer (Dosaka EM). Next to visualize SNB somata and dendrites, retrogradely labeled with CTb-HRP, the tetramethylbenzidine (TMB)/diaminobenzidine- (DAB-) nickel method was performed as previously described [32]. Sodium tungstate was used as the stabilizer. Sections were then placed in a 0.1 M PB with 25% sucrose and 10% glycerol for 1 h for cryoprotection, then freeze-thawed using liquid nitrogen to enhance the penetration of the antibodies. After blocking with phosphate buffered saline (PBS; pH 7.4) containing 0.05% Triton X-100, 1% normal goat serum, and 1% BSA for 2 h, the sections were incubated in rabbit anti-GRP serum (Phoenix Pharmaceuticals, Burlingame, CA, USA) at a 1 : 5,000 dilution in the blocking solution, for 5 days at 4°C. After washing with PBS, the sections were treated with biotinylated goat anti-rabbit IgG (Nichirei, Tokyo, Japan), at a 1 : 1,000 dilution in the blocking solution for 3 h at room temperature. After washing with PBS, GRP immunoreactivity was developed using the streptavidin-biotin-HRP complex/DAB-nickel method, as previously described [29, 33]. After washing with 0.1 M PB, the sections were placed in a 0.1 M PB solution with 1% OsO$_4$ for 90 min, dehydrated, and flat embedded in epoxy resin. The embedded sections were viewed using an Olympus Optical BH-2 microscope (Tokyo, Japan), and regions that may contain GRP synapses were selected. These sections were further cut into serial 2 μm-thick semithin sections and collected on copper grids coated with collodion film. Each specimen was first photographed using a light microscope for reference purpose, then examined using UHVEM at an accelerating voltage of 1,000 kV and conventional transmission electron microscopy (EM; JEM-1220, JEOL, Tokyo, Japan) at an accelerating voltage of 80 kV. Stereopaired photomicrographs using UHVEM were prepared by tilting the specimen stage ±8°. Neuronal profiles were identified using the criteria described by Peters et al. [34].

Retrograde tracing is a reliable neuroanatomical method used to locate the somata and dendrites of the motoneurons that innervate the somatic muscles [29, 32, 35]. Neurons, retrogradely labeled with CTb-HRP, were visualized by the TMB method, and were observed only in the SNB at the fifth and sixth lumbar segments of the spinal cord. Using light microscopy, we found densely stained somata and dendrites that were diffusely distributed, or in a dot-like fashion, and often appeared to make close appositions with immunolabeled GRP-immunoreactive axons. These appositions were particularly abundant in the dorsal gray commissure (DGC). GRP-immunoreactive somata were not observed in the SNB.

In terms of their ultrastructures, the TMB reaction products in the CTb-HRP-labeled SNB neurons were also diffusely distributed within the cytoplasm, as revealed by UHVEM and conventional EM [8, 32]. The TMB reaction products were more electron-dense than the DAB reaction products of the GRP-immunoreactive axons [8]. The TMB reaction products were electron-dense small bodies, with a 3D radial spindle-like shape in clusters of various sizes within the cytoplasm and dendrites (Figure 2). The DAB reaction products were visualized as fine, fuzzy materials that were homogeneously distributed throughout the axons and terminals of the GRP neurons (Figure 2). Strikingly, the 3D TMB crystalline structures were clearly observed by UHVEM and were easily distinguishable from the DAB reaction products (Figure 2). Interestingly, 3D analysis with a polarizing lens revealed that some populations of the GRP-immunoreactive terminals possibly formed synaptic contacts with the SNB motoneurons [8]. GRP-immunoreactive axons were also found to wind around a single distal dendrite within the DGC. Taken together, these results suggest that GRP-containing afferents to SNB motoneurons regulate male sexual reflexes *via* these synapses, since the contraction of bulbocavernosus muscles is involved in penile erection [36].

Conventional EM method revealed synaptic inputs into the SNB motoneurons that innervate the bulbocavernosus muscles [8]. In the analysis of ultrathin serial sections we identified a single synaptic GRP input to a TMB-labeled dendrite; however, multiple inputs were not identified. Conventional EM analysis of the ultrathin serial sections (60-nm thick) only revealed a single synaptic input even though both GRP-immunoreactive fibers and SNB motoneuron dendrites are broadly distributed throughout the DGC. By studying the stereopaired UHVEM images, fine, 3D, axonal projections of GRP neurons to CTb-labeled SNB dendrites were observed in a wide but discrete area. Since the semithin sections (2 μm thick) were first visualized using light microscopy and then analyzed using UHVEM (Figure 2), this report is able to definitively conclude that the ability of UHVEM to detect synaptic formations is superior to conventional EM.
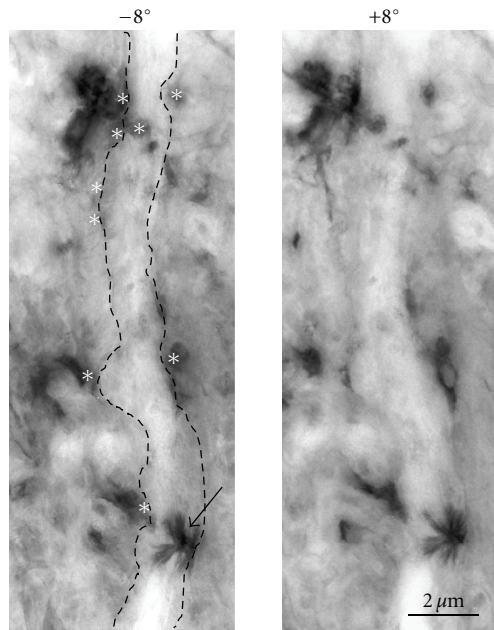
Figure 2: Stereopaired UHVEM images obtained by tilting the specimen stage $\pm 8°$ reveal the 3D structure of the axonal projections (white asterisks) of a single SNB dendrite. The arrow indicates an electron-dense TMB reaction product of an SNB dendrite with the characteristic radial structure. This figure was reproduced from the research by Sakamoto et al. [8] with permission.

4. Conclusions

Here, we summarize the 3D analysis of neuroanatomy at the ultrastructure level using UHVEM. Both UHVEM stereoscopy and morphometry are useful for elucidating the functions of living matter. These techniques can easily be combined with Golgi impregnation, conventional neurotracing, and/or immunoelectron microscopic methods to reveal the fine details of 3D neuroanatomy. In conclusion, we believe that this mixed methodology, which links UHVEM and light microscopy, is a useful and powerful tool for studying molecular and chemical neuroanatomy at the ultrastructural level.

Acknowledgments

References

[1] A. Miyawaki, "Fluorescence imaging of physiological activity in complex systems using GFP-based probes," *Current Opinion in Neurobiology*, vol. 13, no. 5, pp. 591–596, 2003.

[2] M. Nishi and M. Kawata, "Brain corticosteroid receptor dynamics and trafficking: implications from live cell imaging," *The Neuroscientist*, vol. 12, no. 2, pp. 119–133, 2006.

[3] P. V. Belichenko and A. Dahlström, "Studies on the 3-dimensional architecture of dendritic spines and varicosities in human cortex by confocal laser scanning microscopy and Lucifer Yellow microinjections," *Journal of Neuroscience Methods*, vol. 57, no. 1, pp. 55–61, 1995.

[4] S. Ebara, K. Kumamoto, K. I. Baumann, and Z. Halata, "Three-dimensional analyses of touch domes in the hairy skin of the cat paw reveal morphological substrates for complex sensory processing," *Neuroscience Research*, vol. 61, no. 2, pp. 159–171, 2008.

[5] H. Mukai, T. Kimoto, Y. Hojo et al., "Modulation of synaptic plasticity by brain estrogen in the hippocampus," *Biochimica et Biophysica Acta*, vol. 1800, no. 10, pp. 1030–1044, 2010.

[6] H. Cui, H. Sakamoto, S. Higashi, and M. Kawata, "Effects of single-prolonged stress on neurons and their afferent inputs in the amygdala," *Neuroscience*, vol. 152, no. 3, pp. 703–712, 2008.

[7] K. Hama and T. Kosaka, "Neurobiological applications of high voltage electron microscopy," *Trends in Neurosciences*, vol. 4, no. C, pp. 193–196, 1981.

[8] H. Sakamoto, T. Arii, and M. Kawata, "High-voltage electron microscopy reveals direct synaptic inputs from a spinal gastrin-releasing peptide system to neurons of the spinal nucleus of bulbocavernosus," *Endocrinology*, vol. 151, no. 1, pp. 417–421, 2010.

[9] H. Sakamoto, "The gastrin-releasing peptide system in the spinal cord mediates masculine sexual function," *Anatomical Science International*, vol. 86, no. 1, pp. 19–29, 2011.

[10] S. R. Cajal, *Histologie du Systeme Nerveux de l'Homme et des Vertebres*, Instituto Ramon y Cajal, Madrid, Spain, 1972.

[11] T. Kosaka and K. Hama, "Three-dimensional structure of astrocytes in the rat dentate gyrus," *Journal of Comparative Neurology*, vol. 249, no. 2, pp. 242–260, 1986.

[12] B. S. Shankaranarayana Rao, Govindaiah, T. R. Laxmi, B. L. Meti, and T. R. Raju, "Subicular lesions cause dendritic atrophy in CA1 and CA3 pyramidal neurons of the rat hippocampus," *Neuroscience*, vol. 102, no. 2, pp. 319–327, 2001.

[13] U. Tauer, B. Volk, and B. Heimrich, "Differentiation of Purkinje cells in cerebellar slice cultures: an immunocytochemical and Golgi EM study," *Neuropathology and Applied Neurobiology*, vol. 22, no. 4, pp. 361–369, 1996.

[14] M. Sojka, H. A. Davies, D. A. Rusakov, and M. G. Stewart, "3-Dimensional morphometry of intact dendritic spines observed in thick sections using an electron microscope," *Journal of Neuroscience Methods*, vol. 62, no. 1-2, pp. 73–82, 1995.

[15] G. Paxinos, *The Rat Nervous System*, Academic Press, San Diego, Calif, USA, 3rd edition, 2004.

[16] E. G. Gray, "Axo-somatic and axo-dendritic synapses of the cerebral cortex: an electron microscope study," *Journal of Anatomy*, vol. 93, pp. 420–433, 1959.

[17] M. Segal, E. Korkotian, and D. D. Murphy, "Dendritic spine formation and pruning: common cellular mechanisms?" *Trends in Neurosciences*, vol. 23, no. 2, pp. 53–57, 2000.

[18] B. Onufrowicz, "Notes on the arrangement and function of the cell groups in the sacral region of the spinal cord," *Journal of Nervous and Mental Disease*, vol. 26, pp. 498–504, 1899.

[19] S. Nakagawa, "Onuf's nucleus of the sacral cord in a south American monkey (Saimiri): Its location and bilateral cortical input from area 4," *Brain Research*, vol. 191, no. 2, pp. 337–344, 1980.

[20] M. Sato, N. Mizuno, and A. Konishi, "Localization of motoneurons innervating perineal muscles: a HRP study in cat," *Brain Research*, vol. 140, no. 1, pp. 149–154, 1978.

[21] N. G. Forger and S. M. Breedlove, "Sexual dimorphism in human and canine spinal cord: role of early androgen," *Proceedings of the National Academy of Sciences of the United States of America*, vol. 83, no. 19, pp. 7527–7531, 1986.

[22] S. M. Breedlove and A. P. Arnold, "Hormone accumulation in a sexually dimorphic motor nucleus of the rat spinal cord," *Science*, vol. 210, no. 4469, pp. 564–566, 1980.

[23] D. R. Sengelaub and N. G. Forger, "The spinal nucleus of the bulbocavernosus: firsts in androgen-dependent neural sex differences," *Hormones and Behavior*, vol. 53, no. 5, pp. 596–612, 2008.

[24] M. Kojima, Y. Takeuchi, M. Goto, and Y. Sano, "Immunohistochemical study on the localization of serotonin fibers and terminals in the spinal cord of the monkey (Macaca fuscata)," *Cell and Tissue Research*, vol. 229, no. 1, pp. 23–36, 1983.

[25] M. Kojima and Y. Sano, "Sexual differences in the topographical distribution of serotonergic fibers in the anterior column of rat lumbar spinal cord," *Anatomy and Embryology*, vol. 170, no. 2, pp. 117–121, 1984.

[26] M. Kojima, T. Matsuura, H. Kimura, Y. Nojyo, and Y. Sano, "Fluorescence histochemical study on the noradrenergic control to the anterior column of the spinal lumbosacral segments of the rat and dog, with special reference to motoneurons innervating the perineal striated muscles (Onuf's nucleus)," *Histochemistry*, vol. 81, no. 3, pp. 237–241, 1984.

[27] S. M. Breedlove and A. P. Arnold, "Hormonal control of a developing neuromuscular system. I. Complete demasculinization of the male rat spinal nucleus of the bulbocavernosus using the anti-androgen flutamide," *Journal of Neuroscience*, vol. 3, no. 2, pp. 417–423, 1983.

[28] S. M. Breedlove and A. P. Arnold, "Hormonal control of a developing neuromuscular system. II. Sensitive periods for the androgen-induced masculinization of the rat spinal nucleus of the bulbocavernosus," *Journal of Neuroscience*, vol. 3, no. 2, pp. 424–432, 1983.

[29] H. Sakamoto, K. I. Matsuda, D. G. Zuloaga et al., "Sexually dimorphic gastrin releasing peptide system in the spinal cord controls male reproductive functions," *Nature Neuroscience*, vol. 11, no. 6, pp. 634–636, 2008.

[30] H. Sakamoto and M. Kawata, "Gastrin-releasing peptide system in the spinal cord controls male sexual behaviour," *Journal of Neuroendocrinology*, vol. 21, no. 4, pp. 432–435, 2009.

[31] H. Sakamoto, K. Takanami, D. G. Zuloaga et al., "Androgen regulates the sexually dimorphic gastrin-releasing peptide system in the lumbar spinal cord that mediates male sexual function," *Endocrinology*, vol. 150, no. 8, pp. 3672–3679, 2009.

[32] J. J. L. van der Want, J. Klooster, B. Nunes Cardozo, H. De Weerd, and R. S. B. Liem, "Tract-tracing in the nervous system of vertebrates using horseradish peroxidase and its conjugates: tracers, chromogens and stabilization for light and electron microscopy," *Brain Research Protocols*, vol. 1, no. 3, pp. 269–279, 1997.

[33] H. Sakamoto, K. I. Matsuda, D. G. Zuloaga et al., "Stress affects a gastrin-releasing peptide system in the spinal cord that mediates sexual function: implications for psychogenic erectile dysfunction," *PLoS ONE*, vol. 4, no. 1, Article ID e4276, 2009.

[34] A. Peters, S. L. Palay, and H. F. Webster, *The Fine Structure of the Nervous System*, Oxford University Press, New York, NY, USA, 3rd edition, 1990.

[35] A. Matsumoto, P. E. Micevych, and A. P. Arnold, "Androgen regulates synaptic input to motoneurons of the adult rat spinal cord," *Journal of Neuroscience*, vol. 8, no. 11, pp. 4168–4176, 1988.

[36] B. D. Sachs, "Role of striated penile muscles in penile reflexes, copulation, and induction of pregnancy in the rat," *Journal of Reproduction and Fertility*, vol. 66, no. 2, pp. 433–443, 1982.

Review Article

The OPFOS Microscopy Family: High-Resolution Optical Sectioning of Biomedical Specimens

Jan A. N. Buytaert,[1] Emilie Descamps,[2] Dominique Adriaens,[2] and Joris J. J. Dirckx[1]

[1] *Laboratory of Biomedical Physics, University of Antwerp, Groenenborgerlaan 171, 2020 Antwerp, Belgium*
[2] *Evolutionary Morphology of Vertebrates, Ghent University, K. L. Ledeganckstraat 35, 9000 Gent, Belgium*

Correspondence should be addressed to Jan A. N. Buytaert, jan.buytaert@ua.ac.be

We report on the recently emerging (laser) light-sheet-based fluorescence microscopy field (LSFM). The techniques used in this field allow to study and visualize biomedical objects nondestructively in high resolution through virtual optical sectioning with sheets of laser light. Fluorescence originating in the cross-section of the sheet and sample is recorded orthogonally with a camera. In this paper, the first implementation of LSFM to image biomedical tissue in three dimensions—orthogonal-plane fluorescence optical sectioning microscopy (OPFOS)—is discussed. Since then many similar and derived methods have surfaced, (SPIM, ultramicroscopy, HR-OPFOS, mSPIM, DSLM, TSLIM, etc.) which we all briefly discuss. All these optical sectioning methods create images showing histological detail. We illustrate the applicability of LSFM on several specimen types with application in biomedical and life sciences.

1. Introduction

Serial (mechanical) histological sectioning (SHS) creates physical slices of fixed, stained, and embedded tissues which are then imaged with an optical microscope in unsurpassed submicrometer resolution. Obtaining these slices is however extremely work intensive, requires physical (one-time and one-directional) slicing and thus destruction of the specimen. A 2D sectional image reveals lots of histologically relevant information, but a data stack and its 3D reconstruction are even more essential for the morphological interpretation of complex structures, because they give additional insight in the anatomy. The SHS method requires semiautomatic to manual image registration to align all recorded 2D slices into order to get realistic 3D reconstructions. Often dedicated image processing of the sections is needed because of the geometrical distortions from the slicing.

A valuable alternative to achieve sectional imaging and three-dimensional modeling of anatomic structures can be found in the little known and relatively recent field of microscopy called (laser) light-sheet-based fluorescence microscopy or LSFM. These nondestructive methods

generate registered optical sections in real-time through bio(medical) samples ranging from microscopic till macroscopic size. LSFM can reveal both bone and soft tissue at a micrometer resolution, thus showing a large amount of histological detail as well.

The first account of the LSFM idea was published by Voie et al. in 1993 and applied to image the inner ear cochlea of guinea pig [1]. Their method was called orthogonal-plane fluorescence optical sectioning (OPFOS) microscopy or tomography. The motivations for the OPFOS invention were (1) the above-mentioned disadvantages of serial histological sectioning, (2) the typical photobleaching of fluorophores in conventional or confocal fluorescence microscopy, and (3) the fact that samples are optically opaque which means a limited penetration depth and inefficient delivering and collecting of light.

Surprisingly, all these problems can be avoided by combining two old techniques. Voie was the first to combine the Spalteholz method of 1911 [2] with the even older Ultramicroscope method of 1903 [3]. In most microscopy techniques, the same optical path and components are used for the illumination and the observation of light. Siedentopf and

Nobel Prize Winner Zsigmondy made a simple change of the optical arrangement in their ultramicroscopy setup by separating the illumination and viewing axis [3]. Furthermore, their illumination was performed by a thin plane or sheet of light. Orthogonal viewing or observation of this sheet offers full-field and real-time sectional information. Their method was originally developed for gold particle analysis in colloidal solutions with sunlight. OPFOS used the same optical arrangement but for tissue microscopy. The separation of the illumination and imaging axis combined with laser light sheet illumination only illuminates the plane that is under observation (in contrast to confocal microscopy) and thus avoids bleaching in sample regions that are not being imaged. Generally, samples are optically opaque so the plane of laser light cannot section the sample. Spalteholz introduced a clearing method which dates back exactly 100 years [2]. His museum technique is capable of making tissue transparent by matching the refractive index throughout the entire object volume by means of a mixture of oils with refractive indices close to that of protein. Submerged in this Spalteholz fluid, a prepared specimen appears invisible, with light passing right through it unscattered and without absorption. This clearing or refractive index matching is essential for the OPFOS technique to achieve a penetration depth of several millimeters. This procedure is followed by staining of the sample with fluorescent dye or just by relying on naturally occurring autofluorescence. The sectioning laser plane activates the fluorophores in the cross-section of sheet and sample, which are finally orthogonally recorded by a camera.

OPFOS utilizes yet a third method in conjunction with the two previous techniques when the specimen contains calcified tissue or bone. In this case, the calcium first needs to be removed before the Spalteholz procedure is applied. Bone cannot be made transparent, as the calcium atoms strongly scatter light.

Since 1993, many OPFOS-like derived methods were developed for tissue microscopy, all based on light sheet illumination. "LSFM" has become a broadly accepted acronym to cover the whole of these techniques. In the discussion, we will give a short overview of this OPFOS-derived LSFM microscopy family. First, we will explain in detail the specimen preparation and the optical arrangement of the original OPFOS setup. The remainder of this paper will serve to demonstrate some applications of OPFOS.

2. Materials and Methods

2.1. Specimen Preparation. In most LSFM methods, the biomedical tissue samples are severely limited in size, though for instance the LSFM implementations of Ultramicroscopy, HR-OPFOS, and TSLIM (cf. the discussion section) are capable of imaging macroscopic samples up to tens of millimeters [4]. In all cases, an elaborate specimen preparation is required.

 (i) Euthanasia: living animals cannot be used in combination with clearing solutions. In general, LSFM is thus mainly used *in vitro*. Clearing can be omitted, and living animals can be used if the species possesses a natural transparency at a certain developmental stage, for instance fish embryos [5, 6]. The embryos are immobilized by embedding in agarose.

 (ii) Perfusion: before dissecting a sample to the required dimensions, transcardial perfusion with phosphate buffered saline is useful as coagulated blood is difficult to clear with Spalteholz fluid [7–9]. If perfusion is omitted, bleaching is required.

 (iii) Fixation: immersion in 4% paraformaldehyde (10% formalin) for 24 h or more for preservation and fixation of the specimen.

 (iv) Bleaching: optional bleaching in 5% to 10% hydrogen peroxide for one hour up to several days can be performed when the sample contains dark pigmented tissue (e.g., black skin and fish eyes) [10]. This step can also be applied after decalcification [11].

 (v) Decalcification: when the specimen contains calcified or mineralized tissue, such as cartilage or bone, decalcification is in order. A 10% demineralized water solution of dihydrate ethylenediaminetetraacetic acid (EDTA) slowly diffuses calcium atoms from the sample through a chelation process. Low-power microwave exposure (without heating) drastically accelerates the decalcification process from a month to several days [12, 13].

 (vi) Dehydration: immersion in a graded ethanol series (f.i., 25%, 50%, 75%, 100%, and 100% each for 24 h) removes all water content from the sample [12]. In the final 100% step, optional addition of anhydrous copper sulfate at the bottom of the ethanol bath might improve the dehydration [14].

 (vii) Hexane or benzene: the optional immersion in a graded series of hexane or benzene is said to improve dehydration further [8, 11, 14, 15]. Furthermore, hexane might assist in clearing myelin present in the tissue sample. Nerve axons are surrounded by myelin sheets which do not easily become transparent with Spalteholz fluid.

(viii) Clearing: to achieve large volume imaging in inherently less transparent samples, clearing is needed. The specimens are to be immersed in clearing solution, either through a graded series (f.i., 25%, 50%, 75%, 100%, and 100% each for 24 h) when the hexane or benzene step was skipped [12], or directly in 100% pure clearing solution when hexane or benzene was applied [8, 11]. The clearing solution mimics the refraction index of protein and matches the refraction index of the sample to the solution. The solution can either consist of pure benzyl benzoate followed in a later stage by the final mixture [14], or directly of this mixture solution. A 5 : 3 mixture of methyl salicylate and benzyl benzoate is called Spalteholz fluid [1, 2, 7]. For brain tissue, a 1 : 2 mixture of benzyl alcohol and benzyl benzoate has been found to give better results [8, 11].

(ix) Staining: the required fluorescence can originate from auto-fluorescence from lipofuscins, elastin, and/or collagen [8]. Fluorescent staining can be applied by immersion in a dye bath (of f.i., Rhodamine B isothiocyanate in clearing solution [1]) or even by functional staining. However, many fluorescent dyes deteriorate or even break down completely because of the aggressive clearing solution used, for example, GFP.

2.2. Optical Setup. In what follows, the original OPFOS setup is discussed as it was introduced by Voie et al. in 1993 [1]. Many improved versions have been developed since, all based on the OPFOS or ultramicroscopy design (cf., the discussion).

The setup is represented in Figures 1 and 2. The prepared sample is illuminated by an XY-sheet of laser light travelling along the X-axis. The omnidirectional fluorescence light emitted in the positive Z-axis is used for imaging. Virtual section images in the XY-plane are hence recorded; by translation of the specimen along the Z-axis, an aligned sequence of section images is obtained.

An essential requirement for OPFOS is the generation of a laser light sheet. In practice, it is impossible to generate a perfect plane or sheet of light; however, using a cylindrical lens a sheet can be approximated. A Gaussian laser beam is first expanded and collimated by a Keplerian beam expander. The broadened beam then travels along the X-axis through a cylindrical lens which focusing light in only one dimension to a line along the Z-axis. Along the Y-axis, the Gaussian beam is unaltered, cf. Figure 1. In the XZ-plane, the light sheet has a hyperbolic profile in the focal zone, cf. Figure 3. The Z-thickness of the profile increases in either way along the X-axis when moving away from the minimal beam waist focus d_1. The Rayleigh range x_R is the distance on either site of the minimal focus d_1 where the hyperbolically focused beam has thickened to $\sqrt{2}d_1$. This variable is described by the expression $b_1 = 2x_R = \pi d_1^2/2\lambda$, where b_1 is called the confocal parameter or the total distance in which a focus smaller than $\sqrt{2}d_1$ is maintained. The numerical aperture of the cylindrical lens is inversely related to the confocal parameter b_1 and directly proportional to the beam waist focal thickness d_1.

The height of the beam in Y-direction combined with the confocal parameter b_1 along the X-axis defines the size of the XY-sheet which sections the sample. The specimen consequently has to fit within this zone. A trade-off exists between maximal image and sample width ($\approx b_1$) and the sectioning thickness $\sqrt{2}d_1$ ($\sim 1/\sqrt{b_1}$).

In summary, an OPFOS image has a slicing thickness d_1 in the center, growing to $\sqrt{2}d_1$ at the edges x_R. Everything within the thickness of the laser light sheet is integrated into a flat section image, so actually a varying thickness and slicing resolution is integrated in the 2D image. The wavelength of the laser light depends on the fluorophore that is to be exited. A green laser (532 nm) is suited to excite Rhodamine B, while the blue laser (488 nm) is suited to evoke autofluorescence in many biomedical tissue samples.

3. Results and Discussion

3.1. Application Examples

3.1.1. Biomechanics of Hearing. As a first illustration of the above described OPFOS setup, we show an application in hearing research of the middle ear [16]. Better understanding of the biomechanics of hearing through finite-element modeling requires accurate morphology of the hearing bones and their suspensory soft tissue structures. In Figures 4 and 5, OPFOS cross-sections in gerbil (*Meriones unguiculatus)* middle ears are shown, which can be segmented and triangulated into 3D surface mesh models, cf. Figure 6. Thanks to the OPFOS technique, the sections through the sample can be visualized in real time and clearly show histological detail on both bone and soft tissue.

3.1.2. Morphology of the Brain. In neurology, morphological brain atlases are a useful tool. To this end, sectional imaging with histological detail of mice (C57 black *Mus musculus*) brain was achieved with the OPFOS method, cf. Figure 7. The brain was cleared using the Spalteholz method, though for better results a combination of benzyl alcohol and benzyl benzoate could be used (cf. the section on specimen preparation). An extra hexane immersion step might further improve clearing of the brain.

3.1.3. Biomechanics of Small Vertebrates. In morphological studies, functionality of a musculoskeletal system requires the visualization of both skeleton and muscles. For example, the authors gained insight into the feeding mechanisms of newly born seahorses (*Hippocampus reidi*) by investigating the shape, volume, and orientation of the sternohyoideus muscle with OPFOS (Figure 8). This conspicuous muscle spans from the shoulder girdle to the hyoid bar, assisting in an extremely rapid feeding strike in order to suck in prey [17].

Organogenesis and evolutionary morphology can benefit from OPFOS as well. The technique allows to discern the main structural elements of the head of an African clawed tadpole (*Xenopus laevis*) without any dissection. We could visualize many different tissue types, such as muscle, skeletal, and nervous tissues, and discriminate between them by their distinct (auto)fluorescence gray scales, cf. Figure 9. Skeletal structures were depicted as the darkest mass, corresponding to the lowest autofluorescence. By contrast, the nervous system (brain) was the brightest part, and to a lesser extent also the muscles showed high fluorescence. A 3D reconstruction based on the gray scales in the OPFOS image stacks illustrates this in Figures 9 and 10.

3.2. LSFM Drawbacks. The elaborate specimen preparation required in OPFOS and other LSFM techniques is a major disadvantage. The method is considered nondestructive; however, dehydration removed all water content and decalcification did the same with calcium. It is clear that shrinkage is thus unavoidable and in the same order of magnitude as serial histological sectioning [16, 18, 19].
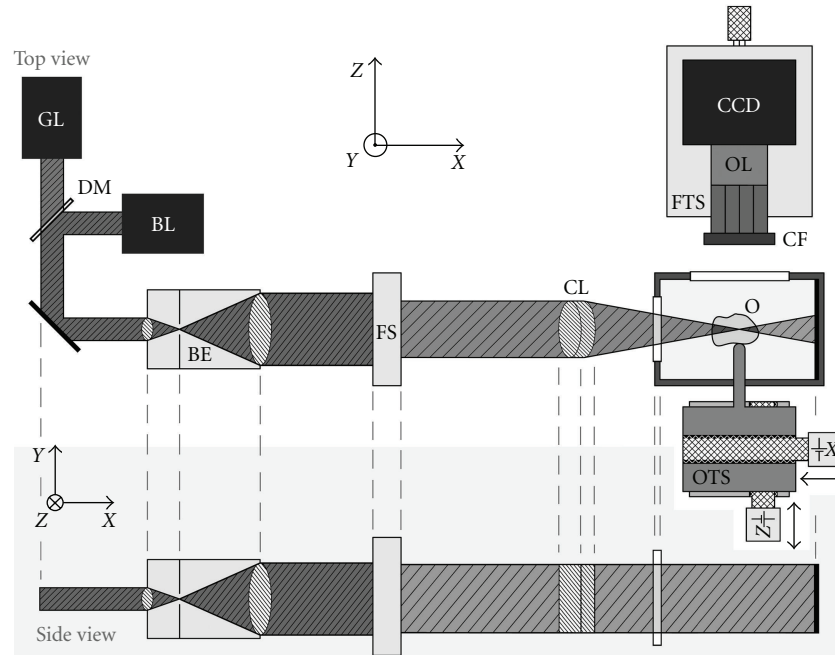
FIGURE 1: Schematic drawing of the (HR-)OPFOS setup: light from a green (GL) or blue laser (BL) passes through a Keplerian beam expander (BE) with spatial filter, a field stop (FS), and a cylindrical achromat lens (CL) which focuses the laser along one dimension within the transparent and fluorescent object (O). A two-axis motorized object translation stage (OTS) allows scanning of the specimen and imaging of different depths. The fluorescence light emitted by the object is projected onto a CCD camera by a microscope objective lens (OL) with fluorescence color filter (CF) in front. The focusing translation stage (FTS) is used to make the objective lens focal plane coincide with the laser focus.
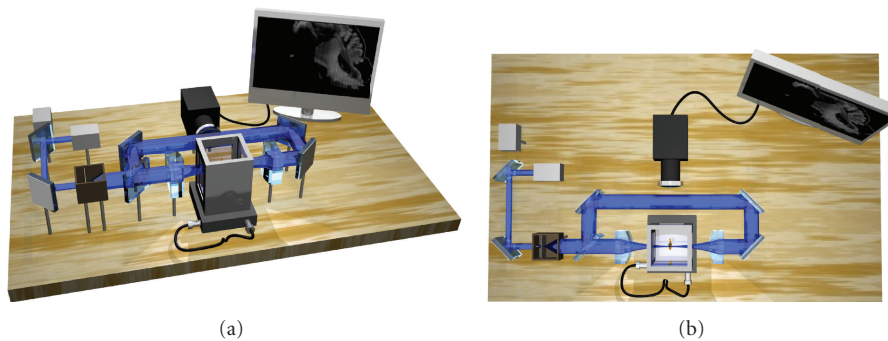

FIGURE 2: A 3D setup representation of an (HR-)OPFOS setup with two-sided cylindrical lens sheet illumination and with two laser wavelengths (green and blue). The blue laser is active here.

The accuracy of measurements based on OPFOS sections depends greatly on the quality of the transparency of the sample and thus on the bleaching, dehydration, and decalcification process. Dark or dense regions in the sample, remaining water content or calcium atoms, refract or scatter laser light, leading to out-of-focus illumination and blurring. Furthermore, the illuminating light sheet entering the sample from one side can be partially absorbed in dense regions resulting in loss of excitation light and fluorescence on the far side of the region. Remaining pigment or zones of less(er) transparency also create this kind of shadows. These stripes or shadow line artifacts are a typical drawback of OPFOS-like techniques. Solutions for these stripes have been implemented, cf. the following section.

Finally, it is important to keep the distance and the amount of refractive material constant between the laser light sectioning plane and the observation lens when sectioning different depths. By translating the refraction-index-matched sample within the Spalteholz-filled specimen chamber orthogonally to the light sheet [5, 7], or by rotating it within the chamber [1, 12], this condition is fulfilled. However, when the entire specimen holder is moved to scan an image stack, the focus will degrade as the focal plane and sectioning plane no longer match [8].
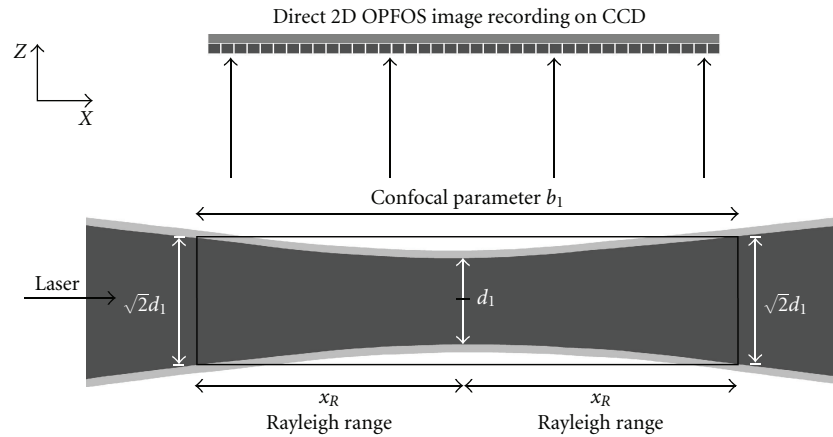
FIGURE 3: The hyperbolic focus profile of a cylindrical lens is shown. OPFOS records 2D images in an approximated planar sheet defined by the confocal parameter zone b_1 where the thickness is considered constant at $\sqrt{2}d_1$. The dark gray area in the center represents the $1/e^2$ intensity profile.
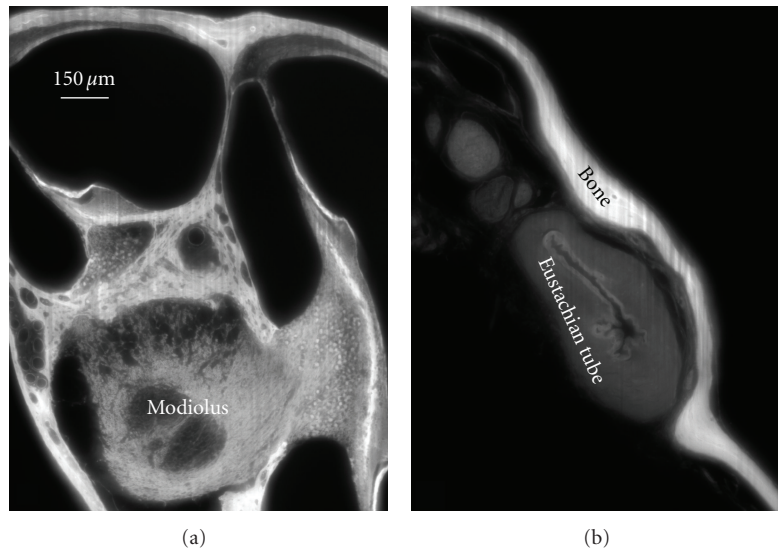

(a)   (b)

FIGURE 4: An OPFOS cross-section of 1600×1200 pixels through (a) the scalae and modiolus of a gerbil inner ear cochlea and (b) a closed Eustachian tube in the middle ear. Rhodamine staining was combined with 532 nm laser light sheet sectioning.

3.3. The OPFOS Family. Optical sectioning with a plane of light was initiated in 1903 by Siedentopf and Zsigmondy [3]. Their Ultramicroscopy light sheet idea was revived 90 years later by Voie et al. with the OPFOS microscope [1, 12, 20]. This invention initiated the LSFM field, but awareness and growth of the field only followed after the 2004 publication of the Single or Selective Plane Illumination Microscope (SPIM) in *Science* by Huisken et al. [5]. Before in 2002, Fuchs et al. also built an LSFM device but not for tissue sectioning microscopy [21]. their thin laser light sheet microscope (TLSM) was used for identification of aquatic microbes in oceanic seawater (rather in the manner of Zsigmondy's Ultramicroscope for colloidal gold particles [22]). The SPIM implementation was developed at Stelzer's EMBL lab in Heidelberg (Germany) and quickly led to many new and improved designs. The SPIM authors claim

to have invented light sheet illumination and orthogonal observation independently from ultramicroscopy and OPFOS—though being aware of and citing OPFOS in 1995 [23]—based on their work on oblique confocal (theta) microscopy [24]. SPIM omits the Spalteholz clearing method which allows to use living animal embryos that possess a natural degree of transparency, like Medaka (*Oryzias latipes*) and fruit fly (*Drosophila melanogaster*) embryos embedded in agarose. Sometimes, multiple SPIM image stacks are recorded between which the sample was rotated, and postprocessing combines them into one high-quality multiview reconstruction.

In 2007, Dodt et al. published a new LSFM setup in *Nature Methods*, again called ultramicroscopy in honor of Zsigmondy, countering the inherent problem of stripe artifacts. The authors added optical components to illuminate
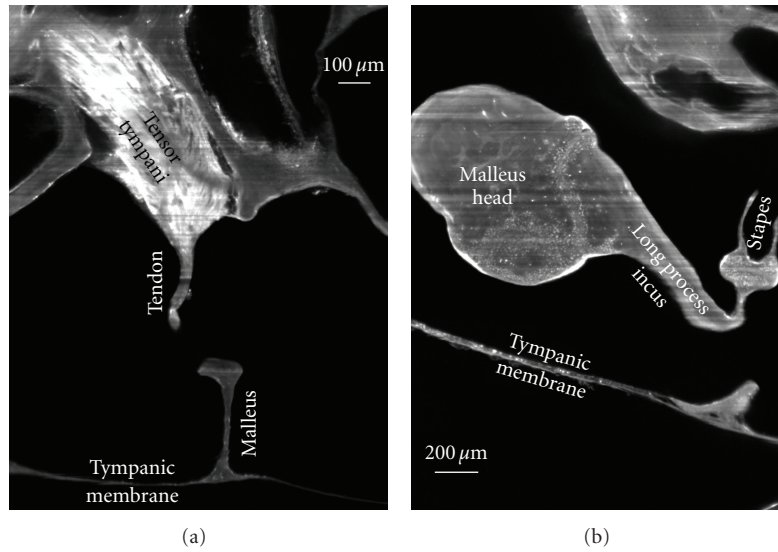
FIGURE 5: 2D virtual cross-sections (1600 × 1200 pixels) from OPFOS microscopy on the gerbil middle ear. (a) Tensor tympani muscle and tendon reaching down towards the malleus hearing bone. (b) Incudomalleolar and incudostapedial articulation between incus and malleus hearing bone. Rhodamine staining was combined with 532 nm laser light sheet sectioning. Pixel size $1.5 \times 1.5 \, \mu$m.
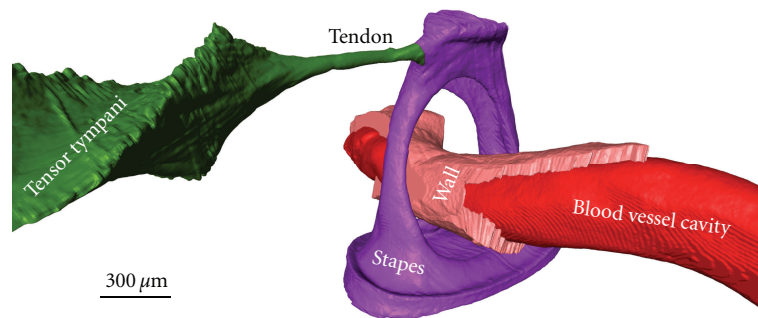
FIGURE 6: A 3D OPFOS reconstruction of Gerbil showing a surface mesh of the stapes hearing bone, a blood vessel running through it, and the tensor tympani muscle attaching to the stapes head. The blood vessel wall and inner cavity are both separately modeled. Voxel size $1.5 \times 1.5 \times 5 \, \mu$m.
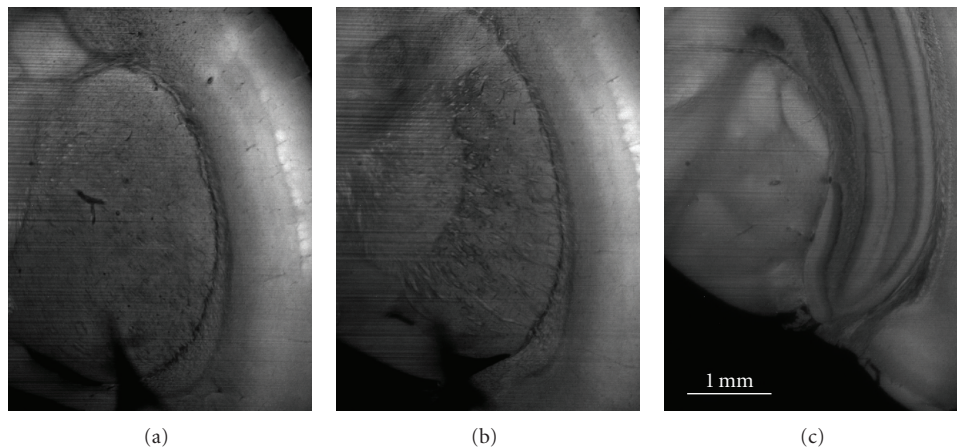
FIGURE 7: Three OPFOS cross sections of 1600 × 1200 pixels at different depths in a mouse brain. Natural autofluorescence of the brain was achieved using 488 nm laser light sheet sectioning. Pixel size $3 \times 3 \, \mu$m.

(a)

(b)

(c)

(d)
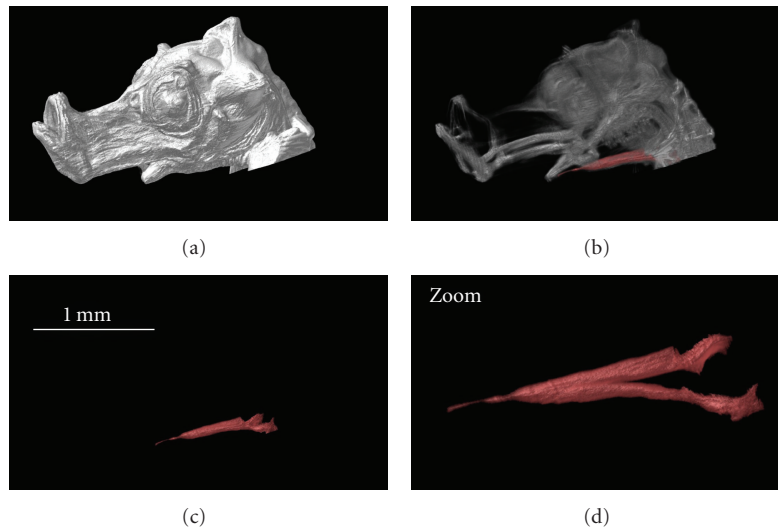
FIGURE 8: 3D reconstruction of the head of a one-day-old seahorse. The OPFOS image data is functionally segmented to study the morphology of the sternohyoideus muscle, cf. zoom (oblique view of the muscle). Natural autofluorescence of the head was achieved using 488 nm laser light sheet sectioning. Voxel size $3.5 \times 3.5 \times 5\,\mu$m.

(a)

(b)

FIGURE 9: (a) A transverse OPFOS cross section through a tadpole head with indications of the different tissue types. (b) A 3D reconstruction of the entire functionally segmented OPFOS image data stack (sensory organs, muscles, cartilage and neuronal structures in different colors) (frontal view). Voxel size $1.5 \times 1.5 \times 3\,\mu$m.

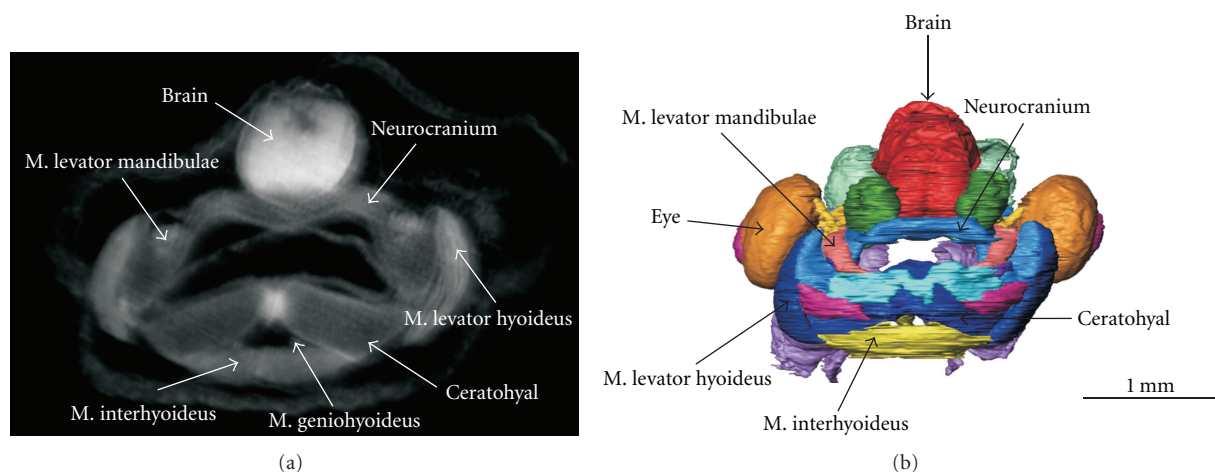the sample simultaneously from opposing sides, effectively reducing the presence of stripes in the images. The Dodt group focuses on visualizing brain tissue. The same year, Huisken and Stainier also started implementing bidirectional sheet illumination (and two constantly pivoting cylindrical lenses) to reduce these stripes, but his multidirectional SPIM or mSPIM setup measures each light sheet consecutively [6]. The resulting two image datasets are computationally combined yielding an image with minimal stripes. Another innovation in mSPIM is related to the quality of light sheet illumination. Each mSPIM cylindrical lens focuses laser light to a horizontal line into the back focal plane of microscope objective lens. Hence, the quality and aberrations of the light sheet is determined by the well-corrected objective and not by the cylindrical lens.

Whenever using cylindrical lenses for light sheet generation, the resulting parabolic focus can only be approximated as a plane over a length described by the confocal parameter, cf. the section on OPFOS setup. The minimal beam waist thickness of the parabolic focus widens near the edges of the confocal parameter with a factor $\sqrt{2}$. Consequently, the light plane has no constant thickness and thus no constant sectioning resolution. Furthermore, a trade-off exists between the length of the confocal parameter and the thickness of the plane. Large(r) macroscopic samples require a large confocal parameter and consequently a thick sectioning plane and low sectioning resolution. Buytaert and Dirckx resolved this problem in 2007 by line scanning the sample across the minimal beam waist, and stitching the section image columns together [7]. In this way, the confocal parameter is
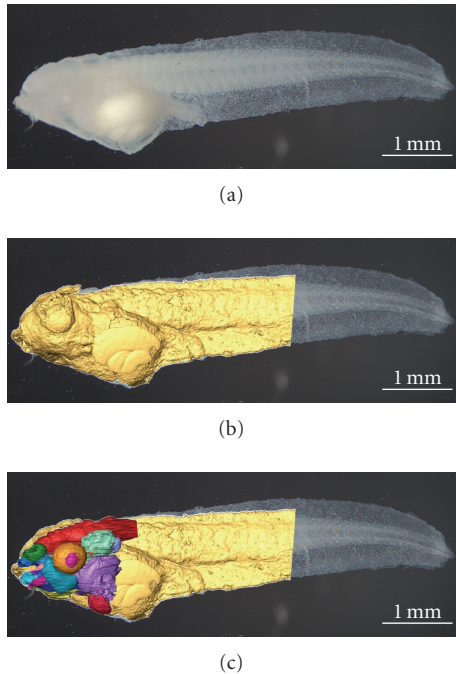
(a)

(b)

(c)

FIGURE 10: (a) A photograph of the tadpole after bleaching. (b) The photograph is superposed with the OPFOS surface mesh of the tadpole head and body. (c) Color-coded functional segmentation of individual organs, cf. Figure 9.

allowed to be small, producing a thin sectioning plane and high sectioning resolution. Their implementation was called high-resolution OPFOS or HR-OPFOS. The newest version of HR-OPFOS incorporates bidirectional sheet illumination as in ultramicroscopy, cf. Figure 2 [4].

In 2008, three new LSFM versions were developed. Holekamp et al. fixed the light sheet illumination unit to the observation objective [25]. This implementation was referred to as objective-coupled planar illumination (OCPI) used for living brain imaging. Dunsby used a one high numeric aperture lens in his oblique plane microscope (OPM) to both illuminate the sample with an oblique light sheet and observe the fluorescence [26]. Finally, Keller et al. introduced a new method to generate a light sheet. A tilting mirror rapidly scans a micrometer thin *spherical* focus of laser light into a plane [27]. The method is called digital scanned laser light sheet fluorescence microscopy (DSLM).

Thin-sheet laser imaging microscopy (TSLIM) by Santi et al. incorporates many improved features of the previous devices [28], namely, the bidirectional light-sheet illumination from ultramicroscopy, the image stitching idea from HR-OPFOS, and the combination of cylindrical lenses with aberration corrected objectives from mSPIM.

Finally, Mertz and Kim developed the HiLo LSFM system [29]. This DSLM-based device counters sample-induced scattering and aberrations that broaden the thickness of the sheet illumination. Through sequential uniform and structured sheet illumination, out-of-focus background can be identified and rejected in postprocessing, improving the image quality.

3.4. Commercial Devices. The long-lasting lack of a commercial LSFM device is responsible for the many different implementations of the basic method and for the unfamiliarity of researchers with the technique in certain fields [11]. This is all about to change since now LSFM microscopes have become commercially available.

Carl Zeiss showed a prototype of a commercial LSFM device, named SPIM, at the First LSFM meeting in 2009 in Dresden (Germany). *Zeiss* is still preparing the launch of their system, but *LaVision BioTec* already launched the ultramicroscope (in collaboration with Dodt) near the end of 2009 at Neuroscience in Chicago (US). The samples are limited to less than one cubic centimeter and require clearing. The device is optimized to image juvenile mouse brains and complete mouse and fruit fly embryos. *LaVision* acknowledges the initial Ultramicroscopy idea by Zsigmondy, and OPFOS by Voie as being the first tissue microscopy implementation.

4. Conclusions

We have shown with several applications that the OPFOS (and derived) methods, better known as light-sheet-based fluorescence microscopy or LSFM, are a valuable addition for sectional imaging and three-dimensional modeling of anatomic structures. LSFM has the major advantage that the virtual slices are automatically and perfectly aligned, making it easy to generate 3D models from them. Microscopy techniques are either focusing on flexibility, imaging depth, speed, or resolution. LSFM has all these benefits according to device manufacturers and the LSFM scientific community. Specimens containing both bone and soft tissue and ranging from microscopic till small macroscopic in size can be studied with LSFM, with application in biomedical and life sciences. This microscopy method is relatively new, conceptually simple but powerful. Researchers can easily build their own setup, and even the first commercial devices are becoming available.

Acknowledgments

References

[1] A. H. Voie, D. H. Burns, and F. A. Spelman, "Orthogonal-plane fluorescence optical sectioning: three-dimensional imaging of macroscopic biological specimens," *Journal of Microscopy*, vol. 170, no. 3, pp. 229–236, 1993.

[2] W. Spalteholz, *Über das Durchsichtigmachen von Menschlichen und Tierischen Präparaten*, Verlag Hirzel, 1911.

[3] H. Siedentopf and R. A. Zsigmondy, "Uber sichtbarmachung und größenbestimmung ultramikoskopischer teilchen, mit besonderer anwendung auf goldrubingläser," *Annalen der Physik*, vol. 315, pp. 1–39, 1903.

[4] J. A. N. Buytaert and J. J. J. Dirckx, "Tomographic imaging of macroscopic biomedical objects in high resolution and three dimensions using orthogonal-plane fluorescence optical sectioning," *Applied Optics*, vol. 48, no. 5, pp. 941–948, 2009.

[5] J. Huisken, J. Swoger, F. Del Bene, J. Wittbrodt, and E. H. K. Stelzer, "Optical sectioning deep inside live embryos by selective plane illumination microscopy," *Science*, vol. 305, no. 5686, pp. 1007–1009, 2004.

[6] J. Huisken and D. Y. R. Stainier, "Even fluorescence excitation by multidirectional selective plane illumination microscopy (mSPIM)," *Optics Letters*, vol. 32, no. 17, pp. 2608–2610, 2007.

[7] J. A. N. Buytaert and J. J. J. Dirckx, "Design and quantitative resolution measurements of an optical virtual sectioning three-dimensional imaging technique for biomedical specimens, featuring two-micrometer slicing resolution," *Journal of Biomedical Optics*, vol. 12, no. 1, Article ID 014039, 2007.

[8] H. U. Dodt, U. Leischner, A. Schierloh et al., "Ultramicroscopy: three-dimensional visualization of neuronal networks in the whole mouse brain," *Nature Methods*, vol. 4, no. 4, pp. 331–336, 2007.

[9] R. Hofman, J. M. Segenhout, J. A. N. Buytaert, J. J. J. Dirckx, and H. P. Wit, "Morphology and function of Bast's valve: additional insight in its functioning using 3D-reconstruction," *European Archives of Oto-Rhino-Laryngology*, vol. 265, no. 2, pp. 153–157, 2008.

[10] J. Buytaert, E. Descamps, D. Adriaens, and J. Dirckx, "Orthogonal-plane fluorescence optical sectioning : a technique for 3-D imaging of biomedical specimens," in *Microscopy: Science, Technology, Applications and Education*, A. Méndez-Vilas and J. Díaz, Eds., pp. 1356–1365, Formatex, 2010.

[11] P. A. Santi, "Light sheet fluorescence microscopy: a review," *The Journal of Histochemistry and Cytochemistry*, vol. 59, no. 2, pp. 129–138, 2011.

[12] A. H. Voie, "Imaging the intact guinea pig tympanic bulla by orthogonal-plane fluorescence optical sectioning microscopy," *Hearing Research*, vol. 171, no. 1-2, pp. 119–128, 2002.

[13] S. P. Tinling, R. T. Giberson, and R. S. Kullar, "Microwave exposure increases bone demineralization rate independent of temperature," *Journal of Microscopy*, vol. 215, no. 3, pp. 230–235, 2004.

[14] C. F. A. Culling, "Spalteholz technique," in *Handbook of Histopathological and Histochemical Techniques*, pp. 550–552, Butterworths, 1974.

[15] V. Ermolayev, M. Friedrich, R. Nozadze et al., "Ultramicroscopy reveals axonal transport impairments in cortical motor neurons at prion disease," *Biophysical Journal*, vol. 96, no. 8, pp. 3390–3398, 2009.

[16] J. A. N. Buytaert, W. H. M. Salih, M. Dierick, P. Jacobs, and J. J. J. Dirckx, "Realistic 3-D computer model of the gerbil middle ear, featuring accurate morphology of bone and soft tissue structures," *Journal of the Association for Research in Otolaryngology*. In press.

[17] S. Van Wassenbergh, G. Roos, A. Genbrugge et al., "Suction is kid's play: extremely fast suction in newborn seahorses," *Biology Letters*, vol. 5, no. 2, pp. 200–203, 2009.

[18] R. Hofman, J. M. Segenhout, and H. P. Wit, "Three-dimensional reconstruction of the guinea pig inner ear, comparison of OPFOS and light microscopy, applications of 3D reconstruction," *Journal of Microscopy*, vol. 233, no. 2, pp. 251–257, 2009.

[19] J. Lane and Z. A. Ralis, "Changes in dimensions of large cancellous bone specimens during histological preparation as measured on slabs from human femoral heads," *Calcified Tissue International*, vol. 35, no. 1, pp. 1–4, 1983.

[20] A. H. Voie and F. A. Spelman, "Three-dimensional reconstruction of the cochlea from two-dimensional images of optical sections," *Computerized Medical Imaging and Graphics*, vol. 19, no. 5, pp. 377–384, 1995.

[21] E. Fuchs, J. S. Jaffe, R. A. Long, and F. Azam, "Thin laser light sheet microscope for microbial oceanography," *Optics Express*, vol. 10, no. 2, pp. 145–154, 2002.

[22] R. A. Zsigmondy, *Properties of Colloids*, Nobel lecture in chemistry, Elsevier, Amsterdam, The Netherlands, 1926.

[23] E. H. K. Stelzer, S. Lindek, S. Albrecht et al., "A new tool for the observation of embryos and other large specimens: confocal theta fluorescence microscopy," *Journal of Microscopy*, vol. 179, no. 1, pp. 1–10, 1995.

[24] S. Lindek and E. H. K. Stelzer, "Confocal theta microscopy and 4Pi-confocal theta microscopy," in *Three-Dimensional Microscopy, SPIE International Society for Optical Engineering*, vol. 2184 of *Proceedings of the SPIE*, p. 188, 1994.

[25] T. F. Holekamp, D. Turaga, and T. E. Holy, "Fast three-dimensional fluorescence imaging of activity in neural populations by objective-coupled planar illumination microscopy," *Neuron*, vol. 57, no. 5, pp. 661–672, 2008.

[26] C. Dunsby, "Optically sectioned imaging by oblique plane microscopy," *Optics Express*, vol. 16, no. 25, pp. 20306–20316, 2008.

[27] P. J. Keller, A. D. Schmidt, J. Wittbrodt, and E. H. K. Stelzer, "Reconstruction of zebrafish early embryonic development by scanned light sheet microscopy," *Science*, vol. 322, no. 5904, pp. 1065–1069, 2008.

[28] P. A. Santi, S. B. Johnson, M. Hillenbrand, P. Z. GrandPre, T. J. Glass, and J. R. Leger, "Thin-sheet laser imaging microscopy for optical sectioning of thick tissues," *BioTechniques*, vol. 46, no. 4, pp. 287–294, 2009.

[29] J. Mertz and J. Kim, "Scanning light-sheet microscopy in the whole mouse brain with HiLo background rejection," *Journal of Biomedical Optics*, vol. 15, no. 1, p. 016027, 2010.

Research Article

Computed Tomography and Magnetic Resonance Imaging Features of the Temporomandibular Joint in Two Normal Camels

Alberto Arencibia, Diego Blanco, Nelson González, and Miguel A. Rivero

Department of Morphology, Veterinary Faculty, University of Las Palmas de Gran Canaria, Trasmontaña s/n, Gran Canaria, 35413 Las Palmas, Spain

Correspondence should be addressed to Alberto Arencibia, aarencibia@dmor.ulpgc.es

Computed tomography (CT) and magnetic resonance (MR) image features of the temporomandibular joint (TMJ) and associated structures in two mature dromedary camels were obtained with a third-generation equipment CT and a superconducting magnet RM at 1.5 Tesla. Images were acquired in sagittal and transverse planes. Medical imaging processing with imaging software was applied to obtain postprocessing CT and MR images. Relevant anatomic structures were identified and labelled. The resulting images provided excellent anatomic detail of the TMJ and associated structures. Annotated CT and MR images from this study are intended as an anatomical reference useful in the interpretation for clinical CT and MR imaging studies of the TMJ of the dromedary camels.

1. Introduction

The temporomandibular joint (TMJ) is a synovial condylar joint between the base of the zygomatic process of the temporal bone and the condylar process of the mandible; its main articular components are the synovial pouches, articular disc, caudal and lateral ligaments, and joint capsule [1].

In veterinary medicine, the exploration of the anatomical structures located in the TMJ and the evaluation of the soft tissues turn out to be laborious due to its complex anatomical organization [2–5], which makes it difficult to diagnose morphological alterations by means of physical exploration and conventional radiographic studies [6–8].

Nowadays, modern image-based diagnostic techniques, especially computed tomography (CT) [9–14], and magnetic resonance imaging (MRI) [15–21], make possible to obtain body sections from different tomographic planes, achieving images with a good anatomical resolution, high contrast between different structures, and excellent tissue-like differentiation. The applications of CT and MRI have revolutionized the practice of veterinary diagnostic imaging. In large animals, several studies have demonstrated the clinical value of CT and MRI of the TMJ [22–25]. To the author's knowledge, there is no published material describing the results of CT and MRI of the mature camel TMJ. An accurate interpretation of the CT and MRI normal anatomy is necessary for the evaluation of pathological tissues.

The objective of this study was to provide an overview of the normal anatomy of the TMJ of the dromedary camel using CT, MR images, and transverse gross anatomical section.

2. Methods

2.1. Animals. Two male mature dromedary camels' cadaver heads were used for this study. One was from a 4-year-old (525 kg bodyweight) and the other from an 8-year-old (638 kg bodyweight) one. Camels were dead for medical reasons unrelated to the TMJ diseases and did not show lesions in the head that could influence our results.

The camels belonged to a Camel Farm located in Fataga, Gran Canaria, Canary Island, Spain. Both heads, sectioned at the level of atlantoaxial joint, were refrigerated and imaged immediately to minimize postmortem changes.

(a)   (b)
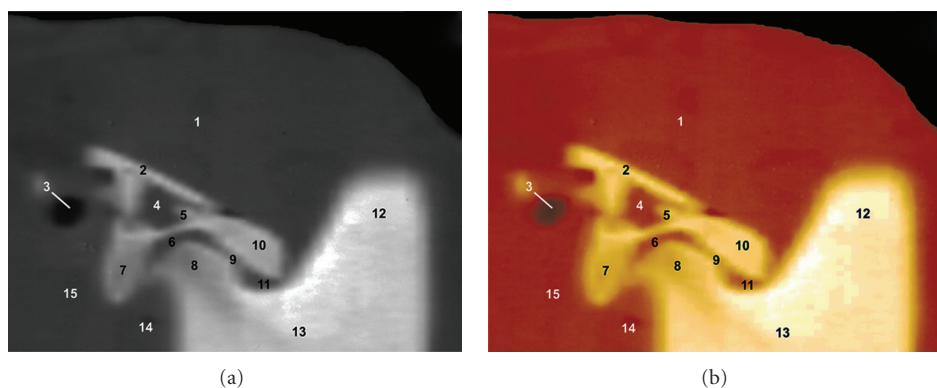
FIGURE 1: Sagittal CT images at the level of the TMJ in a mature camel. (a) Soft tissue window CT image (WW = 4000; WL = 335) and (b) postprocessing VR muscles-bones CT image (Osirix imaging software). Right lateral view. 1 is temporal muscle; 2 is border of the temporal fossa; 3 is external acoustic meatus; 4 is temporal venous sinus; 5 is zygomatic process of the temporal bone; 6 is articular disc; 7 is retroarticular process; 8 is mandibular condyle; 9 is joint capsule; 10 is articular tubercle; 11 is mandibular notch; 12 is coronoid process of mandible; 13 is ramus of mandible; 14 is digastric muscle; 15 is parotid salivary gland.

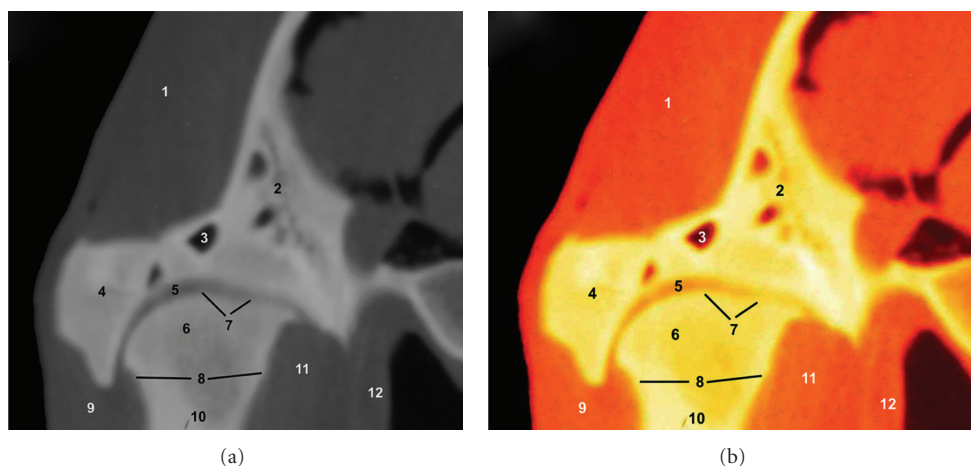(a)   (b)

FIGURE 2: Transverse CT images at the level of the TMJ in a mature camel. (a) Soft tissue window CT image (WW = 4000; WL = 335) and (b) postprocessing VR muscles-bones CT image (Osirix imaging software). Caudal view. 1 is temporal muscle; 2 is squamous part of the temporal bone; 3 is temporal venous sinus; 4 is zygomatic process of the temporal bone; 5 is articular disc; 6 is mandibular condyle; 7 is joint capsule; 8 is cortical bone; 9 is masseter muscle; 10 is ramus of mandible; 11 is lateral pterygoid muscle; 12 is tensor and levator veli palatini muscles.

2.2. CT Scan Technique. CT imaging was performed at the Radiodiagnostic Service of the Hospital Universitario Insular of Las Palmas de Gran Canaria (Spain), with a Toshiba 600 HQ scanner (third-generation equipment, Toshiba Medical Imaging System, Tustin, Calif, USA). Throughout the procedure, the heads were positioned in ventral recumbency during scanning time.

CT images from the TMJ were obtained in sagittal and transverse planes with 120 kV and 130 Ma. Best image quality was obtained by adjusting the window widths (WWs) and window levels (WLs) setting.

For visualizing soft tissue structures, a soft-tissue window setting (WW = 4000; WL = 335) was used. In addition, medical imaging processing software (Osirix) was applied to obtain postprocessing sagittal and transverse CT images with clut VR muscles-bones.

2.3. MRI Technique. MR imaging was performed at the Radiodiagnostic Service of the Clinica San Roque of Las Palmas de Gran Canaria (Spain), using a superconducting magnet operating at field strength of 1.5 Tesla (Genesis Sigma; General Electric Medical System, USA) and a human coil. Images were acquired in sagittal and transverse planes with fast spin-echo (FSE) sequences. Throughout the procedure, the heads were positioned in ventral recumbency during scanning time.

FSE T1-weighted transverse MR images were obtained with the following parameters: repetition time (TR) = 340 ms, echo time (TE) = 8 ms, 256 × 224 matrix, and one excitation. For FSE T2-weighted transverse images, the TR was 6400 ms, TE was 105 ms, 256 × 224 matrix, and one excitation. In addition, medical imaging processing software
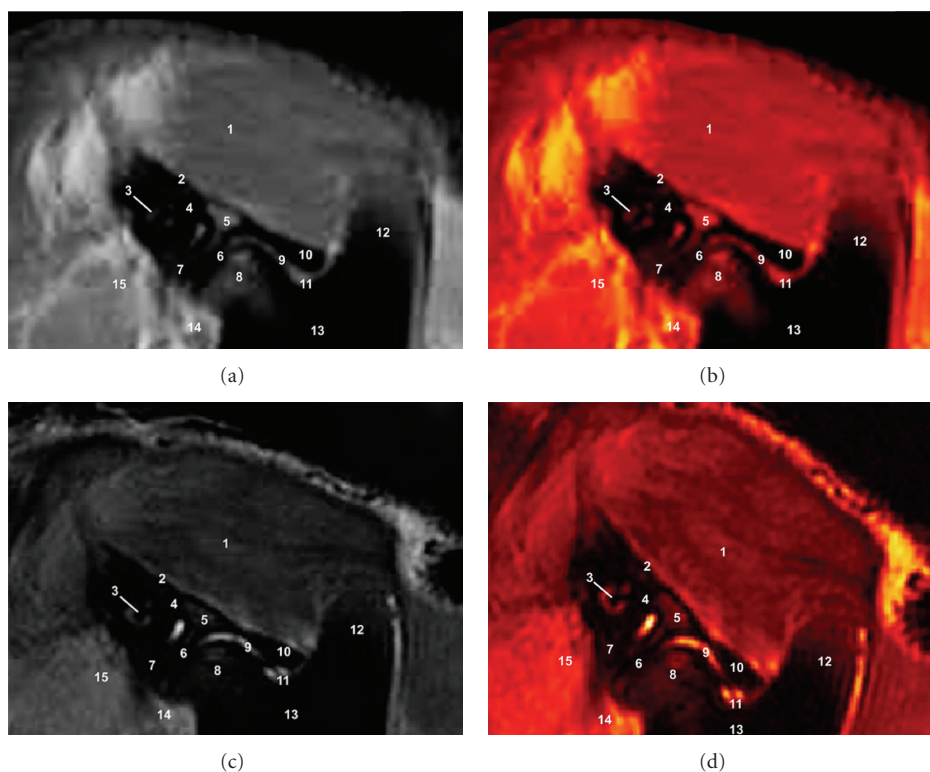
FIGURE 3: Sagittal FSE MR images at the level of the TMJ in a mature camel. (a) T1-weighted MR image, (b) postprocessing VR muscles-bones T1-weighted MR image (Osirix imaging software), (c) T2-weighted MR image, and (d) postprocessing VR muscles-bones T2-weighted MR image (Osirix imaging software). Right lateral view. 1 is temporal muscle; 2 is border of the temporal fossa; 3 is external acoustic meatus; 4 is temporal venous sinus; 5 is zygomatic process of the temporal bone; 6 is articular disc; 7 is retroarticular process; 8 is mandibular condyle; 9 is joint capsule; 10 is articular tubercle; 11 is mandibular notch; 12 is coronoid process of mandible; 13 is ramus of mandible; 14 is digastric muscle; 15 is parotid salivary gland.

(Osirix) was applied to obtain postprocessing T1- and T2-weighted MR images with clut VR muscles-bones.

2.4. Anatomical Evaluation. CT and MR images were compared to transverse anatomical section and with anatomy books [1, 26–28], to identify the normal CT and MRI anatomy of the TMJ of the dromedary camel. Clinically, several structures of the TMJ were identified and labelled according to an internationally accepted veterinary anatomical nomenclature [27].

3. Results

In this study, anatomical structures of the TMJ of the mature camel were identified and labelled in five figures (Figures 1, 2, 3, 4, and 5).

3.1. CT Images (Figures 1 and 2). The use of the soft-tissue window permits to identify the articular surfaces (articular cartilage and subchondral bone), articular disc and joint capsule, and the relationships between the TMJ, external acoustic meatus and masticatory muscles. Each of these soft tissues showed variable shades of grey, and the synovial fluid was the lowest attenuating structure. The

squamous part of the temporal bone and the mandible were easily identifiable because of the high CT density in cortical bone and the intermediate CT density in their medullary cavities. The articular disc and joint capsule produced low to intermediate attenuation. It was not possible to identify the ligaments, blood vessels, and nerves in CT images. The postprocessing of CT images allowed us to appreciate different bone structures and soft tissues of the TMJ, assisting in the interpretation of the CT images.

3.2. MRI (Figures 3 and 4). Anatomical details of the camel TMJ were evaluated according to the characteristics of signal of the different tissues.

On FSE T1-weighting sequences, the TMJ bony components showed high signal intensity with a granular appearance of the trabecular bone and bone marrow owing to fatty infiltration and no signal intensity (black) of the cortical and subchondral bone. The articular fibrocartilage disc and joint capsule produced low-to-intermediate signal intensity. The parotid salivary gland and masticatory muscles were identified. It was not possible to identify the TMJ ligaments, blood vessels, and nerves in CT images.

On FSE T2-weighted MR images, the cortical and subchondral bone showed the same dark signal intensity, and
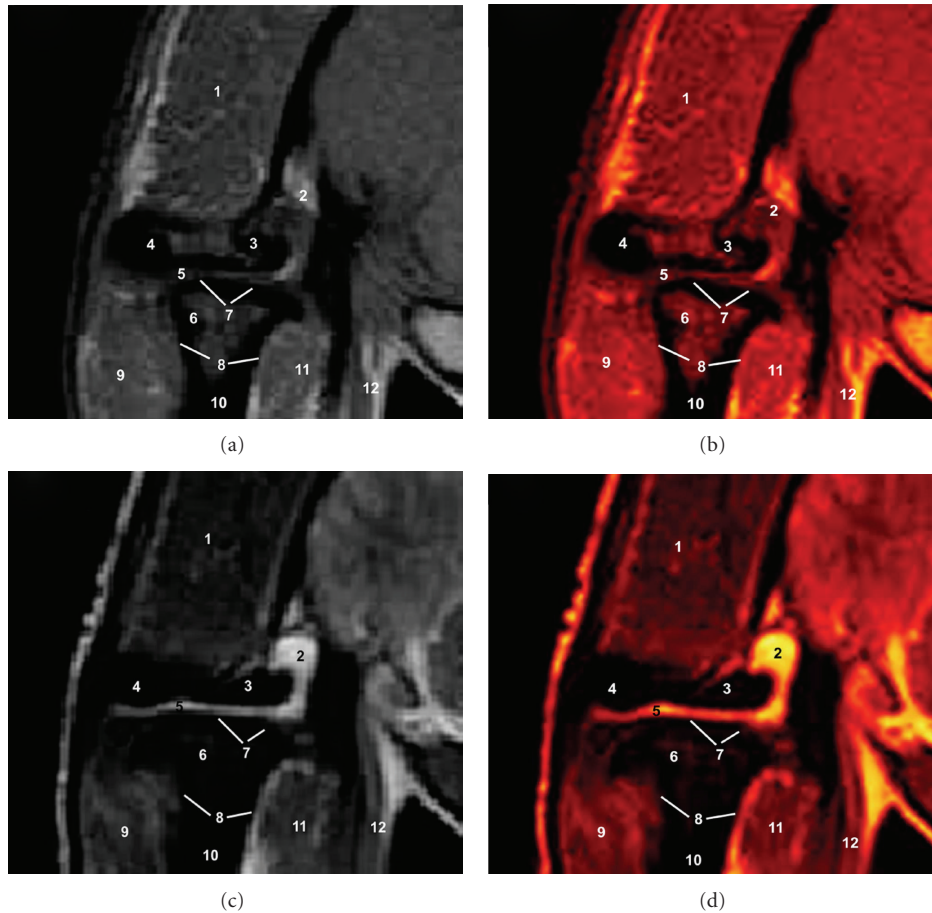
the bone marrow appeared less bright than that on SE T1-weighted images. The articular fibrocartilage disc and joint capsule produced higher signal intensity. The parotid salivary gland and muscles had a intermediate signal intensity and appeared grey. Blood vessels were not differentiated because there was no blood flow as the camels were dead.

The after processing of MR images allowed us to appreciate different bone structures and soft tissues of the TMJ, assisting in the interpretation of the MR images.

3.3. Transverse Anatomical Section of the Left TMJ (Figure 5). The section used in this study provides the comparison with the CT and MR images and allowed the verification of anatomic details.

4. Discussion

To the authors' knowledge, there are no detailed published studies of the TMJ of the dromedary camel using CT and MRI, which turns out to be essential for morphologic,

physiologic, and clinical studies involving bones and soft tissues located in this joint.

CT imaging is a cross-sectional diagnostic technique that provided excellent detail of clinically relevant anatomy and offers considerable advantages compared with traditional radiography and ultrasound for the examination of the TMJ: a lack of superimposition of the tissues and a higher differentiation of tissue densities [24, 25, 29]. CT provides excellent spatial resolution and good discrimination between bone and soft tissue [9–14, 24, 25, 29, 30]. CT is more sensitive in detecting diseases and distinguishes normal and abnormal structures accurately [22–24].

FSE T1- and T2-weighted MR images of the camel TMJ provided details of clinically relevant anatomy, and there were discrimination of both soft and mineralized tissues [15–21, 29]. MRI leads to an excellent spatial resolution and good discrimination between the bones and the cephalic soft tissues, in comparison with other conventional image-based techniques, due to a higher contrast resolution of the anatomic structures. MRI is good for understanding the morphology and the positions of the soft tissues [15–21, 29].
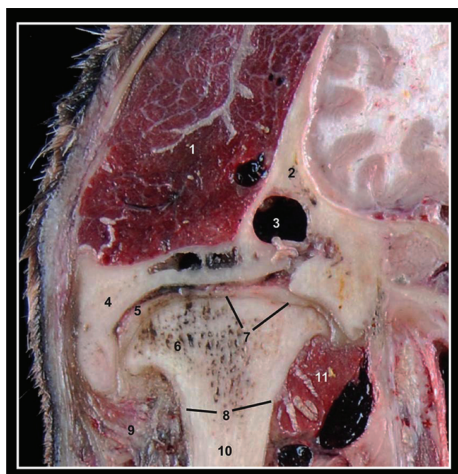
Figure 5: Transverse anatomical section at the level of the left TMJ in a mature camel. Caudal view. 1 is temporal muscle; 2 is squamous part of the temporal bone; 3 is temporal venous sinus; 4 is zygomatic process of the temporal bone; 5 is articular disc; 6 is mandibular condyle; 7 is joint capsule; 8 is cortical bone; 9 is masseter muscle; 10 is ramus of mandible; 11 is lateral pterygoid muscle.

In addition, an important advantage is that MRI is a powerful technique for obtaining images on various anatomic planes without repositioning of the animal. Nonetheless, MRI also shows some disadvantages in comparison to other exploratory procedures. We emphasize that sedation is required if the animal is alive, the high cost of such equipment and the lack of antennas for use in medicine of the camels. This is the reason why many authors have resorted to the low intensity of the MRI units or collaboration agreements with hospitals in human medicine [15–21]. It is also necessary to stress that MRI is an image-based diagnostic technique that does not detect the contents of calcium in organic tissues, and, therefore, its application on studies of the osseous system is not recommended.

In our study, we used an MRI unit of 1.5 T with a superconductor magnet, which enabled us to obtain high-definition tomographies. The physical parameters (TR, TE, matrix, etc.) which we applied to obtain MRI on the sagittal and transverse spatial planes can be used as an initial valid reference for this type of exploratory studies on the TMJ of the camel, especially for scientists who initiate themselves in the application of these modern image-based diagnostic techniques.

MRI obtained in the sagittal plane allowed us a better evaluation of the topographic anatomic structures on the median plane of the TMJ, fundamentally the articular surfaces and articular disc, as well as the associated and topographically related structures. The anatomic relationships were appreciated most easily in the transverse planes. The anatomy section of the TMJ allows a correct morphologic assessment and topographic evaluation of anatomical structures, being useful tool for the identification of CT and MRI images. A thorough understanding of normal TMJ anatomy on CT and MR images is essential to optimize the diagnosis of TMJ disorders [16, 21, 25]. In the same way, we consider it quite useful to be able to establish some references on TMJ, in order to scan only selected parts during a clinical or experimental approach.

The use of CT and MRI in camels is limited because of cost, availability, and logistical problems to acquire imaging in large animals [9–11, 13, 14, 17, 19–25]. With developing technology [30], CT and MR imaging may soon become more readily available for diagnostic imaging in veterinary medicine.

5. Conclusions

Our study contribute to a better anatomical knowledge of the TMJ of the dromedary camel by means of CT and MRI and is a useful initial reference for clinical studies. CT is an excellent method for the detailed assessment of the bony structures. MRI is a valid imaging modality for the evaluation of the soft tissues. The FSE T1-weighted sequence should be the baseline to identify the anatomy, and FSE T2-weighted sequence will better enhance the study of the articular surfaces and articular disc. The after processing of CT and MR images allowed us to appreciate different bone structures and soft tissues of the TMJ, assisting in the interpretation of the images.

Acknowledgments

References

[1] J. Sandoval, *Tratado de Anatomía Veterinaria. Tomo III: Cabeza y Sistemas Viscerales*, Imprenta Sorles, León, Spain, 2000.

[2] T. Schwarz, R. Weller, A. M. Dickie, M. Konar, and M. Sullivan, "Imaging of the canine and feline temporomandibular joint: a review," *Veterinary Radiology and Ultrasound*, vol. 43, no. 2, pp. 85–97, 2002.

[3] S. J. Bonin, H. M. Clayton, J. L. Lanovaz, and T. J. Johnson, "Kinematics of the equine temporomandibular joint," *American Journal of Veterinary Research*, vol. 67, no. 3, pp. 423–928, 2006.

[4] P. H. Ramzan, "The temporomandibular joint: component of clinical complexity," *Equine Veterinary Journal*, vol. 38, no. 2, pp. 102–104, 2006.

[5] M. J. Rodríguez, A. Agut, F. Gil, and R. Latorre, "Anatomy of the equine temporomandibular joint: study by gross dissection, vascular injection and section," *Equine Veterinary Journal*, vol. 38, no. 2, pp. 143–147, 2006.

[6] M. B. Hurtig, S. M. Barber, and C. S. Farrow, "Temporomandibular joint luxation in a horse," *Journal of the American Veterinary Medical Association*, vol. 185, no. 1, pp. 78–80, 1984.

[7] J. Hardy and J. T. Shiroma, "What is your diagnosis? Rostral luxation of the right temporomandibular joint," *Journal of the American Veterinary Medical Association*, vol. 198, no. 9, pp. 1663–1664, 1991.

[8] D. V. Devine, H. D. Moll, and R. J. Bahr, "Fracture, luxation, and chronic septic arthritis of the temporomandibular joint in a juvenile horse," *Journal of Veterinary Dentistry*, vol. 22, no. 2, pp. 96–99, 2005.

[9] D. D. Barbee, J. R. Allen, and P. R. Gavin, "Computed tomography in horses: technique," *Veterinary Radiology*, vol. 28, no. 5, pp. 144–151, 1987.

[10] Y. Lignereux, J. Fargeas, M. H. Marty, and P. Bénard, "Computerized tomographic examination of the stereotaxic topography of the meningeal spaces of the cow (Bos taurus L.)," *Anatomia, Histologia, Embryologia*, vol. 15, no. 4, pp. 289–302, 1986.

[11] J. T. Hatchcock, D. G. Pugh, R. E. Cartee, and L. Hammond, "Computed tomography of the llama head: technique and normal anatomy," *Veterinary Radiology & Ultrasound*, vol. 36, no. 4, pp. 290–296, 1995.

[12] A. Arencibia, J. M. Vázquez, J. A. Ramirez, J. A. Sandoval, G. Ramirez, and C. Sosa, "Anatomy of the cranioencephalic structures of the goat (Capra hircus L.) by imaging techniques: a computerized tomographic study," *Anatomia, Histologia, Embryologia*, vol. 26, no. 3, pp. 161–164, 1997.

[13] A. Arencibia, J. M. Vázquez, M. Rivero et al., "Computed tomography of normal cranioencephalic structures in two horses," *Anatomia, Histologia, Embryologia*, vol. 29, no. 5, pp. 295–299, 2000.

[14] K. L. Morrow, R. D. Park, T. L. Spurgeon, T. S. Stashak, and B. Arceneaux, "Computed tomographic imaging of the equine head," *Veterinary Radiology and Ultrasound*, vol. 41, no. 6, pp. 491–497, 2000.

[15] S. L. Kraft, P. R. Gavin, L. R. Wendling, and V. K. Reddy, "Canine brain anatomy on magnetic resonance images," *Veterinary Radiology*, vol. 30, no. 4, pp. 147–158, 30.

[16] D. M. Macready, S. Hecht, L. E. Craig, and G. A. Conklin, "Magnetic resonance imaging features of the temporomandibular joint in normal dogs," *Veterinary Radiology and Ultrasound*, vol. 51, no. 4, pp. 436–440, 2010.

[17] M. K. Chaffin, M. A. Walker, N. H. Mcarthur, E. E. Perris, and N. S. Matthews, "Magnetic resonance imaging of the brain of normal neonatal foals," *Veterinary Radiology and Ultrasound*, vol. 38, no. 2, pp. 102–111, 1997.

[18] W. R. Widmer, K. A. Buckwalter, M. A. Hill, J. F. Fessler, and S. Ivancevich, "A technique for magnetic resonance imaging of equine cadaver specimens," *Veterinary Radiology and Ultrasound*, vol. 40, no. 1, pp. 10–14, 1999.

[19] A. Arencibia, J. M. Vázquez, R. Jaber et al., "Magnetic resonance imaging and cross sectional anatomy of the normal equine sinuses and nasal passages," *Veterinary Radiology and Ultrasound*, vol. 41, no. 4, pp. 313–319, 2000.

[20] A. Arencibia, M. A. Rivero, F. Gil et al., "Anatomy of the cranioencephalic structures of the camel (Camelus dromedarius L.) by imaging techniques: a magnetic resonance imaging study," *Journal of Veterinary Medicine Series C*, vol. 34, no. 1, pp. 52–55, 2005.

[21] M. J. Rodríguez, A. Agut, M. Soler et al., "Magnetic resonance imaging of the equine temporomandibular joint anatomy," *Equine Veterinary Journal*, vol. 42, no. 3, pp. 200–207, 2010.

[22] C. A. Ragle, P. D. Koblik, J. R. Pascoe, and C. M. Honnas, "Computed tomographic evaluation of head trauma in a foal," *Veterinary Radiology*, vol. 29, no. 5, pp. 206–208, 1988.

[23] S. Tietje, M. Becker, and G. Böckenhoff, "Computed tomographic evaluation of head diseases in the horse: 15 cases," *Equine Veterinary Journal*, vol. 28, no. 2, pp. 98–105, 1996.

[24] E. P. L. Warmerdam, W. R. Klein, and B. P. J. M. Van Herpen, "Infectious temporomandibular joint disease in the horse: computed tomographic diagnosis and treatment of two cases," *Veterinary Record*, vol. 141, no. 7, pp. 172–174, 1997.

[25] M. J. Rodríguez, R. Latorre, O. López-Albors et al., "Computed tomographic anatomy of the temporomandibular joint in the young horse," *Equine Veterinary Journal*, vol. 40, no. 6, pp. 566–571, 2008.

[26] M. M. Smuts and A. J. Bezuidenhout, *Anatomy of the Dromedary*, Clarendon Press, Oxford, UK, 1987.

[27] O. Schaller, *Illustrated Veterinary Anatomical Nomenclature*, Ferdinand Enke, Sttutgart, Germany, 1992.

[28] J. M. Vázquez Autón, F. Gil Cano, F. Moreno Medina, R. Latorre Reviriego, and G. Ramírez Zarzosa, in *Atlas en Color. Anatomía Veterinaria. Volumen I Cabeza*, Universidad de Murcia, Murcia, Spain, 1992.

[29] J. C. Vilanova, J. Barceló, J. Puig, S. Remollo, C. Nicolau, and C. Bru, "Diagnostic imaging: magnetic resonance imaging, computed tomography, and ultrasound," *Seminars in Ultrasound, CT and MRI*, vol. 28, no. 3, pp. 184–191, 2007.

[30] A. Shores, "New and future advanced imaging techniques," *Veterinary Clinics of North America—Small Animal Practice*, vol. 23, no. 2, pp. 461–469, 1993.

Review Article

Three-Dimensional Anatomic Evaluation of the Anterior Cruciate Ligament for Planning Reconstruction

Yuichi Hoshino, Donghwi Kim, and Freddie H. Fu

Department of Orthopaedic Surgery, University of Pittsburgh, Pittsburgh, PA 15213, USA

Correspondence should be addressed to Freddie H. Fu, ffu@upmc.edu

Anatomic study related to the anterior cruciate ligament (ACL) reconstruction surgery has been developed in accordance with the progress of imaging technology. Advances in imaging techniques, especially the move from two-dimensional (2D) to three-dimensional (3D) image analysis, substantially contribute to anatomic understanding and its application to advanced ACL reconstruction surgery. This paper introduces previous research about image analysis of the ACL anatomy and its application to ACL reconstruction surgery. Crucial bony landmarks for the accurate placement of the ACL graft can be identified by 3D imaging technique. Additionally, 3D-CT analysis of the ACL insertion site anatomy provides better and more consistent evaluation than conventional "clock-face" reference and roentgenologic quadrant method. Since the human anatomy has a complex three-dimensional structure, further anatomic research using three-dimensional imaging analysis and its clinical application by navigation system or other technologies is warranted for the improvement of the ACL reconstruction.

1. Introduction

Recent progress of the anterior cruciate ligament (ACL) reconstruction procedure and related research largely stems from the increased attention to the restoration of the original anatomy. An accurate evaluation of the native anatomy is critical for achieving anatomic ACL reconstruction. Clinical outcome could be imperfect when the graft placement is not located at an anatomic position [1, 2]. Also, conventional transtibial ACL reconstruction, which often locates the graft away from anatomic location [3], leads to abnormal biomechanical behavior and in vivo knee kinematics [4–6], which could influence long-term knee joint health [7, 8]. On the other hand, the anatomical ACL reconstruction procedure, either single-bundle or double-bundle technique, could provide better knee kinematics than nonanatomic reconstruction [9–11] and promising clinical results [12–20]. Appropriate anatomic evaluation of the native ACL for each individual patient can provide critical information for planning ACL reconstruction in an anatomic fashion, while postoperative evaluation of the reconstructed ACL graft location could predict the prognosis after the surgery and give valuable feedback to surgeons. In theory, a conventional two-

dimensional assessment cannot fully recognize the three-dimensional structure of the original anatomy. Therefore, three-dimensional imaging analysis of the knee has been progressively developed over the last few years [21, 22].

The purpose of this paper is to introduce the progression of imaging technology into three-dimensional analysis on various fields of research related to the ACL and to suggest the future direction of ACL-related anatomic studies.

2. Progression of the Imaging Technology for the ACL Anatomy

2.1. Image Analysis for the ACL Insertion Site. Anatomic research investigating the native ACL location has been developed over the last several decades. In 1975, Girgis et al. [23] investigated the cruciate ligaments in cadaveric knees focusing on their function and first recognized the different functional bundles of the ACL, the anteromedial (AM) and posterolateral (PL) bundles [23]. The relative positions between the two bundles were identified, while the exact locations were not determined due to lack of baseline anatomic landmarks and scales. In the 1980s, relative distances from the anatomic landmarks, such as the anterior

edge of the intercondylar notch, lateral condyle surface, and cartilage margin, on a hypothetical sagittal plane which was usually set on the lateral wall of the intercondylar notch were often used for describing the anatomical location. One of the examples of the two-dimensional anatomic description on the lateral wall of the intercondylar notch is the isometric mapping introduced by Sidles et al., which showed the relationship between the anatomical ACL graft location on a hypothetical plane and the length change of the graft [24]. They revealed that the original ACL insertion site is different from the isometric point where the graft does not change length during flexion-extension movement, whereas some cadaveric experiments at that time demonstrated that the anatomical location of the original ACL could produce the isometric length change pattern of the ACL graft [25, 26]. This disparity of the results could be caused by lack of common anatomic definition. In the 1990s, two-dimensional anatomical scales, such as the "clock-face" reference and quadrant method, were developed as a fixed and universal scaling method to describe the anatomical location of the ACL insertion site and graft placement. The "clock-face" reference has been utilized for referring the coronal position of the ACL insertion site and graft placement [27–29]. This reference system is able to be adopted for arthroscopic images [30]. However, a recent study shows that the interobserver variability is still high using the clock-face reference [31]. Interestingly, Siebold et al. demonstrated that the AM and PL were aligned at the same level on the "clock-face" reference, at 1:30 o'clock, when the knee flexed at 102 degrees [32]. It reversely implied that the anatomical location indicated by the clock-face reference can be easily modified by changing knee flexion angle. This critical flaw of the "clock-face" reference has been frequently pointed out [33, 34]. In the meantime, the quadrant method, originally described by Bernard et al. [35], is the most commonly used reference for the location of the ACL on the lateral X-ray of the distal femur [36–38]. However, this system depends crucially on an unstable baseline, Blumensaat's line, which is a projected line of the intercondylar roof on the lateral X-ray of the distal femur. Farrow et al. [39] demonstrated by cadaver experiment that the posterior edge of Blumensaat's line cannot be consistently recognized [39]. Also, Berg et al. [40] reported the large variability in the angle measurement of Blumensaat's line against the femoral shaft [40]. In addition, the anatomical location indicated by this system cannot be reproduced under arthroscopy. Also, the true lateral view of the distal femur is also extremely difficult to achieve by intraoperative fluoroscopy. Therefore, clinical value of this technique is assumed to be limited.

As anatomic double bundle ACL reconstruction was introduced in the 2000s, meticulous investigations of bony landmarks were conducted to identify useful landmarks which are available under arthroscopy and can be used for precise graft placements. Three-dimensional (3D) CT images contributed to this decade's progress of anatomic research. Purnell et al. [41] demonstrated that the lateral intercondylar ridge, formally known as "resident's ridge" [42], was clearly shown by the 3D CT image and can be defined as the anterior edge of the ACL original insertion site [41]. Furthermore,

Ferretti et al. [43] observed the bifurcate ridge on the lower third of the lateral wall which separates the AM and PL bundles [43], which can also be recognized by 3D CT image [44]. Although these tiny bony ridges are not always visible under arthroscopy [45], these osseous landmarks provides useful information for identifying the original ACL insertion site and performing the ACL reconstruction in an anatomic fashion [44]. Further advantage of the three-dimensional CT is the ability to arrange the rotation of the 3D image in a standardized orientation, providing consistent mapping of the ACL tunnel location [21]. This technique can be used for accurate and repeatable analysis of the ACL graft tunnel locations after reconstruction [3].

The progress of CT imaging technique from two- to three-dimensional has contributed significantly to the anatomic research of the ACL. Similar progress is still warranted for MRI because of its capacity to evaluate soft-tissue structures.

2.2. Imaging Analysis for Intercondylar Notch Geometry.
Femoral intercondylar notch width has been often discussed as a risk factor for the ACL injury, but it remains unknown if the narrow notch truly leads to ACL injury. Several studies evaluating intercondylar notch width by X-ray or CT reported narrow notch as a risk factor for the ACL injury [46–52]. Houseworth et al. [47] measured notch width using notch view, which is an AP view of the knee joint with 45 degrees of knee flexion, and demonstrated a correlation between femoral intercondylar notch stenosis and anterior cruciate ligament injuries [50]. However, other research cast doubt on the impact of the intercondylar notch stenosis [53, 54]. Schickendantz and Weiker [53] prospectively measured the notch width in professional basketball players, and their follow-up survey did not find significant difference of the notch width between ACL injured and noninjured players [53]. Those ambivalent results might be caused by the two-dimensional measurement of the intercondylar notch width. Van Eck et al. [55] compared two-dimensional and three-dimensional measurement of intercondylar notch geometry and demonstrated that there were only moderate correlations between those two measurement [55]. Since X-ray measurement is largely influenced by rotation and angulations [52], three-dimensional measurement is preferable to assess the intercondylar notch geometry.

2.3. Application to Navigation System for the ACL Reconstruction.
The development of 3D imaging techniques and increased attention to the anatomic procedure are accompanied with the advanced technology of computers and robots, leading to strong motivation for computer-assisted surgery which could provide real-time imaging feedback with the individualized anatomic information to the surgeons during ACL reconstruction.

In the early 1980s, computer-assisted ACL reconstruction was first attempted by the technique using stereotaxic frame of CT scan for brain surgery [56]. However, it was not commercialized due to excessive cost, invasiveness, and especially prolonged operation time due to computer processing.

An imageless navigation system was introduced in the mid-1990s [57], while anatomic placement drew increased attention because of higher revision rate as much as 10% to 40% due to inaccurate tunnel placement [58]. However, navigation-assisted ACL reconstruction was not accepted even though it had inherent accuracy mainly due to the invasiveness by fixing the tracker or exposing radiation and poor cost effectiveness [59]. Meanwhile, experimental use of the navigation system has flourished as an experimental tool. According to Zaffagnini et al., published research using navigation systems could be divided in two groups: anatomical studies (ligament insertion, tunnel position, graft isometry, and impingement) and kinematic studies (Lachman test, anterior drawer test, internal rotation and external rotation, and pivot shift test) [59]. Anatomic studies focused on the evaluation of graft length change and graft impingement against the intercondylar notch roof after ACL reconstruction [57] and the validation of the system accuracy [60], whereas knee kinematics evaluation by navigation system was largely performed to compare various operation techniques [61–64].

Navigation systems can be divided into image-guided [65] and imageless systems [56]. In an image-guided system, preoperative images from fluoroscopy, CT, or MRI are inputted and utilized to provide real-time feedback of anatomic information under arthroscopy. In imageless system, which is more common, positional information of anatomical landmarks and joint kinematics is intraoperatively registered for providing anatomic feedback. Nakagawa et al. [65] converted intraoperative 2D fluoroscopic picture into 3D image for preventing blow-out fractures while drilling the femoral tunnel [65]. However, their 2D-3D matching technique did not identify either lateral intercondylar ridge or bifurcate ridge [65].

Navigation systems can provide real-time quantitative feedback during arthroscopic procedure and minimize technical error with enhanced reproducibility and reliability [56, 66]. However, these systems must be improved before wider acceptance of the navigation system, such as invasiveness, cost effectiveness, and complexity of the navigation processing. Moreover, clear and reproducible definition of ideal tunnel position based on concrete anatomic baseline should be established to restore normal joint kinematics after ACL reconstruction.

3. Conclusion

Research on the anatomy of to the ACL has progressed along with the advancement of imaging and navigation technology. Useful bony landmarks for placing the ACL graft at the ideal position can be identified by 3D imaging technique. Also, 3D-CT analysis for the location of the native and reconstructed ACL provides better and more consistent evaluation than conventional "clock-face" reference and roentgenologic quadrant method. Three-dimensional image analysis of the ACL anatomy and its application to the navigation system is becoming more prevalent and reliable for advancing the anatomic studies related to the native ACL and the ACL reconstruction procedure.

Conflict of Interests

References

[1] B. G. Marchant, F. R. Noyes, S. D. Barber-Westin, and C. Fleckenstein, "Prevalence of nonanatomical graft placement in a series of failed anterior cruciate ligament reconstructions," *The American Journal of Sports Medicine*, vol. 38, no. 10, pp. 1987–1996, 2010.

[2] P. Aglietti, R. Buzzi, F. Giron, A. J. V. Simeone, and G. Zaccherotti, "Arthroscopic-assisted anterior cruciate ligament reconstruction with the central third patellar tendon: a 5–8-year follow-up," *Knee Surgery, Sports Traumatology, Arthroscopy*, vol. 5, no. 3, pp. 138–144, 1997.

[3] S. Kopf, B. Forsythe, A. K. Wong et al., "Nonanatomic tunnel position in traditional transtibial single-bundle anterior cruciate ligament reconstruction evaluated by three-dimensional computed tomography," *Journal of Bone and Joint Surgery. American*, vol. 92, no. 6, pp. 1427–1431, 2010.

[4] V. Musahl, A. Plakseychuk, A. VanScyoc et al., "Varying femoral tunnels between the anatomical footprint and isometric positions: effect on kinematics of the anterior cruciate ligaments-reconstructed knee," *The American Journal of Sports Medicine*, vol. 33, no. 5, pp. 712–718, 2005.

[5] S. Tashman, D. Collon, K. Anderson, P. Kolowich, and W. Anderst, "Abnormal rotational knee motion during running after anterior cruciate ligament reconstruction," *The American Journal of Sports Medicine*, vol. 32, no. 4, pp. 975–983, 2004.

[6] E. S. Abebe, G. M. Utturkar, D. C. Taylor et al., "The effects of femoral graft placement on in vivo knee kinematics after anterior cruciate ligament reconstruction," *Journal of Biomechanics*, vol. 44, pp. 924–929, 2011.

[7] T. P. Andriacchi, A. Mündermann, R. L. Smith, E. J. Alexander, C. O. Dyrby, and S. Koo, "A framework for the *in vivo* pathomechanics of osteoarthritis at the knee," *Annals of Biomedical Engineering*, vol. 32, no. 3, pp. 447–457, 2004.

[8] T. P. Andriacchi, P. L. Briant, S. L. Bevill, and S. Koo, "Rotational changes at the knee after ACL injury cause cartilage thinning," *Clinical Orthopaedics and Related Research*, no. 442, pp. 39–44, 2006.

[9] E. Kondo, A. M. Merican, K. Yasuda, and A. A. Amis, "Biomechanical comparison of anatomic double-bundle, anatomic single-bundle, and nonanatomic single-bundle anterior cruciate ligament reconstructions," *The American Journal of Sports Medicine*, vol. 39, pp. 279–288, 2011.

[10] M. Yagi, E. K. Wong, A. Kanamori, R. E. Debski, F. H. Fu, and S. L. Y. Woo, "Biomechanical analysis of an anatomic anterior cruciate ligament reconstruction," *The American Journal of Sports Medicine*, vol. 30, no. 5, pp. 660–666, 2002.

[11] Y. Yamamoto, W. H. Hsu, S. L. Y. Woo, A. H. Van Scyoc, Y. Takakura, and R. E. Debski, "Knee stability and graft function after anterior cruciate ligament reconstruction: a comparison of a lateral and an anatomical femoral tunnel placement," *The American Journal of Sports Medicine*, vol. 32, no. 8, pp. 1825–1832, 2004.

[12] D. Araki, R. Kuroda, S. Kubo et al., "A prospective randomised study of anatomical single-bundle versus double-bundle anterior cruciate ligament reconstruction: quantitative evaluation

using an electromagnetic measurement system," *International Orthopaedics*, vol. 35, pp. 439–446, 2011.

[13] P. Aglietti, F. Giron, M. Losco, P. Cuomo, A. Ciardullo, and N. Mondanelli, "Comparison between single- and double-bundle anterior cruciate ligament reconstruction: a prospective, randomized, single-blinded clinical trial," *The American Journal of Sports Medicine*, vol. 38, no. 1, pp. 25–34, 2010.

[14] R. Siebold, C. Dehler, and T. Ellert, "Prospective randomized comparison of double-bundle versus single-bundle anterior cruciate ligament reconstruction," *Arthroscopy*, vol. 24, no. 2, pp. 137–145, 2008.

[15] R. B. Meredick, K. J. Vance, D. Appleby, and J. H. Lubowitz, "Winner of the 2007 systematic review competition: outcome of single-bundle versus double-bundle reconstruction of the anterior cruciate ligament: a meta-analysis," *The American Journal of Sports Medicine*, vol. 36, no. 7, pp. 1414–1421, 2008.

[16] F. H. Fu, W. Shen, J. S. Starman, N. Okeke, and J. J. Irrgang, "Primary anatomic double-bundle anterior cruciate ligament reconstruction: a preliminary 2-year prospective study," *The American Journal of Sports Medicine*, vol. 36, no. 7, pp. 1263–1274, 2008.

[17] M. Yagi, R. Kuroda, K. Nagamune, S. Yoshiya, and M. Kurosaka, "Double-bundle ACL reconstruction can improve rotational stability," *Clinical Orthopaedics and Related Research*, no. 454, pp. 100–107, 2007.

[18] T. Muneta, H. Koga, T. Mochizuki et al., "A prospective randomized study of 4-strand semitendinosus tendon anterior cruciate ligament reconstruction comparing single-bundle and double-bundle techniques," *Arthroscopy*, vol. 23, no. 6, pp. 618–628, 2007.

[19] T. Järvelä, "Double-bundle versus single-bundle anterior cruciate ligament reconstruction: a prospective, randomize clinical study," *Knee Surgery, Sports Traumatology, Arthroscopy*, vol. 15, no. 5, pp. 500–507, 2007.

[20] P. Volpi, M. Cervellin, M. Denti et al., "ACL reconstruction in sports active people: transtibial DB technique with ST/G vs. transtibial SB technique with BPTB: preliminary results," *Injury*, vol. 41, no. 11, pp. 1168–1171, 2010.

[21] B. Forsythe, S. Kopf, A. K. Wong et al., "The location of femoral and tibial tunnels in anatomic double-bundle anterior cruciate ligament reconstruction analyzed by three-dimensional computed tomography models," *Journal of Bone and Joint Surgery. American*, vol. 92, no. 6, pp. 1418–1426, 2010.

[22] S. Lorenz, F. Elser, M. Mitterer, T. Obst, and A. B. Imhoff, "Radiologic evaluation of the insertion sites of the 2 functional bundles of the anterior cruciate ligament using 3-dimensional computed tomography," *The American Journal of Sports Medicine*, vol. 37, no. 12, pp. 2368–2376, 2009.

[23] F. G. Girgis, J. L. Marshall, and A. R. S. Al Monajem, "The cruciate ligaments of the knee joint. Anatomical, functional and experimental analysis," *Clinical Orthopaedics and Related Research*, vol. 106, pp. 216–231, 1975.

[24] J. A. Sidles, R. V. Larson, J. L. Garbini, D. J. Downey, and F. A. Matsen III, "Ligament length relationships in the moving knee," *Journal of Orthopaedic Research*, vol. 6, no. 4, pp. 593–610, 1988.

[25] T. Hoogland and B. Hillen, "Intra-articular reconstruction of the anterior cruciate ligament: an experimental study of length changes in different ligament reconstructions," *Clinical Orthopaedics and Related Research*, vol. 185, pp. 197–202, 1984.

[26] S. F. Schutzer, S. Christen, and R. P. Jakob, "Further observations on the isometricity of the anterior cruciate ligament: an anatomical study using a 6-mm diameter replacement," *Clinical Orthopaedics and Related Research*, no. 242, pp. 247–255, 1989.

[27] J. Loh, Y. Fukuda, E. Tsuda, R. Steadman, F. Fu, and S. Woo, "Knee stability and graft function following anterior cruciate ligament reconstruction: comparison between 11 o'clock and 10 o'clock femoral tunnel placement: 2002 Richard O'Connor Award paper," *Arthroscopy*, vol. 19, no. 3, pp. 297–304, 2003.

[28] C. S. Raffo, P. Pizzarello, J. C. Richmond, and N. Pathare, "A reproducible landmark for the tibial tunnel origin in anterior cruciate ligament reconstruction: avoiding a vertical graft in the coronal plane," *Arthroscopy*, vol. 24, no. 7, pp. 843–845, 2008.

[29] J. P. H. Rue, N. Ghodadra, and B. R. Bach Jr., "Femoral tunnel placement in single-bundle anterior cruciate ligament reconstruction: a cadaveric study relating transtibial lateralized femoral tunnel position to the anteromedial and posterolateral bundle femoral origins of the anterior cruciate ligament," *The American Journal of Sports Medicine*, vol. 36, no. 1, pp. 73–79, 2008.

[30] A. A. Amis and R. P. Jakob, "Anterior cruciate ligament graft positioning, tensioning and twisting," *Knee Surgery, Sports Traumatology, Arthroscopy*, vol. 6, supplement 1, pp. S2–S12, 1998.

[31] M. G. Azzam, C. J. Lenarz, L. D. Farrow, H. A. Israel, D. A. Kieffer, and S. G. Kaar, "Inter- and intraobserver reliability of the clock face representation as used to describe the femoral intercondylar notch," *Knee Surgery, Sports Traumatology, Arthroscopy*, vol. 19, no. 8, pp. 1265–1270, 2011.

[32] R. Siebold, T. Ellert, S. Metz, and J. Metz, "Femoral insertions of the anteromedial and posterolateral bundles of the anterior cruciate ligament: morphometry and arthroscopic orientation models for double-bundle bone tunnel placement—a cadaver study," *Arthroscopy*, vol. 24, no. 5, pp. 585–592, 2008.

[33] F. H. Fu, "The clock-face reference: simple but nonanatomic," *Arthroscopy*, vol. 24, no. 12, pp. 1433–1434, 2008.

[34] A. C. Colvin, W. Shen, V. Musahl, and F. H. Fu, "Avoiding pitfalls in anatomic ACL reconstruction," *Knee Surgery, Sports Traumatology, Arthroscopy*, vol. 17, no. 8, pp. 956–963, 2009.

[35] M. Bernard, P. Hertel, H. Hornung, and T. Cierpinski, "Femoral insertion of the ACL: radiographic quadrant method," *The American Journal of Knee Surgery*, vol. 10, no. 1, pp. 14–21, 1997.

[36] P. Colombet, J. Robinson, P. Christel et al., "Morphology of anterior cruciate ligament attachments for anatomic reconstruction: a cadaveric dissection and radiographic study," *Arthroscopy*, vol. 22, no. 9, pp. 984–992, 2006.

[37] M. Takahashi, M. Doi, M. Abe, D. Suzuki, and A. Nagano, "Anatomical study of the femoral and tibial insertions of the anteromedial and posterolateral bundles of human anterior cruciate ligament," *The American Journal of Sports Medicine*, vol. 34, no. 5, pp. 787–792, 2006.

[38] T. Zantop, M. Wellmann, F. H. Fu, and W. Petersen, "Tunnel positioning of anteromedial and posterolateral bundles in anatomic anterior cruciate ligament reconstruction: anatomic and radiographic findings," *The American Journal of Sports Medicine*, vol. 36, no. 1, pp. 65–72, 2008.

[39] L. D. Farrow, M. R. Chen, D. R. Cooperman, D. B. Goodfellow, and M. S. Robbin, "Radiographic classification of the femoral intercondylar notch posterolateral rim," *Arthroscopy*, vol. 24, no. 10, pp. 1109–1114, 2008.

[40] G. E. Berg, S. C. Ta'ala, E. J. Kontanis, and S. S. Leney, "Measuring the intercondylar shelf angle using radiographs: intra- and inter-observer error tests of reliability," *Journal of Forensic Sciences*, vol. 52, no. 5, pp. 1020–1024, 2007.

[41] M. L. Purnell, A. I. Larson, and W. Clancy, "Anterior cruciate ligament insertions on the tibia and femur and their relationships to critical bony landmarks using high-resolution volume-rendering computed tomography," *The American Journal of Sports Medicine*, vol. 36, no. 11, pp. 2083–2090, 2008.

[42] M. R. Hutchinson and S. A. Ash, "Resident's ridge: assessing the cortical thickness of the lateral wall and roof of the intercondylar notch," *Arthroscopy*, vol. 19, no. 9, pp. 931–935, 2003.

[43] M. Ferretti, M. Ekdahl, W. Shen, and F. H. Fu, "Osseous landmarks of the femoral attachment of the anterior cruciate ligament: an anatomic study," *Arthroscopy*, vol. 23, no. 11, pp. 1218–1225, 2007.

[44] F. H. Fu and S. S. Jordan, "The lateral intercondylar ridge—a key to anatomic anterior cruciate ligament reconstruction," *Journal of Bone and Joint Surgery. American*, vol. 89, no. 10, pp. 2103–2104, 2007.

[45] C. F. van Eck, K. R. Morse, B. P. Lesniak et al., "Does the lateral intercondylar ridge disappear in ACL deficient patients?" *Knee Surgery, Sports Traumatology, Arthroscopy*, vol. 18, no. 9, pp. 1184–1188, 2010.

[46] A. F. Anderson, A. B. Lipscomb, K. J. Liudahl, and R. B. Addlestone, "Analysis of the intercondylar notch by computed tomography," *The American Journal of Sports Medicine*, vol. 15, no. 6, pp. 547–552, 1987.

[47] S. W. Houseworth, V. J. Mauro, B. A. Mellon, and D. A. Kieffer, "The intercondylar notch in acute tears of the anterior cruciate ligament: a computer graphics study," *The American Journal of Sports Medicine*, vol. 15, no. 3, pp. 221–224, 1987.

[48] T. O. Souryal, H. A. Moore, and J. P. Evans, "Bilaterality in anterior cruciate ligament injuries: associated intercondylar notch stenosis," *The American Journal of Sports Medicine*, vol. 16, no. 5, pp. 449–454, 1988.

[49] T. O. Souryal, T. R. Freeman, and D. M. Daniel, "Intercondylar notch size and anterior cruciate ligament injuries in athletes: a prospective study," *The American Journal of Sports Medicine*, vol. 21, no. 4, pp. 535–539, 1993.

[50] R. F. LaPrade, Q. M. Burnett II, and D. M. Daniel, "Femoral intercondylar notch stenosis and correlation to anterior cruciate ligament injuries: a prospective study," *The American Journal of Sports Medicine*, vol. 22, no. 2, pp. 198–203, 1994.

[51] K. D. Shelbourne, T. J. Davis, and T. E. Klootwyk, "The relationship between intercondylar notch width of the femur and the incidence of anterior cruciate ligament tears: a prospective study," *The American Journal of Sports Medicine*, vol. 26, no. 3, pp. 402–408, 1998.

[52] M. L. Ireland, B. T. Ballantyne, K. Little, and I. S. McClay, "A radiographic analysis of the relationship between the size and shape of the intercondylar notch and anterior cruciate ligament injury," *Knee Surgery, Sports Traumatology, Arthroscopy*, vol. 9, no. 4, pp. 200–205, 2001.

[53] M. S. Schickendantz and G. G. Weiker, "The predictive value of radiographs in the evaluation of unilateral and bilateral anterior cruciate ligament injuries," *The American Journal of Sports Medicine*, vol. 21, no. 1, pp. 110–113, 1993.

[54] S. Lombardo, P. M. Sethi, and C. Starkey, "Intercondylar notch stenosis is not a risk factor for anterior cruciate ligament tears in professional male basketball players: an 11-year prospective study," *The American Journal of Sports Medicine*, vol. 33, no. 1, pp. 29–34, 2005.

[55] C. F. van Eck, C. A. Q. Martins, S. Kopf, P. Lertwanich, F. H. Fu, and S. Tashman, "Correlation between the 2-dimensional notch width and the 3-dimensional notch volume: a cadaveric study," *Arthroscopy*, vol. 27, pp. 207–212, 2011.

[56] D. W. Jackson and T. M. Simon, "History of computer-assisted orthopedic surgery (CAOS) in sports medicine," *Sports Medicine and Arthroscopy Review*, vol. 16, no. 2, pp. 62–66, 2008.

[57] V. Dessenne, S. Lavallée, R. Julliard, R. Orti, S. Martelli, and P. Cinquin, "Computer-assisted knee anterior cruciate ligament reconstruction: first clinical tests," *Journal of Image Guided Surgery*, vol. 1, no. 1, pp. 59–64, 1995.

[58] M. J. Wetzler, A. R. Bartolozzi, M. J. Gillespie, D. L. Rubenstein, M. G. Ciccotti, and L. S. Miller, "Revision anterior cruciate ligament reconstruction," *Operative Techniques in Orthopaedics*, vol. 6, no. 3, pp. 181–189, 1996.

[59] S. Zaffagnini, T. V. Klos, and S. Bignozzi, "Computer-assisted anterior cruciate ligament reconstruction: an evidence-based approach of the first 15 years," *Arthroscopy*, vol. 26, no. 4, pp. 546–554, 2010.

[60] T. V. S. Klos, R. J. E. Habets, A. Z. Banks, S. A. Banks, R. J. J. Devilee, and F. F. Cook, "Computer assistance in arthroscopic anterior cruciate ligament reconstruction," *Clinical Orthopaedics and Related Research*, no. 354, pp. 65–69, 1998.

[61] V. Musahl, J. E. Voos, P. F. O'Loughlin et al., "Comparing stability of different single-and double-bundle anterior cruciate ligament reconstruction techniques: a cadaveric study using navigation," *Arthroscopy*, vol. 26, no. 9, pp. S41–S48, 2010.

[62] J. Y. Ho, A. Gardiner, V. Shah, and M. E. Steiner, "Equal kinematics between central anatomic single-bundle and double-bundle anterior cruciate ligament reconstructions," *Arthroscopy*, vol. 25, no. 5, pp. 464–472, 2009.

[63] A. Ferretti, E. Monaco, L. Labianca, A. De Carli, B. Maestri, and F. Conteduca, "Double-bundle anterior cruciate ligament reconstruction: a comprehensive kinematic study using navigation," *The American Journal of Sports Medicine*, vol. 37, no. 8, pp. 1548–1553, 2009.

[64] R. H. Brophy and A. D. Pearle, "Single-bundle anterior cruciate ligament reconstruction: a comparison of conventional, central, and horizontal single-bundle virtual graft positions," *The American Journal of Sports Medicine*, vol. 37, no. 7, pp. 1317–1323, 2009.

[65] T. Nakagawa, H. Takeda, K. Nakajima et al., "Intraoperative 3-dimensional imaging-based navigation-assisted anatomic double-bundle anterior cruciate ligament reconstruction," *Arthroscopy*, vol. 24, no. 10, pp. 1161–1167, 2008.

[66] P. Kodali, S. Yang, and J. Koh, "Computer-assisted surgery for anterior cruciate ligament reconstruction," *Sports Medicine and Arthroscopy Review*, vol. 16, no. 2, pp. 67–76, 2008.

Research Article

Tridimensional Regression for Comparing and Mapping 3D Anatomical Structures

Kendra K. Schmid,[1] David B. Marx,[2] and Ashok Samal[3]

[1] *Department of Biostatistics, College of Public Health, University of Nebraska Medical Center, 984375 Nebraska Medical Center, Omaha, NE 68198-4375, USA*
[2] *Department of Statistics, University of Nebraska-Lincoln, 340 Hardin Hall North, Lincoln, NE, 68583-0963, USA*
[3] *Department of Computer Science and Engineering, University of Nebraska-Lincoln, Lincoln, NE 68588-0115, USA*

Correspondence should be addressed to Kendra K. Schmid, kkschmid@unmc.edu

Shape analysis is useful for a wide variety of disciplines and has many applications. There are many approaches to shape analysis, one of which focuses on the analysis of shapes that are represented by the coordinates of predefined landmarks on the object. This paper discusses Tridimensional Regression, a technique that can be used for mapping images and shapes that are represented by sets of three-dimensional landmark coordinates, for comparing and mapping 3D anatomical structures. The degree of similarity between shapes can be quantified using the tridimensional coefficient of determination (R^2). An experiment was conducted to evaluate the effectiveness of this technique to correctly match the image of a face with another image of the same face. These results were compared to the R^2 values obtained when only two dimensions are used and show that using three dimensions increases the ability to correctly match and discriminate between faces.

1. Introduction

Tobler [1] proposed bidimensional regression as a tool for computing the degree of similarity between two planar configurations of points and to estimate mapping relations between two objects that are represented by a set of two-dimensional landmarks. Bidimensional regression is an extension of linear regression where both dependent and independent variables are represented by coordinate pairs, instead of scalar values. Specifically, Tobler [1] suggested that bidimensional regression may be useful for comparing signatures, geographical maps, or faces. The latter was done in the context of face recognition by Shi et al. [2] and Kare et al. [3].

Tobler's [1] method has been extended to *Tridimensional Regression* for situations when both dependent and independent variables are represented by three-dimensional coordinates [4]. The purpose of this paper is to provide a summary of that extension, to illustrate the use of tridimensional regression for comparing and mapping anatomical structures, and to compare the effectiveness of the two-dimensional and three-dimensional methods. Widespread use of three-dimensional imaging devices in many areas of research makes this research timely. This technique is broadly applicable to any situation where spatial configurations of three-dimensional points are compared. Specific instances where tridimensional regression may be of use are three-dimensional mapping and comparison of objects or structures that are represented by their three-dimensional coordinates. The R^2 values derived from regression allow the degree of similarity between two objects to be quantified.

2. Methods

In this section, a brief summary of bidimensional regression and its extension to three dimensions is provided. Details of the tridimensional regression models are provided.

2.1. Bidimensional Regression. Nakaya [5] defines a bidimensional regression model as

$$\begin{pmatrix} u_i \\ v_i \end{pmatrix} = \begin{pmatrix} g(x_i, y_i) \\ h(x_i, y_i) \end{pmatrix} + \begin{pmatrix} \varepsilon_i \\ \eta_i \end{pmatrix}, \tag{1}$$

where (u_i, v_i) is the dependent variable, (x_i, y_i) represent the corresponding coordinates of the independent variable, g and h are transformation functions used to estimate mapping relations between independent and dependent variables, and (ε_i, η_i) is an error vector that is assumed to be normally and independently distributed. Both Tobler [1] and Nakaya [5] discuss obtaining estimates for parameters in g and h using the method of least-squares so that

$$\sum_{i=1}^{n}\left[\left(u_i - \hat{g}(x_i, y_i)\right)^2 + \left(v_i - \hat{h}(x_i, y_i)\right)^2\right], \qquad (2)$$

where $\hat{g}$ and $\hat{h}$ are the transformation functions evaluated at the parameter estimates, is minimized. Here n is the number of landmark points used in the analysis. The normal equations are obtained in the usual manner [1], and by solving $\hat{\boldsymbol{\beta}}_j$ in

$$\mathbf{X}_j^T \mathbf{X}_j \hat{\boldsymbol{\beta}}_j = \mathbf{X}_j^T \mathbf{Y}, \qquad (3)$$

where $\mathbf{X}_j$ is the design matrix of transformation j and $\mathbf{Y} = \begin{bmatrix} \mathbf{u} & \mathbf{v} \end{bmatrix}^T$ is a $(2n \times 1)$ vector for the dependent variable partitioned by the coordinates, will yield the least-squares parameter estimates [6]. The design matrix $(\mathbf{X}_j)$ will depend on the transformation used and the number of parameters to estimate; hence, the dimension of $\hat{\boldsymbol{\beta}}_j$ will also be determined by the type of transformation.

Tobler [1] proposes four bidimensional regression models, three of which are intrinsically linear and one is curvilinear. Friedman and Kohler [7] argue that the curvilinear model may be too general for practical use and describe the linear transformations in more detail. Each of the other three transformations is linearized by reparameterization prior to solving the parameter estimates.

The three linear transformations yield the Euclidean, affine, and projective models where in each model the original coordinates are scaled, rotated, and translated. These transformations form a hierarchy with the Euclidean being the simplest (fewest parameters) and the projective the most complex (most parameters) of the models.

Details of bidimensional regression models can be found in [1, 5, 7, 8]. Briefly, the Euclidean model is a similarity transformation in that the overall shape remains unchanged. The coordinates are translated, rotated, and isotropically scaled [8], thus preserving the original shape and angles. The affine model allows for X and Y coordinates to be scaled independently, and the configuration could exhibit shear (γ) (e.g., a square may become a parallelogram; Figure 1). The projective transformation, which is the most complex, allows the size, shape, and orientation to change as a function of viewpoint [7]. An example of a projective transformation is shown in Figure 2.

In the Euclidean and affine transformations, the models are linearized by reparameterization, and then the normal equations can be derived in the usual manner. Once the parameters have been estimated [7], provide equations for calculating the scale and rotation values for the Euclidean
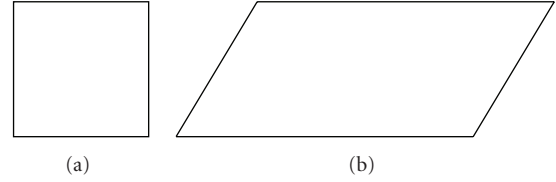

Figure 1: Example of a bidimensional affine transformation.

transformation and the scale, shear, and rotation values for the affine transformation.

The equations for the projective transformation can be rewritten using homogeneous coordinates and put in matrix notation as shown in (16). Homogeneous coordinates can be used with any of the models to provide a uniform framework for all transformations. For rotation, scaling, and shear, the transformed coordinates can be expressed as the product of a transformation matrix and the original coordinates. For translation, however, the coordinates are derived by addition of the translation vector to the original coordinates. Use of homogeneous coordinates makes all the transformations multiplicative. This is accomplished by adding an additional coordinate (t), called the homogeneous coordinate.

The homogeneous coordinate is added purely for mathematical simplification and has no effect on the transformation of coordinates. For example, it is convenient to represent a sequence of transformations as the product of the corresponding transformation matrices. Thus, in the Euclidean and affine models, the translation parameters become multiplicative and one matrix could be used for all of the transformation parameters [10]. With the projective model, the conversion is used to linearize the model, and once the object is mapped using homogeneous coordinates, the original coordinates are restored by dividing by the homogeneous coordinate, t. However, when this is done, the restriction placed on t results in parameter estimates of $\hat{\beta}_{31} = 0$, $\hat{\beta}_{32} = 0$, and $\hat{\beta}_{33} = 1$. Consequently, the projective transformation is reduced to the affine transformation and the results are identical. The conversion to homogeneous coordinates is adequate for determining the location of transformed points, but not for obtaining transformation parameter estimates. If left in terms of the original equations, the parameters of the projective transformation can be estimated using nonlinear regression. When extended to three dimensions, a similar approach is used.

The similarity of the two objects is assessed using the bidimensional correlation coefficient [1],

$$R_{2D} = \sqrt{1 - \frac{\sum_i\left\{(u_i - \hat{u}_i)^2 + (v_i - \hat{v}_i)^2\right\}}{\sum_i\left\{(u_i - \overline{u})^2 + (v_i - \overline{v})^2\right\}}}. \qquad (4)$$

2.2. Tridimensional Regression. The bidimensional regression models proposed by Tobler [1] can be extended to instances where three-dimensional data are used for comparison. A specific instance may include anatomical structures that are represented by three-dimensional landmark coordinates, but tridimensional regression can be useful for
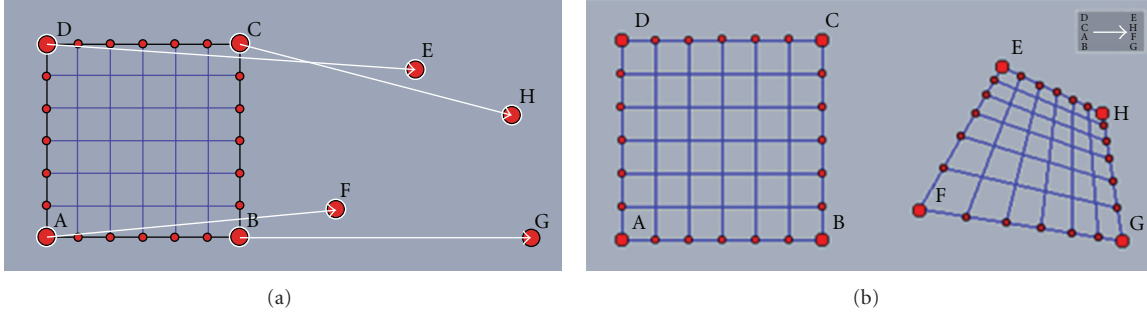
(a)

(b)

FIGURE 2: Example of a bidimensional projective transformation (ABCD → FGHE) [9].

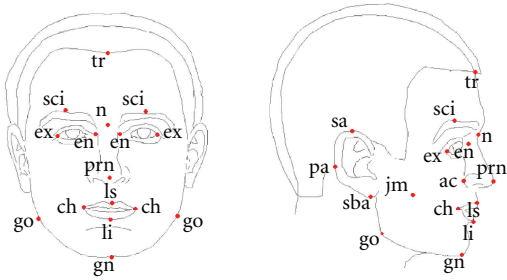FIGURE 3: Example of a tridimensional affine transformation [12].

FIGURE 4: Landmarks used for evaluating tridimensional regression.

determining the degree of similarity between any two objects that are represented by three-dimensional coordinates.

In this paper, the linear transformations discussed by Tobler [1] will be extended to three dimensions. Extensions to the Euclidean, affine, and projective transformations are described in detail where the dependent and independent variables are represented by their three-dimensional coordinates,

$$
\begin{pmatrix} u_i \\ v_i \\ w_i \end{pmatrix}, \qquad \begin{pmatrix} x_i \\ y_i \\ z_i \end{pmatrix}, \text{ respectively.} \tag{5}
$$

2.2.1. Euclidean Transformation. The three-dimensional Euclidean transformation is similar to the two-dimensional case in that coordinates are simply translated, rotated, and isotropically scaled. The overall shape and the angles of the original object are preserved, and parallel lines in the original object are mapped to parallel lines in the transformed space. There is an additional translation parameter, and the rotation matrix differs depending on which axis(es) are used for the rotation. In general, the number of rotation parameters is

$k(k-1)/2$, where k is the number of dimensions. Therefore, there are three rotation parameters for the general three-dimensional Euclidean transformation. However, for instances when it is known that all three rotations are not necessary, the transformation can be reduced to one or two rotations. These special cases are discussed in detail in [4].

Three-Dimensional Euclidean Transformation with One Angle of Rotation. The format of the rotation matrix depends on the axis of rotation. The formats for each of the three rotations are shown below, where γ is the angle of rotation about the x-axis, θ is the angle of rotation about the y-axis, and ϕ is the angle of rotation about the z-axis:

$$
\begin{aligned}
\mathbf{R_X} &= \begin{bmatrix} 1 & 0 & 0 \\ 0 & \cos\gamma & -\sin\gamma \\ 0 & \sin\gamma & \cos\gamma \end{bmatrix}, \\[2mm]
\mathbf{R_Y} &= \begin{bmatrix} \cos\theta & 0 & \sin\theta \\ 0 & 1 & 0 \\ -\sin\theta & 0 & \cos\theta \end{bmatrix}, \\[2mm]
\mathbf{R_Z} &= \begin{bmatrix} \cos\phi & -\sin\phi & 0 \\ \sin\phi & \cos\phi & 0 \\ 0 & 0 & 1 \end{bmatrix}.
\end{aligned} \tag{6}
$$

The general form of the three-dimensional Euclidean transformation is

$$
\begin{bmatrix} u_i \\ v_i \\ w_i \end{bmatrix} = \begin{bmatrix} \alpha_1 \\ \alpha_2 \\ \alpha_3 \end{bmatrix} + s\mathbf{R}\begin{bmatrix} x_i \\ y_i \\ z_i \end{bmatrix}, \tag{7}
$$

where $\mathbf{R}$ is one of the rotation matrices.

As in the two-dimensional case, the transformation can be linearized by reparameterization, where the new transformation matrix ($\mathbf{R}'$) is a combination of the scale and rotation parameters. The reparameterized transformations and their normal equations follow.
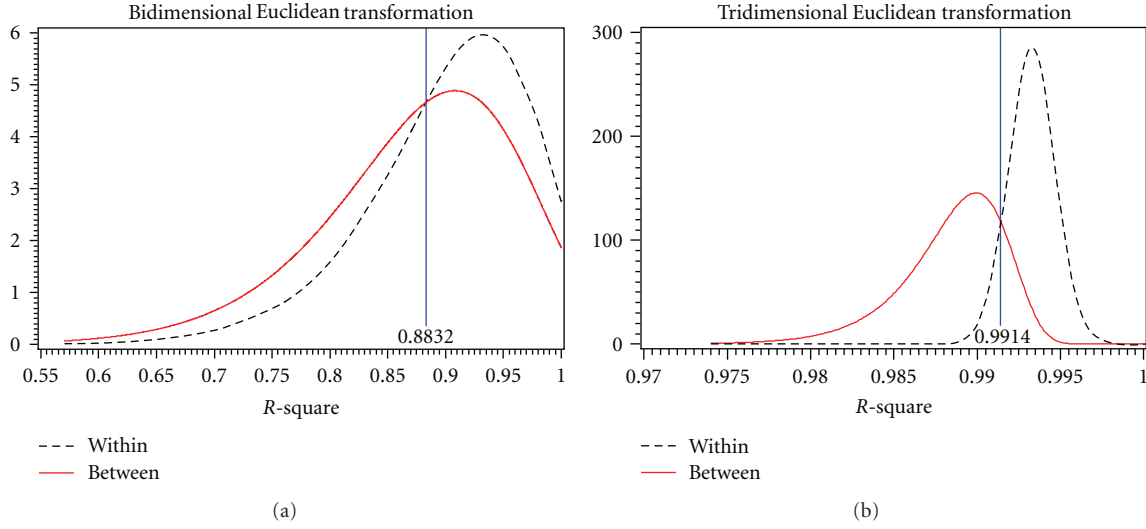
FIGURE 5: Within and between person R^2 for bidimensional (l) and tridimensional (r) Euclidean transformation.
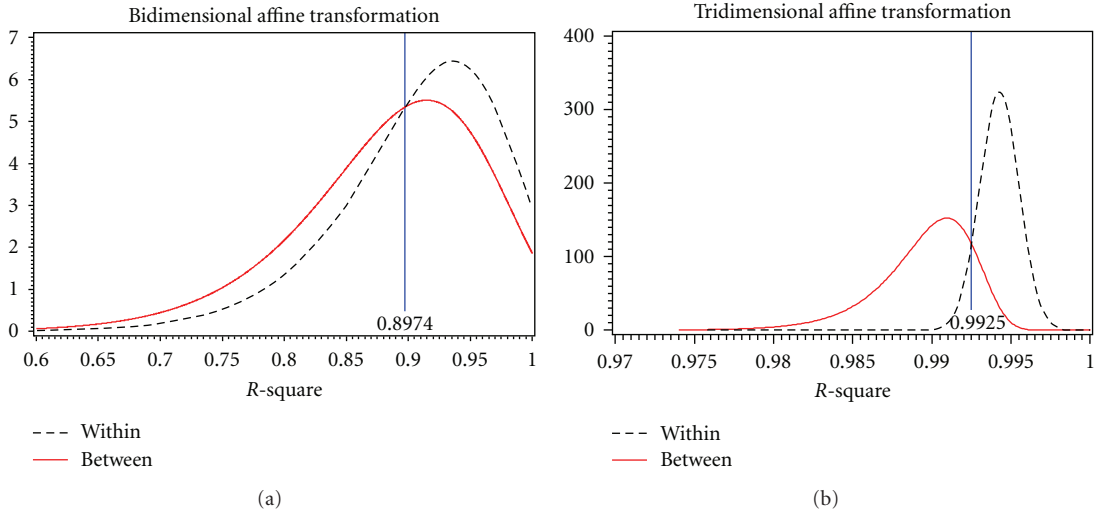
FIGURE 6: Within and between person R^2 for bidimensional (l) and tridimensional (r) affine transformation.

For rotation about the x-axis,

$$\mathbf{R}'_{\mathbf{X}} = \begin{bmatrix} 1 & 0 & 0 \\ 0 & \beta_1 & -\beta_2 \\ 0 & \beta_2 & \beta_1 \end{bmatrix},$$

$$u_i = \alpha_1 + x_i,$$

$$v_i = \alpha_2 + \beta_1 y_i - \beta_2 z_i,$$

$$w_i = \alpha_3 + \beta_2 y_i + \beta_1 z_i,$$

(8)

and deriving the normal equations in the usual manner yields

$$\begin{bmatrix} N & 0 & 0 & 0 & 0 \\ 0 & N & 0 & \sum y_i & -\sum z_i \\ 0 & 0 & N & \sum z_i & \sum y_i \\ 0 & \sum y_i & \sum z_i & \sum(y_i^2 + z_i^2) & 0 \\ 0 & -\sum z_i & \sum y_i & 0 & \sum(y_i^2 + z_i^2) \end{bmatrix} \begin{bmatrix} \alpha_1 \\ \alpha_2 \\ \alpha_3 \\ \beta_1 \\ \beta_2 \end{bmatrix}$$

$$= \begin{bmatrix} \sum(u_i - x_i) \\ \sum v_i \\ \sum w_i \\ \sum(v_i y_i + w_i z_i) \\ \sum(w_i y_i - v_i z_i) \end{bmatrix}.$$
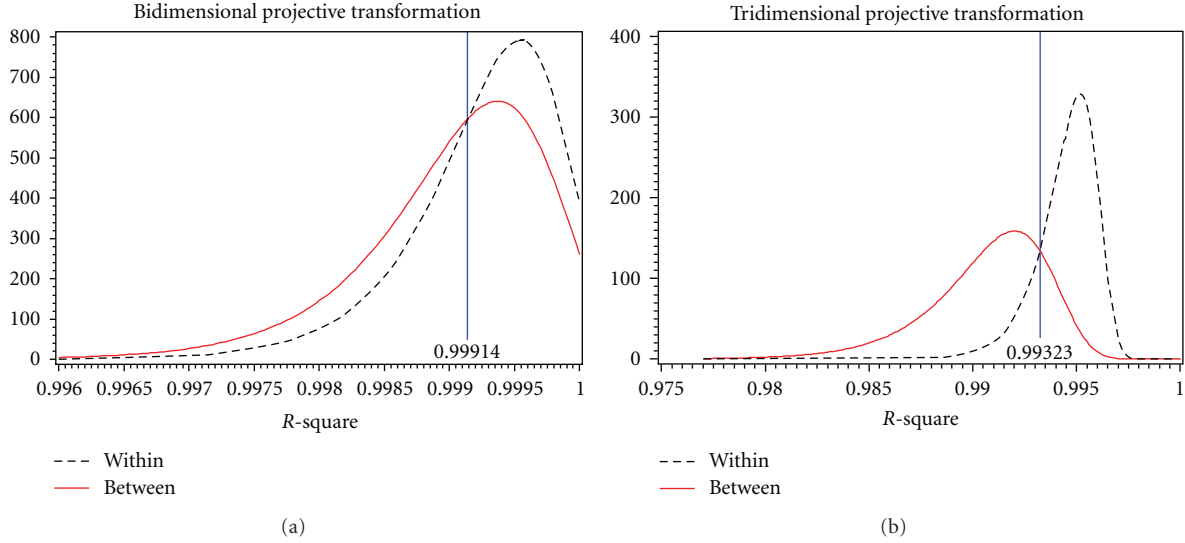
(9)

FIGURE 7: Within and between person R^2 for bidimensional (l) and tridimensional (r) projective transformation.

Similar details for rotation about the y and z axes can be found in [4].

Three-Dimensional Euclidean Transformation with Multiple Angles of Rotation. When more than one rotation is used, the reparameterization to linearize the model is not obvious; therefore, the rotation matrices remain in terms of the rotation parameters and nonlinear regression is used. The advantage of using nonlinear regression is that the rotation and scale parameters are directly estimated instead of being solved in terms of β_i; the disadvantage in using nonlinear regression is convergence may not be reached and starting values must be specified. The similarity of the two objects is assessed using the Pseudo-R^2 as defined by [11]. The Pseudo-R^2 is calculated in the same manner as R^2, but, in general, is not guaranteed to be greater than zero. Again, the rotation matrix differs depending upon the axes of rotation. An example of a two-rotation Euclidean transformation is shown below.

$$\begin{bmatrix} u_i \\ v_i \\ w_i \end{bmatrix} = \begin{bmatrix} \alpha_1 \\ \alpha_2 \\ \alpha_3 \end{bmatrix} + s \begin{bmatrix} \cos\theta\cos\phi & -\cos\theta\sin\phi & \sin\theta \\ \sin\gamma\sin\theta\cos\phi + \cos\gamma\sin\phi & -\sin\gamma\sin\theta\sin\phi + \cos\gamma\cos\phi & -\sin\gamma\cos\theta \\ -\cos\gamma\sin\theta\cos\phi + \sin\gamma\sin\phi & \cos\gamma\sin\theta\sin\phi + \sin\gamma\cos\phi & \cos\gamma\cos\theta \end{bmatrix} \begin{bmatrix} x_i \\ y_i \\ z_i \end{bmatrix}. \tag{11}$$

2.2.2. Affine Transformation. The extension of the affine transformation from two dimensions into three dimensions includes additional parameters for translation, scaling, rotation, and shear. Figure 3 shows an example of a three-dimensional affine transformation. The transformed coordinates in affine transformations are given by

$$u_i = \alpha_1 + \beta_{11}x_i + \beta_{12}y_i + \beta_{13}z_i,$$

For rotation about x and y axes,

$$\begin{bmatrix} u_i \\ v_i \\ w_i \end{bmatrix} = \begin{bmatrix} \alpha_1 \\ \alpha_2 \\ \alpha_3 \end{bmatrix} + s \begin{bmatrix} \cos\theta & 0 & \sin\theta \\ \sin\gamma\sin\theta & \cos\gamma & -\sin\gamma\cos\theta \\ -\cos\gamma\sin\theta & \sin\gamma & \cos\gamma\cos\theta \end{bmatrix} \begin{bmatrix} x_i \\ y_i \\ z_i \end{bmatrix}. \tag{10}$$

In the general form of the three-dimensional Euclidean transformation, the order in which the transformations are applied will result in different parameter estimates. Permuting this order will result in different estimates of the rotation parameters, but the measure of similarity will remain the same regardless of the order of transformations. The following system of equations shows the rotations in the order of x-axis, y-axis, and then z-axis:

$$v_i = \alpha_2 + \beta_{21}x_i + \beta_{22}y_i + \beta_{23}z_i,$$

$$w_i = \alpha_3 + \beta_{31}x_i + \beta_{32}y_i + \beta_{33}z_i,$$

$$\begin{bmatrix} u_i \\ v_i \\ w_i \end{bmatrix} = \begin{bmatrix} \alpha_1 \\ \alpha_2 \\ \alpha_3 \end{bmatrix} + \begin{bmatrix} \beta_{11} & \beta_{12} & \beta_{13} \\ \beta_{21} & \beta_{22} & \beta_{23} \\ \beta_{31} & \beta_{32} & \beta_{33} \end{bmatrix} \begin{bmatrix} x_i \\ y_i \\ z_i \end{bmatrix}. \tag{12}$$

Deriving the normal equations in the usual manner yields

$$
\begin{bmatrix}
\mathbf{I}_3 \otimes N & \mathbf{I}_3 \otimes \left(\sum x_i \quad \sum y_i \quad \sum z_i \right) \\
\mathbf{I}_3 \otimes \begin{pmatrix} \sum x_i \\ \sum y_i \\ \sum z_i \end{pmatrix} & \mathbf{I}_3 \otimes \begin{pmatrix} \sum x_i^2 & \sum x_i y_i & \sum x_i z_i \\ \sum x_i y_i & \sum y_i^2 & \sum y_i z_i \\ \sum x_i z_i & \sum y_i z_i & \sum z_i^2 \end{pmatrix}
\end{bmatrix}
\begin{bmatrix}
\alpha_1 \\ \alpha_2 \\ \alpha_3 \\ \beta_{11} \\ \beta_{12} \\ \beta_{13} \\ \beta_{21} \\ \beta_{22} \\ \beta_{23} \\ \beta_{31} \\ \beta_{32} \\ \beta_{33}
\end{bmatrix}
$$

$$
= \begin{bmatrix}
\sum u_i \\
\sum v_i \\
\sum w_i \\
\sum u_i x_i \\
\sum u_i y_i \\
\sum u_i z_i \\
\sum v_i x_i \\
\sum v_i y_i \\
\sum v_i z_i \\
\sum w_i x_i \\
\sum w_i y_i \\
\sum w_i z_i
\end{bmatrix},
\tag{13}
$$

where $\mathbf{I}_3$ is a 3×3 identity matrix and $\otimes$ is the direct product of the two matrices.

2.2.3. Projective Transformation.

The extension of the projective transformation from two to three dimensions involves the conversion to homogeneous coordinates (16). Additional parameters are added corresponding to the coordinate of the third dimension. In a projective transformation, the size, shape, and orientation can all change as a function of viewpoint. While this is a nonlinear transformation, by using homogeneous coordinates, the model can be linearized in order to obtain the normal equations and estimate the parameters. The equations to obtain the transformed coordinates are

$$
u_i = \frac{\beta_{11} x_i + \beta_{12} y_i + \beta_{13} z_i + \beta_{14}}{\beta_{41} x_i + \beta_{42} y_i + \beta_{43} z_i + \beta_{44}},
$$

$$
v_i = \frac{\beta_{21} x_i + \beta_{22} y_i + \beta_{23} z_i + \beta_{24}}{\beta_{41} x_i + \beta_{42} y_i + \beta_{43} z_i + \beta_{44}},
$$

$$
w_i = \frac{\beta_{31} x_i + \beta_{32} y_i + \beta_{33} z_i + \beta_{34}}{\beta_{41} x_i + \beta_{42} y_i + \beta_{43} z_i + \beta_{44}},
$$

$$
\begin{bmatrix} u_i t \\ v_i t \\ w_i t \\ t \end{bmatrix} =
\begin{bmatrix}
\beta_{11} & \beta_{12} & \beta_{13} & \beta_{14} \\
\beta_{21} & \beta_{22} & \beta_{23} & \beta_{24} \\
\beta_{31} & \beta_{32} & \beta_{33} & \beta_{34} \\
\beta_{41} & \beta_{42} & \beta_{43} & \beta_{44}
\end{bmatrix}
\begin{bmatrix} x_i \\ y_i \\ z_i \\ 1 \end{bmatrix}.
\tag{14}
$$

Let

$$
u_i' = u_i t,
$$
$$
v_i' = v_i t,
\tag{15}
$$
$$
w_i' = w_i t,
$$

then

$$
\begin{bmatrix} u_i' \\ v_i' \\ w_i' \\ t \end{bmatrix} =
\begin{bmatrix}
\beta_{11} & \beta_{12} & \beta_{13} & \beta_{14} \\
\beta_{21} & \beta_{22} & \beta_{23} & \beta_{24} \\
\beta_{31} & \beta_{32} & \beta_{33} & \beta_{34} \\
\beta_{41} & \beta_{42} & \beta_{43} & \beta_{44}
\end{bmatrix}
\begin{bmatrix} x_i \\ y_i \\ z_i \\ 1 \end{bmatrix},
\tag{16}
$$

and deriving the normal equations in the usual manner yields

$$
\left(\mathbf{I}_4 \otimes \begin{bmatrix}
\sum x^2 & \sum xy & \sum xz & \sum x \\
\sum xy & \sum y^2 & \sum yz & \sum y \\
\sum xz & \sum yz & \sum z^2 & \sum z \\
\sum x & \sum y & \sum z & N
\end{bmatrix} \right)
\begin{pmatrix}
\beta_{11} \\ \beta_{12} \\ \beta_{13} \\ \beta_{14} \\ \beta_{21} \\ \beta_{22} \\ \beta_{23} \\ \beta_{24} \\ \beta_{31} \\ \beta_{32} \\ \beta_{33} \\ \beta_{34} \\ \beta_{41} \\ \beta_{42} \\ \beta_{43} \\ \beta_{44}
\end{pmatrix}
=
\begin{pmatrix}
\sum ux \\ \sum uy \\ \sum uz \\ \sum u \\ \sum vx \\ \sum vy \\ \sum vz \\ \sum v \\ \sum wx \\ \sum wy \\ \sum wz \\ \sum w \\ \sum tx \\ \sum ty \\ \sum tz \\ \sum t
\end{pmatrix},
\tag{17}
$$

where $\mathbf{I}_4$ is a 4×4 identity matrix and $\otimes$ is the direct product of the two matrices.

As described in [4], this linearization results in parameter estimates that reduce the transformation to affine. The linearization is adequate to determine the transformed points, but not for the optimization to determine the transformation parameters or for measuring the degree of similarity between the two objects. Therefore, the transformation is left in terms of the original equations and nonlinear regression is used to obtain parameter estimates.

Nonlinear regression is an extension of linear regression where the expected responses are nonlinear functions of the parameters [13]. Finding least-squares estimates for linear models is straightforward as they have a closed-form solution. For nonlinear models, the least-squares estimates must be found using an iterative procedure. In this paper, the Gauss-Newton algorithm is used. This iterative procedure utilizes a Taylor series expansion to find the least-squares estimates [13].

For all transformations, parameter estimates can be found in the usual manner, $\hat{\boldsymbol{\beta}}_j = (\mathbf{X}_j^T \mathbf{X}_j)^{-1} \mathbf{X}_j^T \mathbf{Y}$, and subsequently used to solve for rotation, scale, and sheer parameters. The similarity of the two objects can be assessed using the tridimensional correlation coefficient, R_{3D}, given by

$$R_{3D} = \sqrt{1 - \frac{\sum_i \left\{ (u_i - \hat{u}_i)^2 + (v_i - \hat{v}_i)^2 + (w_i - \hat{w}_i)^2 \right\}}{\sum_i \left\{ (u_i - \overline{u})^2 + (v_i - \overline{v})^2 + (w_i - \overline{w})^2 \right\}}},$$ (18)

which is an extension to the bidimensional correlation coefficient [1].

3. Results and Discussion

An experiment was conducted to evaluate the effectiveness of tridimensional regression and its improvement over bidimensional regression. Three-dimensional landmark data obtained from human faces were used for this purpose. The landmarks were obtained by placing reflective markers on the faces of subjects and tracking the coordinates as the subjects moved through a series of poses using automated software. The landmarks were adapted from [14]. They are shown in Figure 4 and described in Table 1.

The landmarks were obtained for three subjects at two different sittings and five poses per sitting. The objective was to compare R^2 values within a subject to the R^2 values between subjects using both tridimensional regression and bidimensional regression. One would expect the degree of similarity to be higher, thus a higher R^2 value, for two samples from the same person than for samples from two different people. All pairwise R^2 values were calculated for bidimensional and tridimensional regressions. Poses of the same individual within a sitting were not compared since the markers were not removed between poses and using these poses would result in inflated R^2 values.

For each transformation, both in two and three dimensions, the distributions of R^2 values for within and between subjects were obtained by fitting a theoretical distribution

Table 1: Description of landmarks used for evaluation (adapted from [14]).

tr	The point on the hairline in the midline of the forehead.
go	The most lateral point on the mandibular angle close to the bony gonion.
gn	The lowest median landmark on the lower border of the mandible.
en	The point at the inner commissure of the eye fissure.
ex	The point at the outer commissure of the eye fissure.
sci	The highest point on the upper boarder in the midportion of each eyebrow.
n	The midpoint of both the nasal root and the nasofrontal structure.
prn	The most protrudent point of the apex nasi.
ac	The most lateral point in the curved baseline of each ala.
ls	The midpoint of the upper vermillion line.
li	The midpoint of the lower vermillion line.
ch	The point located at each labial commissure.
sa	The highest point of the free margin of the auricle.
sba	The lowest point of the free margin of the ear lobe.
pa	The most posterior point on the free margin of the ear.
jm	The most protrudent point of the muscle when the jaw is clenched.

over the histograms of observed values. Overlaying these theoretical distributions allowed for the estimation of a threshold value (τ) as a cutoff for determining if two images were from the same subject. R^2 values greater than τ lead to the decision that the two images are of the same subject (match) while R^2 values less than τ indicate that the images are of two different subjects (nonmatch). The threshold value was determined to be where the two distributions cross, as to simultaneously minimize the false-positive and false-negative error rates. A false positive is when images of two different subjects are incorrectly determined to be from the same subject (an R^2 value greater than τ for different subjects); a false-negative occurs when two images from the same subject are incorrectly determined to be from different subjects (an R^2 value less than τ for the same subject). In addition to calculating the observed error rates, the expected error rates were found by evaluating the cumulative distribution functions of the R^2 values at τ. Table 2 summarizes the observed and expected error rates, and Figures 5, 6, and 7 show the within-subject (dotted line) and between subject (solid line) distributions for each transformation.

Table 2 shows that both the observed and expected error rates for tridimensional regression are much smaller than those for bidimensional regression using any of the three transformations. Bidimensional regression resulted in both error rates being very high, false-positives often over fifty percent. Tridimensional regression shows a substantial decrease in both false-positive and false-negative error rates which indicates that the three-dimensional method is better at correctly matching a subject to him or herself.

TABLE 2: Error rates for each transformation.

		Bidimensional regression		Tridimensional regression	
		False positive	False negative	False positive	False negative
Euclidean	Observed	59.7%	36.0%	19.3%	12.0%
	Expected	51.9%	33.6%	16.7%	9.0%
Affine	Observed	57.5%	38.7%	17.0%	3.3%
	Expected	49.0%	37.2%	14.9%	7.5%
Projective	Observed	56.8%	35.3%	23.5%	7.3%
	Expected	51.2%	34.5%	18.4%	16.2%

In this application, the Euclidean and affine transformations were comparable to one another with the affine performing slightly better. The projective transformation had the largest observed false-positive rate. This result is not surprising as the flexibility of the projective transformation allows it to map objects into many other shapes. This flexibility results in the ability to match even two very dissimilar objects quite well with certain transformation parameters. Consequently, the R^2 values are very high for all matches. This shifts the between-person distribution closer to the within person-distribution which results in a larger false-positive error rate.

Additionally, a sixth pose was taken on each of the subjects in each setting. This pose was not used to build the within- and between-subject distributions, or to determine the threshold. These six sets of points (two for each subject) were compared to all other poses not taken in the same setting of the same subject (30 comparisons per pose, 6 possible correct matches). The highest R^2 for all six was a correct match. In addition, a minimum of the top 4 matches were correct matches, illustrating that tridimensional regression can be very good at identifying correct matches and discriminating between different objects.

4. Conclusion

Bidimensional regression [1] is a useful tool for comparing two geometric configurations that are each represented by a set of coordinate pairs. The scale, rotation, and translation relating the two configurations can be estimated by first estimating the parameters of the transformation model. As an application of the technique, [2, 3] used bidimensional regression analysis for relating faces in landmark-based face recognition.

In this paper, the bidimensional technique has been extended to three dimensions. Such an extension may prove useful in the analysis of three-dimensional landmark data. The underlying foundations for tridimensional regression have been developed with different transformations: Euclidean, affine, and projective. Its use is demonstrated through an application to compare human faces using three-dimensional landmarks. Results show that tridimensional regression improves the ability to correctly match objects that are represented by landmark data. Both the Euclidean and affine transformations work well to reduce the error rates. The projective transformation also shows improved error rates, but its flexibility may make it too general for some practical applications. Choice of transformation should be given careful consideration given the goals of the application. While there is improvement over Bidimensional regression, the observed and expected error rates are likely higher in this experiment due to the small number of subjects involved and comparing several poses of the same subject. A larger-scale study is needed to better estimate the expected error rates.

This work can be extended in several different directions. The focus here was in developing the theory of tridimensional regression and conducting an initial investigation for shape matching with a feasibility experiment. An investigation with a larger amount of three-dimensional landmark data is needed to more fully understand its effectiveness. In addition to a larger-scale study, it is also of interest to develop weighted tridimensional regression techniques which would allow some landmarks to be weighted more or less heavily than others. Weighting landmarks allows for less weight to be placed on landmarks that are highly variable. Some landmarks could be more variable because they are less reliably extracted or simply due to more natural variability. Weighting has been shown to improve the matching ability in bidimensional regression [15], specifically in a face matching application [16], and is expected to improve the matching ability and precision in mapping for tridimensional regression as well.

References

[1] W. R. Tobler, "Bidimensional regression," *Geographical Analysis*, vol. 26, no. 3, pp. 187–212, 1994.

[2] J. Shi, A. Samal, and D. Marx, "Face recognition using landmark-based bidimensional regression," in *Proceedings of the 5th IEEE International Conference on Data Mining, (ICDM 2005)*, pp. 765–768, November 2005.

[3] S. Kare, A. Samal, and D. Marx, "Using bidimensional regression to assess face similarity," *Machine Vision and Applications*, vol. 21, no. 3, pp. 261–274, 2010.

[4] K. K. Schmid, D. B. Marx, and A. Samal, "Tridimensional regression," in *Proceedings of the Kansas State University Conference on Applied Statistics in Agriculture*, pp. 1–9, 2007.

[5] T. Nakaya, "Statistical inferences in bidimensional regression models," *Geographical Analysis*, vol. 29, no. 2, pp. 169–186, 1997.

[6] N. R. Draper and H. Smith, *Applied Regression Analysis*, John Wiley & Sons, New York, NY, USA, 3rd edition, 1998.

[7] A. Friedman and B. Kohler, "Bidimensional regression: assessing the configural similarity and accuracy of cognitive maps and other two-dimensional data sets," *Psychological Methods*, vol. 8, no. 4, pp. 468–491, 2003.

[8] I. L. Dryden and K. B. Mardia, *Statistical Shape Analysis*, John Wiley & Sons, New York, NY, USA, 1998.

[9] Kramer and Richter, "Projective transformation," 2005, http://doc.cinderella.de/tiki-index.php?page=Projective+Transformation/.

[10] J. D. Foley, A. van Dam, S. K. Feiner, and J. F. Hughes, *Computer Graphics: Principles and Practice in C*, Addison-Wesley, Boston, Mass, USA, 2nd edition, 1995.

[11] O. Schabenberger and F. J. Pierce, *Contemporary Statistical Models for the Plant and Soil Sciences*, Taylor & Francis Group, New York, NY, USA, 2002.

[12] C.-K. Shene, "Geometric transformations," http://www.cs.mtu.edu/~shene/COURSES/cs3621/NOTES/geometry/geotran.html.

[13] D. M. Bates and D. G. Watts, *Nonlinear Regression Analysis and its Applications*, John Wiley & Sons, New York, NY, USA, 1988.

[14] L. G. Farkas, *Anthropometry of the Head and Face*, Raven Press, New York, NY, USA, 2nd edition, 1994.

[15] K. K. Schmid, D. B. Marx, and A. Samal, "Weighted bidimensional regression," *Geographical Analysis*, vol. 43, no. 1, pp. 1–13, 2011.

[16] K. K. Schmid, D. B. Marx, and A. Samal, "Weighted bidimensional regression with a face matching application," in *Proceedings of the 2009 Joint Statistical Meetings*, pp. 1203–1212, 2009.